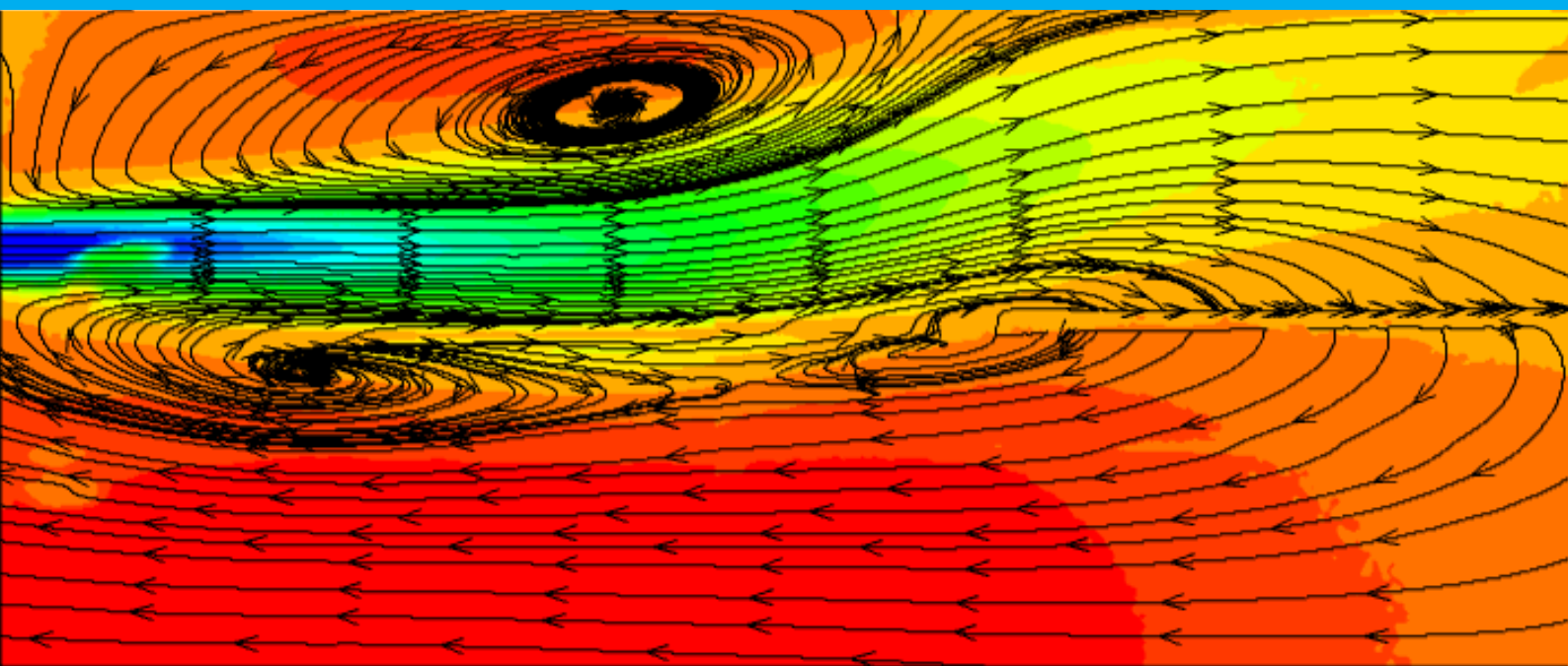


An Experimental Investigation of the Operating Characteris- tics of a Flameless Combustor

N.G.H. Goselink



An Experimental Investigation of the Operating Characteristics of a Flameless Combustor

by

N.G.H. Goselink

to obtain the degree of Master of Science
at the Delft University of Technology,
to be defended publicly on Tuesday the 28th of June at 13:00 hour.

Student number: 4684370

Thesis committee:	Dr. ir. A. Gangoli Rao,	TU Delft, supervisor
	Dr. ir. A. Sciacchitano,	TU Delft
	Dr. ir. I. Langella,	TU Delft
	ir. R. Sampat,	TU Delft, daily supervisor

This thesis is confidential and cannot be made public until June 28, 2025.

An electronic version of this thesis is available at <http://repository.tudelft.nl/>.

Preface

The presentation of my thesis marks the end of my time at the faculty of Aerospace Engineering at the TU Delft. When I started the Flight Performance and Propulsion master track I could not have imagined the amazing journey ahead of me. It was a big step for me, leaving Twente on a quest to become an aerospace engineer. I can safely say now that this has been one of the best decisions I have made in my life. During my master, I developed myself both on a professional and on a personal level. I made great friends and memories that will stay with me for the rest of my life. It has not always been easy, but in the end it was definitely worth the effort. The same can be said about my thesis. I am thankful to have been given the opportunity to work on the flameless combustion setup under the supervision of Dr. ir. Arvind Gangoli Rao and ir. Rishikesh Sampat, it was a great experience.

I wish to thank Arvind for his valuable guidance and feedback throughout this project. The many meetings and discussions we had personally or during the combustion group meetings definitely made me a better engineer and were of great value to my thesis. A very special thanks to my daily supervisor Rishikesh Sampat, for his guidance over the past couple of years. I am thankful for the many discussions we shared on combustion and non-combustion related topics. The many hours we spent in the lab working through issue after issue getting the system up and running, building experimental setups and performing the experiments, were great learning moments

I would also like to thank all faculty members and employees that have contributed to my research by offering advice and assistance during the experimental campaigns and processing of the results. Special thanks to Dr. ir. Ferry Schrijer who was always available for feedback and advice in setting up the experiments. Moreover, I would have not been able to progress this far without the help of Jos, Gerard, Henk-Jan, Dennis, Peter, Frits and Nico from the High-Speed Laboratory technical staff. With a special thanks to Jos van Meurs for all his help and advice on designing and the manufacturing of the different components used on the gas analyser and thermocouple setups.

Of course, I would not have been able to get through all of this without the infinite support from my parents, brother, girlfriend, and my friends both in Delft and Haaksbergen. Shout-out to Sophia and Niña for putting up with me during the highs and the lows of this last half year. Thanks to my (former) BalPol 2 friends Pieter, Bas and Ana for their support and the many drinks and rants we have shared. And of course Emily for her support and feedback in the process.

*N.G.H. Goselink
Delft, June 2022*

Contents

Preface	iii
List of Figures	ix
List of Tables	xiii
List of Abbreviations	xv
Abstract	1
1 Introduction	3
1.1 Environmental concerns	3
1.1.1 Environmental impact by aviation	3
1.2 Previous Work	5
1.3 Current Contribution	6
1.4 Structure	7
2 Theoretical Background	9
2.1 Nitrogen oxide formation	9
2.1.1 Thermal mechanism	9
2.1.2 Prompt mechanism	10
2.1.3 Nitrous oxide mechanism	10
2.1.4 NNH mechanism route	10
2.2 Techniques to lower NO _x emissions	10
2.2.1 Stationary Gas Turbines	10
2.2.2 Aeronautical gas turbines	11
2.3 Flameless Combustion	12
2.3.1 Definition of Flameless Combustion	12
2.3.2 Conceptual FC Combustor Designs	15
2.3.3 Earlier work on a comparable combustor	17
2.4 Focus of Research	17
2.4.1 Grey Areas	17
2.4.2 Research Objective	18
2.4.3 Research Question	18
3 Flameless Combustor Setup	19
3.1 Combustor	19
3.1.1 Overview	19
3.1.2 Pilot burner	19
3.1.3 Burner head	19
3.1.4 Quartz glass chamber	20
3.1.5 Steel chamber	20
3.1.6 Combustor exhaust	21
3.1.7 Cooling ring	21
3.2 System components	21
3.2.1 Air supply system	21
3.2.2 Electric heater	22
3.2.3 Gas rack	22
3.2.4 Ventilation system	22
3.2.5 Gas supply system	22
3.2.6 Data acquisition system	22

3.3	Operating range	22
3.3.1	PIV Campaign	22
3.3.2	Gas composition measurements	25
4	Flow Field Characterisation	27
4.1	Theoretical Background	28
4.2	System Components	28
4.2.1	Seeding	28
4.2.2	Light Source	29
4.2.3	Camera	30
4.2.4	Evaluation of images	30
4.3	Setup	30
4.4	Methodology	31
4.4.1	Setting up the system	31
4.4.2	Separation time optimization	32
4.4.3	Encountered problems and solution strategies	34
4.4.4	Image processing procedure	35
4.4.5	Flow field statistics	36
4.4.6	Uncertainty Estimation	37
4.5	Results	39
4.5.1	Mean velocity field	39
4.5.2	Turbulent velocity field	44
5	Temperature Measurements	49
5.1	Theoretical Background	49
5.1.1	Different types of thermocouples	49
5.2	Setup	50
5.3	Methodology	51
5.3.1	Measurement procedure	51
5.3.2	Temperature correction method	52
5.3.3	Uncertainty estimation	52
5.4	Results	53
6	Emission Measurements	59
6.1	Theoretical Background	59
6.1.1	Infrared analyser	59
6.1.2	Ultraviolet analyser	60
6.1.3	Paramagnetic analyser	61
6.2	Acquisition New System	62
6.2.1	Evaluation Procedure	62
6.3	Probe Design	63
6.3.1	Thermal analysis	63
6.3.2	Aerodynamic analysis	66
6.4	Setup	67
6.4.1	Steel combustion chamber	67
6.4.2	Gas analyser system components	67
6.5	Methodology	69
6.5.1	Thermal model validation	69
6.5.2	Calibration procedure	73
6.5.3	Measurement procedure	75
6.5.4	Data correction	75
6.5.5	Encoutered problems and solutions	76
6.5.6	Probe induced disturbances	78
6.5.7	Influence of system inaccuracies	79

6.6	Results	79
6.6.1	O ₂ concentration	79
6.6.2	CO ₂ concentration	80
6.6.3	NO _x concentration	80
6.6.4	CO concentration	83
6.6.5	CH ₄ concentration	85
7	Results Analysis & Discussion	89
7.1	Flow field characteristics	89
7.2	Temperature & Gas composition	89
7.2.1	Thermocouple measurements	89
7.2.2	Gas composition measurements	90
7.2.3	NO _x formation pathways	91
7.3	How do these results relate to available literature?	91
8	Conclusions & Recommendations	95
8.1	Conclusions	95
8.2	Recommendations for future research	96
A	Background Oriented Schlieren	99
B	Combustor system layout	105
C	Gas supply system layout	107
D	Gas probe strakes overview	109
E	Gas sampling probe layout	111
F	Uncertainty PIV plots	113
	Bibliography	117

List of Figures

1.1	Radiative forcing components from global aviation	4
1.2	Forward NO formation rate	4
1.3	Variation of overall pressure ratio with NO _x emission index	5
1.4	Pathlines on a meridian plane obtained from a CFD solution, showing the relative locations of the peripheral recirculation zone (PRZ) and central recirculation zone (CRZ) [8]	6
2.1	Depiction of different flame regimes according to Wüning&Wüning	13
2.2	S-shaped curves based on the Damköhler number and temperature	13
2.3	Combustion regime map according to Rao et al.	14
2.4	Combustion diagrams for premixed and nonpremixed flames	15
2.5	Schematic of FLOX burner designs	16
3.1	DUT flameless combustor layout	20
3.2	Schematic of the burner head and cut through with the fuel and oxidizer nozzles highlighted	20
3.3	Photo of the steel chamber inserted in the combustor setup	21
3.4	Data acquisition cabinet, with cRIO-9067 embedded controller and different NI modules	23
3.5	Percentage oxygen reactants	24
3.6	Gas composition and temperature measurement locations relative to the flow field	25
4.1	Schematic overview of PIV system	27
4.2	Various fluidized bed seeding generator designs. [40]	29
4.3	Image windowing and window cross-correlation procedure resulting in a velocity vector [41]	31
4.4	PIV Cut Through	31
4.5	Schematic of the burner head rotation due to deformation of the frame under thermal loading. The shown rotation is an exaggeration of the observed rotation	35
4.6	1-D visualisation of PPR [46]	37
4.7	Peak ratio of PIV cross-correlation for respective instantaneous flow field for the reacting case 1.	38
4.8	Large scale flow structures for the case R1	40
4.9	Contour plots of axial velocity for the reacting and non-reacting isothermal flow cases	41
4.10	Comparison of axial velocity flow field contours for different reacting flow cases	42
4.11	Axial velocity distribution along the jet centreline	42
4.12	Normalised radial velocity profiles at $x/d_{noz}=2$	43
4.13	Normalised radial velocity profiles at $x/d_{noz}=5$	43
4.14	Normalised radial velocity profiles at $x/d_{noz}=20$	43
4.15	Normalised radial velocity profiles at $x/d_{noz}=30$	43
4.16	Contour plots of Reynolds shear stress for the reacting, hot and cold flow cases	44
4.17	Comparison of Reynolds shear stress contours for different reacting flow cases	45
4.18	Normalised Reynolds shear stress profiles at $x/d_{noz}=2$	46
4.19	Normalised Reynolds shear stress profiles at $x/d_{noz}=5$	46
4.20	Normalised Reynolds shear stress profiles at $x/d_{noz}=20$	46
4.21	Normalised Reynolds shear stress profiles at $x/d_{noz}=30$	46
4.22	Turbulence intensity distribution along the jet centreline	47
5.1	Render of the setup with combustion chamber and thermocouple mounted on linear traverse	50
5.2	Schematic of the shielded thermocouple, highlighted the positioning of the measurement bead at the tip	51
5.3	Schematic overview of the combustor including burner head, with port 3 & 5 marked in red	51
5.4	Influence of the thermocouple on a laminar flame	53

5.5	Raw and corrected gas temperatures obtained with the ceramic thermocouple for different operating points at 60kW, with $\phi=0.6/0.8$ and N_2 dilution at port 3	54
5.6	Ceramic and platinum thermocouple measurements compared, for $P=60kW$ and $\phi=0.8$ at port 3	55
5.7	Ceramic and platinum thermocouple measurements compared, for $P=60kW$ and $\phi=0.6$ at port 3	56
5.8	Ceramic and platinum thermocouple measurements compared, for $P=60kW$, $\phi=0.8$ and $N_2=450NLPM$ at port 3	56
5.9	Measured gas temperature for a variation in power settings and equivalence ratio at port 3	57
5.10	Radial profiles of temperature at 50kW for different equivalence ratios. Both the slow traverse measurements and the point wise measurements are shown at port 3	58
5.11	Radial profiles of temperature at 60kW for different equivalence ratios. Both the slow traverse measurements and the point wise measurements are shown at port 3	58
6.1	Gas absorption spectrum	59
6.2	Optical gas sensor based on the Beer-Lambert's law, with (a) no signal detected when the IR lamp is off, (b) a maximum detected signal with the lamp on and no sample gas present, and (c) decreasing signal strength for an increase in gas concentration. [55]	60
6.3	Schematic of Limas analyser	61
6.4	Schematic overview of the operating principle of a paramagnetic oxygen sensor [57]	62
6.5	Examples of different types of cooled probe designs, from [53]	63
6.6	Overall heat transfer through a plane wall [58]	64
6.7	Regimes of fluid flow across circular cylinders [61]	69
6.8	Strouhal-Reynolds number plot for circular cylinders [61]	69
6.9	Schematic of the cooled gas sampling probe	70
6.10	Schematic overview of the combustor including burner head, with ports 3 and 6 marked in red	70
6.11	Drawing of the gas analyser system at the lab	71
6.12	Photo of the gas analyser probe inserted in the combustion chamber	71
6.13	Gas probe thermal model validation	72
6.14	Combined plot with gas temperature and coolant flow rate vs radial position in the combustor	73
6.15	2-Point calibration curve, schematic obtained from [65]	74
6.16	Drop in NO_2 during gas composition measurements, for two separate experimental runs	76
6.17	Dew point temperature as a function of the sample gas H_2O vapour pressure. Calculated using the Antoine formula [68]	77
6.18	Zero and span stability test on the NO_2 component	78
6.19	Offset of calculated ϕ from set value	80
6.20	Measured O_2 on the combustor centreline for a range of ϕ at port 6	80
6.21	O_2 on the combustor centreline at port 3	81
6.22	CO_2 on the combustor centreline for a range of operating conditions at port 6	81
6.23	CO_2 on the combustor centreline at port 3	82
6.24	NO_x on the combustor centreline for a range of operating conditions at port 6	83
6.25	Measured NO_x for the cases with dilution vs the oxygen concentration in the oxidiser at port 6	84
6.26	CO on the combustor centreline for a range of operating conditions at port 6	84
6.27	Measured CO for the cases with dilution vs the oxygen concentration in the oxidiser at port 6	85
6.28	Radial profiles of CO vs equivalence ratio at port 3	86
6.29	CH_4 on the combustor centreline for a range of operating conditions at port 6	86
6.30	Radial profiles of CH_4 vs equivalence ratio at port 3	87
7.1	NO_x and temperature trends for a variation in ϕ at 4 different power settings	92
A.1	Overview BOS setup 1/2	100
A.2	Overview BOS setup 2/2	100
A.3	Raw images of background pattern	101
A.4	BOS post-processing steps	101
A.5	Influence of window sizing on the cross correlation results	102
A.6	Correlation between reference images obtained during experimental campaign	102
A.7	Cross-correlation results due to deformation of the reference image 1/2	103
A.8	Cross-correlation results due to deformation of the reference image 2/2	103
A.9	Conclusions BOS	104

A.10 Sources of uncertainty	104
B.1 Combustor system layout	106
C.1 Lay out gas supply system	108
D.1 Different concepts for the suppression of vortex shedding	110
E.1 Schematic of the cooled gas sampling probe	112
E1 Axial velocity distribution along the jet centreline including error-bars representing measurement uncertainty	114
E2 Turbulence intensity distribution along the jet centreline including error-bars representing measurement uncertainty	115

List of Tables

3.1	Operating conditions for PIV campaign	24
3.2	Operating conditions for gas composition measurements at port 6	26
4.1	PIV setup specifications	33
4.2	Estimated Δt for different jet velocities	33
4.3	PIV post-processing steps, equal for all cases	36
4.4	Uncertainty of the mean velocity per operating condition, normalised with U_j	43
4.5	Uncertainty of the velocity fluctuation per operating condition, normalised with U_c	48
6.1	Gas species with requested measuring range and accuracy	62
6.2	Natural frequencies of vibration for a cantilever beam [62]	67
6.3	Overview of the ABB AO2000 extractive gas analyser system customized for the current research	68
6.4	Overview of used calibration gas bottles	73
6.5	Step-by-step calibration procedure	74

List of Abbreviations

BOS	Background Oriented Schlieren
CARS	Coherent Anti-Stokes Raman Scattering
CDC	Colourless Distributed Combustion
COSTAIR	Continued staged air
CR	Center of Recirculation
CRZ	Central Recirculation Zone
DVR	Dynamic Velocity Range
EGR	Exhaust Gas Recirculation
FAR	Fuel-to-Air Ratio
FC	Flameless Combustion
FLOX	Flameless Oxidation
FOGT	Flameless Oxidation Gas Turbine
FOV	Field of View
HiCOT	High Temperature Combustion Technology
HiTAC	High Temperature Air Combustion
LDI	Lean Direct Injection
LEOR	Low Emission Operating Range
LIF	Laser Induced Fluorescence
MILD	Moderate or Intense Low Oxygen Dilution
NDIR	Non-Dispersive Infrared
NR	Non-Reacting
NR _H	Non-Reacting Hot
OPR	Overall Pressure Ratio
PaSR	Partially Stirred Reactor
PIV	Particle Image Velocimetry
PPR	Primary Peak Ratio
PRZ	Peripheral Recirculation Zone
R	Reacting
RMS	Root-Mean-Square
RQL	Rich-Quench-Lean
SNR	Signal-to-Noise Ratio
SP	Stagnation Point
TIT	Turbine Inlet Temperature
TVC	Trapped Vortex Combustor

Abstract

Flameless combustion is a novel combustion technique that has the potential to drastically reduce NO_x emissions in gas turbines and aero engines. This thesis covers the experimental characterisation of a multi-nozzle research combustor capable of achieving flameless combustion. The combustor is operated with methane as fuel and air as oxidiser, under an overall lean equivalence ratio ranging from 0.6-0.9. The work focussed primarily on the design and application of different experimental techniques under varying operating conditions. Particle Image Velocimetry (PIV) is used for reacting and non-reacting flows, where three distinct operating conditions are investigated. Local gas temperature and gas composition measurements are performed to characterise the formation of NO_x in the combustor. Emission data and temperatures are further reported as a function of the equivalence ratio, thermal power input, and oxygen concentration in the oxidiser stream. The oxygen concentration is reduced by diluting the oxidiser stream with either CO_2 or N_2 .

PIV revealed the flow field structures to be very similar between isothermal non-reacting and reacting flow conditions. The location of the recirculation zones is shown not to be affected by heat release. Significant differences are found in the axial flow velocities and turbulence levels in the central recirculation zone, distributed over a larger area under reacting conditions. It is shown that non-reacting isothermal flow PIV can substitute reacting flow PIV if only the flow field structure has to be visualised. Reacting flow PIV is still necessary for more fundamental research of turbulence characteristics and local flow timescales.

The performance of a 15mm ceramic shielded thermocouple is tested and validated. The ceramic thermocouple is seen to underestimate the local gas temperature. It is calculated that a significant correction of 40-60% of the measured value is required to account for radiation heat losses. However, with this correction applied, the thermocouple overestimated the local gas temperatures; hence, the results are deemed unreliable. Another, 3mm, platinum alloy thermocouple is acquired that is much thinner and requires a smaller correction to be applied of only 10% of the measured value. This thermocouple is used to obtain radial temperature profiles near the reaction zone. It shows the temperature profiles to flatten for a decrease in equivalence ratio, indicative of distributed combustion.

For the gas composition measurements, a new advanced gas analysis system has been acquired to measure minor and major products of combustion such as NO , NO_2 , CO , CO_2 , CH_4 and O_2 . For this purpose, a convection-quenched sampling probe has been developed to extract the flue gas from the combustor. The system performed well in measuring minimal concentrations of NO and NO_2 with high accuracy. Within a range of 0-7ppm, unmistakable trends in NO_x could be observed with variations in both power and equivalence ratio. The gas composition measurements showed the NO_x on the centreline near the exhaust to be ultra-low (<10ppm) for all cases investigated. The N_2O and NNH mechanisms are identified as the major contributors in the production of NO_x , and not the thermal pathway, as the gas temperature is consistently below 1800K. Reducing the equivalence ratio and the oxygen concentration in the oxidiser stream reduces NO_x emissions.

The measured CO is consistently below 4ppm for the non-diluted cases, where dilution with CO_2 is seen to increase CO levels. The negligible levels of CO and CH_4 measured near the exhaust confirm the stable operation of the combustor under all operating conditions investigated. Measurements of CO and CH_4 near the reaction zone indicate distributed combustion under lean $\phi < 0.7$ conditions where elongation and widening of the reaction zone are observed. Finally, oxygen measurements near the exhaust and close to the reaction zone indicate the entrainment of cooling air into the combustion chamber, which would locally influence the equivalence ratio. The exhaust duct connection must be redesigned to eliminate the entrainment of cooling air.

Introduction

This thesis discusses the graduation work performed by N.G.H. Goselink as the final part of the MSc track Flight Performance and Propulsion at the Delft University of Technology. This chapter will give the reader an idea about the motivation behind this research and introduce the topic of flameless combustion. At the end of this chapter, a brief structure overview is provided to navigate the report.

1.1. Environmental concerns

Climate change caused by the emission of pollutants is one of humankind's most significant challenges in recent history. Since the early 1900s, the rise in global temperature has had a major impact on the environment and the world we are living in. Consequently, glaciers and ice sheets have been melting and are slowly disappearing, resulting in an increase in the global sea level. Moreover, the world sees more regular extreme weather events [1]. In the near future, the situation will only worsen if we do not act now and act firmly. The emission of greenhouse gasses has to be reduced drastically to limit the temperature increase, as has been determined in the Paris Agreement [2]. The goal of the Paris Agreement is to limit the rise in global average temperature to 1.5 degrees Celsius above pre-industrial levels. [2].

1.1.1. Environmental impact by aviation

The contribution of aviation emissions and their global impact has been debated heavily. An estimate of the relative contribution by aviation is depended on the assumptions on which these calculations have been based. The IPCC, the Intergovernmental Panel on Climate Change, estimated the contribution of the whole transport sector to the total greenhouse gases CO₂ equivalent emissions to be 14% [1]. Moreover, the IPCC estimated that the relative contribution of transportation could be as high as 24% when considering the total energy-related CO₂ emission only [1]. Furthermore, within the European framework, the European Environment Agency (EEA) estimated the contribution by the transport sector to be 27% of the total greenhouse gas emissions [3], with aviation being one of the largest contributors with a relative share of 13.9%.

The commonly preferred metric to quantify the environmental impact of different greenhouse gases is the radiative forcing (RF). RF is defined as a measure of the perturbation of the earth's atmosphere energy budget since 1750 resulting from changes in trace gasses and particles in the atmosphere, measured in Watts per square metre (Wm⁻²) [4]. Figure 1.1 provides an overview of the calculated radiative forcing components for the most common species in aircraft emissions; Carbon dioxide (CO₂), Nitric oxides (NO_x), contrails, water vapour and soot. The role of NO_x is interesting in this case, as it has both positive and negative effects on RF as observed in figure 1.1, where positive is defined as increasing the RF. The positive RF stems from the production of tropospheric ozone (O₃), whereas a negative RF is associated with the longer-term reduction in ambient methane (CH₄). Combining both effects has a net positive effect on the radiative forcing. Figure 1.1 also shows that after CO₂, NO_x is the second highest contributor to the total aviation RF. Over the last centuries, many improvements have been made to reduce fuel consumption and the emission of CO₂ by increasing the engine's thermal efficiency. The trends followed to increase the thermal efficiency are related to increasing the turbine inlet temperature (TIT) and overall pressure ratio (OPR). These trends, however, are negatively related to NO_x as this emission species tends to increase with increasing TIT and OPR. Figure 1.2 shows the influence of pressure and combustor inlet temperature on the formation rate of NO, which grow

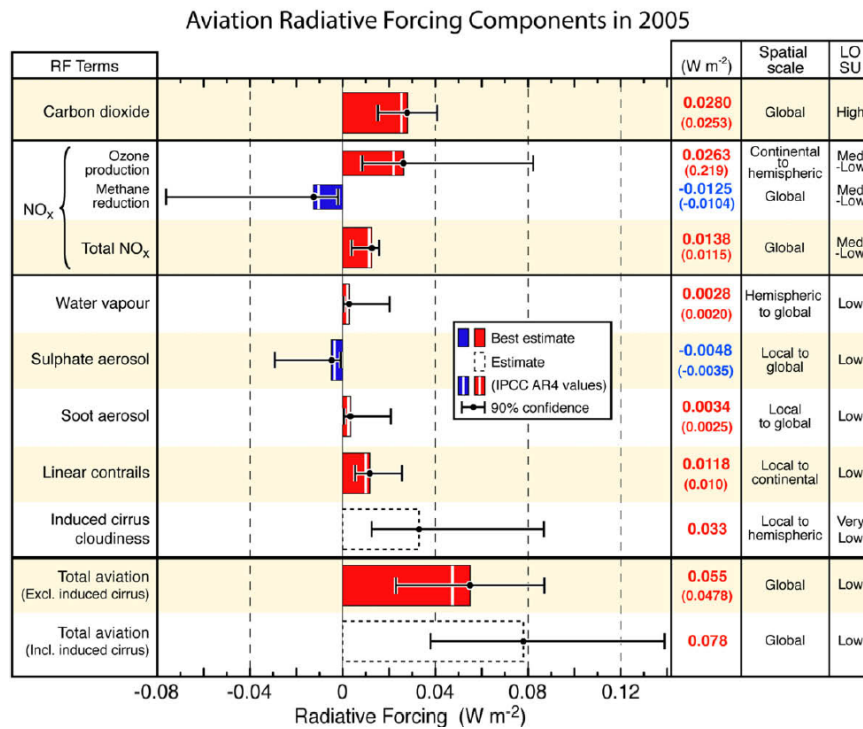


Figure 1.1: Radiative forcing components from global aviation, evaluated from pre-industrial times to 2005 [4]

towards the order of 10^3 ppm/ms for aeronautical gas turbines conditions (TIT > 1000K and OPR \approx 30).

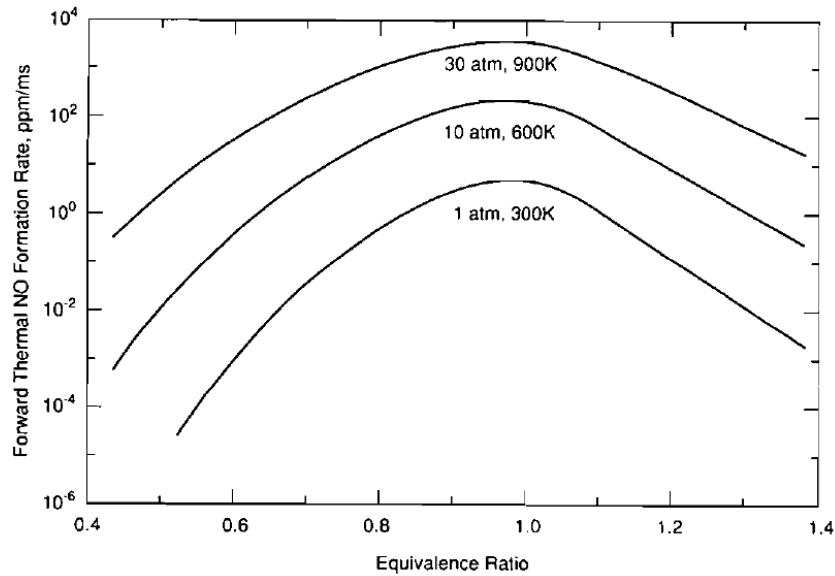


Figure 1.2: Forward NO formation rate. Inlet conditions are representative of laboratory (1 atm, 300K), utility gas-turbine (10 atm, 600K) and aeropropulsion gas turbine (30 atm, 900K) conditions. [5]

Figure 1.3 shows a historical summary of the increase in OPR over the years set against the corresponding NO_x emission index.

Although the NO_x emission index has been lowered for a certain OPR with the development of newer generations of aero engines, these achievements are almost diminished by the increase in OPR of the latest generation of engines. This results in a situation where, despite a reduction in fuel consumption, the NO_x emissions are on a similar level to the smaller engines from the 70s. The grey shaded area in figure 1.3 represents the goal set by the Advisory Council for Aviation Research and Innovation in Europe (ACARE) of a 90%

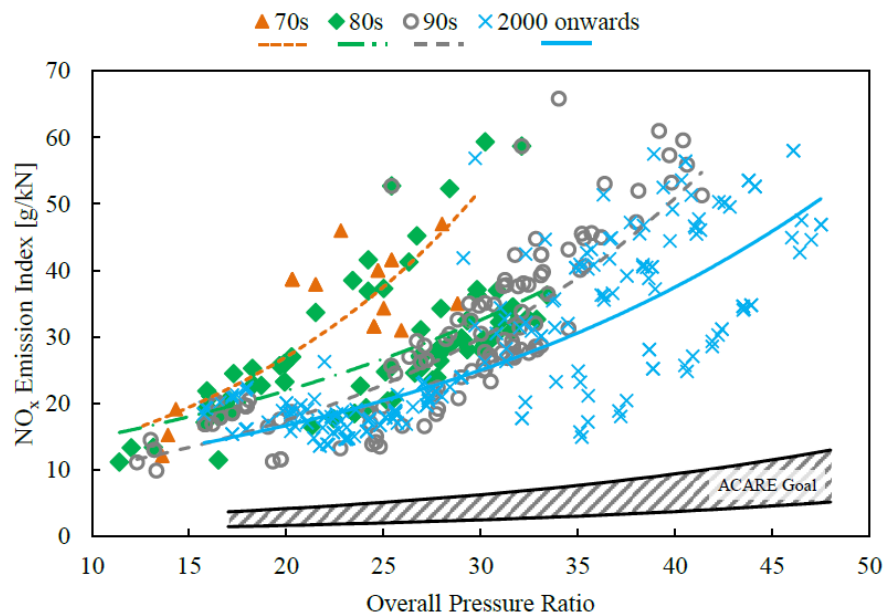


Figure 1.3: Variation of overall pressure ratio with NO_x emissions index over time overlaid with the ACARE Goal as defined for 2050 [6], taken from Perpignan [7]

reduction in NO_x emission levels in 2050 compared to baseline aircraft from the year 2000 [6]. To achieve this reduction in NO_x, new low NO_x combustion techniques must be developed over the years to come. More recently, in the Netherlands, the nitrogen emissions issue has seen the front pages of the papers more often. This is because the Dutch government committed to stricter limits on the emission of nitrogen oxides across all industries. This call for more sustainable alternatives also applies to the aerospace industry. The current work is, therefore, very relevant.

1.2. Previous Work

The previous section highlights the urgency for radical new combustion techniques to lower nitrogen emissions. Several combustion techniques have been developed and tested to reduce NO_x emissions while retaining high combustion efficiencies. Flameless Combustion (FC) is the most promising technique according to a review by Perpignan [7], which considered a variety of approaches such as the Trapped Vortex Combustor (TVC), Lean Direct Injection (LDI), Flameless Combustion (FC), and the Rich-burn, Quick-mix Lean-Burn concepts. Flameless combustion has the potential to drastically reduce NO_x emissions while retaining high stability combustion. This can be achieved by well-distributed reactions which yield low temperature gradients and thus low NO_x emissions. This technique will be further investigated in the scope of this research.

Previous work on flameless combustion at the Delft University of Technology has been performed by Vaz [8], focussing on designing and testing an FC-capable combustor setup, and more recently Perpignan [7]. The latter investigated the use of a computational modelling approach to research parameters which could affect the formation of pollutant emissions in a flameless combustor.

The work by Vaz is particularly interesting, as the burner head used in that research is used on the current setup as well. The current research partly builds on the work done by Vaz. The conclusions previously drawn by Vaz, on the attainment of flameless combustion, are mainly based on the absence of a visible flame, longitudinal temperature, NO_x, and CO profiles. Unfortunately, apart from the visual observation of a decrease in flame luminosity, the difference in temperature profile between the conventional and flameless regimes was small, and the measured NO values were consistently low for all operating points. The evidence presented for attaining flameless combustion is slim and more research is thus required. Vaz was unable to perform PIV experiments to visualise the actual flow field, due to limitations on his setup using a pressurised chamber with limited optical access. Nevertheless, Vaz did perform some CFD simulations to gain insights into the flow field characteristics within the combustion chamber. Figure 1.4 shows the flow pathlines on a meridian plane through the nozzle. This leaves an opportunity for research to characterise the actual flow field under isothermal non-reacting and reacting conditions. Part of the setup and results obtained by Vaz will be used

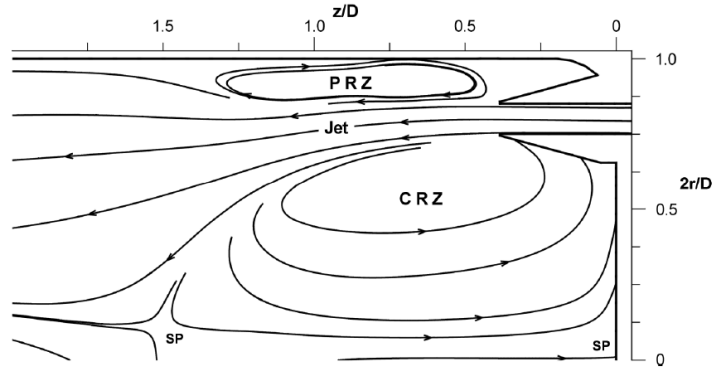


Figure 1.4: Pathlines on a meridional plane obtained from a CFD solution, showing the relative locations of the peripheral recirculation zone (PRZ) and central recirculation zone (CRZ) [8]

as a starting point for the current research. The results obtained are used as benchmark values to validate the results obtained with the current experimental setup.

Research by the DLR on a comparable combustor setup, namely the enhanced FLOX[®] burner, demonstrated the suitability of using laser based techniques to distinguish between conventional and flameless combustion [9]. The combustor operated on a mixture of natural gas and hydrogen at high power densities and high flame temperatures, while NO_x concentrations remained in the single-digit ppm range. The authors presented PIV, OH*-Chemiluminescence (OH*-CL) and Coherent Anti-Stokes Raman Scattering (CARS) experiments, combined with numerical simulations. Varying the fuel blend up to 100% vol. hydrogen, while retaining stable operation, demonstrated the high fuel flexibility this burner concept offers. Additional research by DLR focussed on the combustion behaviour as a function of equivalence ratio, fuel composition and gas inlet velocity, applying OH*-CL and planar LIF-OH techniques while measuring NO_x and CO emission levels at the exhaust [10] and [11]. It was shown that the jet velocity strongly influenced the recirculation rate and mixing between fresh reactants and burned gasses. An increase in jet velocity resulted in an increase in the Low Emission Operating Range (LEOR), NO_x and CO < 10ppm. These papers further demonstrated the possibilities that full optical access to the reaction zone provides in determining the combustion behaviour. In Schutz et al. [12], the pollutant formation in the FLOX[®] combustor is analysed using flow field information from CFD experiments and detailed finite rate chemistry from a Partially Stirred Reactor (PaSR) model. This work shows the benefits of using a combined CFD-CRN approach, coupling the flow field dynamics and chemistry characteristics to characterise the combustion behaviour. Schutz et al. [12] also discussed the different pathways in which minor species such as CO and NO were formed, providing insights into their formation processes by comparing results obtained by the PaSR model with experimental gas composition measurements. Because CFD approximates the actual flow field, a better approach is to use PIV data instead of CFD data to obtain flow field information. A similar approach by Severin et al. [13] combined PIV and flame reactor data to classify the flames into premixed turbulent combustion regimes. This approach had been applied to a single confined jet. This thesis research will use a combination of experimental techniques to characterise the combustor, a necessary first step in the process of characterising the different regimes of combustion that might be obtained. The aim is to provide insights into the macro flow field structure, local temperature and gas composition and combine these different sources of information to get a first image of the capabilities in terms of emission reduction with a variation in operating conditions.

1.3. Current Contribution

This thesis work encompasses the development and application of several different experimental techniques for fundamental research on the flameless combustion setup. As part of the commissioning of the combustor, flow field, temperature, and gas composition measurement techniques have been applied for the first time on this specific setup. The aim of this research is to characterise the combustor setup at the propulsion lab of the faculty of Aerospace Engineering at the TU Delft. The obtained insights into the flow field structures, together with information on the local gas temperatures and gas compositions, will assist in the characterisation of different regimes of combustion to achieve ultra-low NO_x combustion. PIV measurements have been performed under reacting and non-reacting conditions with a high spatial resolution, to identify the

main flow field structures. NO_x emission levels have also been measured with higher accuracy, compared to previous research on a comparable setup by Vaz, to show the variation in NO_x levels subjected to a variation in operating conditions. Temperature measurements have been performed within the combustor to gain insight into the possible pathways in which NO_x is formed under varying operating conditions. Additionally, the temperature profiles might be indicative of a variation in temperature distribution with operating conditions.

In addition to the research described in this thesis, the experimental results are also used in other research as an input to the computational modelling tool of pollutant emissions, building on the work by Perpignan [7]. The flow field information is used to generate an "informed" Chemical Reactor Network (CRN) model that provides temperature and species distributions in the combustor [14]. Moreover, the gas analysis system acquired for this research is also designed and intended to be used for future combustion research at the faculty lab.

1.4. Structure

The motivation and urgency of the current research and some previous work have been highlighted in the earlier sections. The literature review will be covered in the next chapter. Chapter 2 will discuss possible techniques to lower NO_x emissions in stationary gas turbines and aeronautical gas turbines. It is shown that FC may be such a technique which could drastically reduce the NO_x emission levels. This chapter details the different pathways along which NO_x is produced, while the definition of FC is also discussed. By the end of chapter 2, the research objective and research questions are presented.

Chapter 3 focuses on the flameless combustion setup, developed and used for the current research. The combustor layout and supporting system will be explained in detail to give the reader an idea of the system's capabilities and limits, which determine the experimental limitations of the current research. In addition, the experimental matrices are discussed, specifying the operating conditions investigated.

Subsequently, the different experimental techniques used in this research are elaborated on in the chapters 4 (PIV), 5 (Thermocouples), and 6 (Emission measurements). All chapters follow the same basic layout. First, some theoretical background information is given on that specific technique. Then the used setup and methodology are discussed, after which the results are provided.

In chapter 7, the results obtained in the respective chapters for the different experimental techniques are combined to analyse the operating characteristics of the flameless combustor and comment on the possible pathways in which NO_x is produced and how to reduce it. The results are also compared to the literature.

The final chapter 8 summarises the conclusions obtained from the results and observations in chapter 7, the research questions are answered, and recommendations for future research are provided.

2

Theoretical Background

This chapter will deal with the different production mechanisms of NO_x , techniques to lower NO_x emissions, and the theoretical background of flameless combustion. At the end of this chapter, a short overview of the grey areas in literature is discussed, from which the research objective and research questions are defined.

2.1. Nitrogen oxide formation

This research aims to reduce the nitrogen oxide emissions formed during combustion in (aeronautical) gas turbines. First, the different NO_x formation pathways are discussed. Once a basic understanding is created of its production mechanisms, different techniques are proposed to reduce these emissions. The main nitrogen oxide formed during combustion is nitric oxide (NO). Therefore, most studies and mechanisms focus on the production of the NO molecule. The four primary chemical pathways along which NO_x is produced in methane flames are listed and elaborated on in the following paragraphs. This review has not included the *fuel mechanism* pathway. This mechanism describes the oxidation of nitrogen bound to the fuel molecules. For the current research, the used fuel is methane CH_4 . Because methane does not contain any fuel-bound nitrogen, this pathway is excluded from this overview.

2.1.1. Thermal mechanism

The first pathway through which NO_x is formed, is the thermal mechanism, also referred to as the *Zeldovich* mechanism. It is named after the Soviet scientist Yakov Zeldovich, who was the first to postulate this reaction chain in 1946. The reactions involve:



Thermal NO_x is the primary contributor to nitrogen oxide emissions in the higher temperature spectrum. It is an endothermic reaction, which proceeds only at temperatures over 1800K. After exceeding this temperature threshold, the activation energy is overcome and atmospheric nitrogen and oxygen atoms will react according to reaction 2.1, creating N radicals. The large activation energy of around 76 kcal/mol necessary for the dissociation of the N_2 molecule is dictated by the strong triple covalent bond between the nitrogen atoms. The N radicals are subsequently used in reactions 2.2 and 2.3 creating NO. When the temperature exceeds 2200 Kelvin, the formation of thermal NO_x will become very sensitive to small changes in temperature. A perturbation of 90 Kelvin can already change the reaction rate by a factor of 2 [5]. Fortunately, the thermal pathway is a slower oxidation reaction, mostly occurring in the post-flame region. This is effectively reduced by lowering the residence time in the combustion chamber, preventing NO_x from attaining equilibrium values. However, the best way to reduce the formation of NO_x via the thermal mechanism is by reducing peak temperatures within the flow field in regions of high oxygen concentration.

2.1.2. Prompt mechanism

During the 1970s, researchers discovered NO_x formation in the early stages of combustion near the flame region. This finding was contradicting the idea at that moment that the formation of NO_x was a slow mechanism. Further research showed that not the aforementioned Zeldovich but a different and faster process, which already occurred in the flame zone, was responsible for this. The process has been called prompt NO_x , or *Fenimore* NO_x after the researcher who first identified the mechanism in 1971. This mechanism involves a hydrocarbon which reacts with molecular nitrogen following the reaction:



The cyano compound at the RHS of 2.4, can eventually lead to the production of NO again. Besides this mechanism, NO is also formed by 2.2 and 2.3, from the thermal mechanism, which occurs way faster than the first reaction 2.1. The activation energy for the prompt mechanism is in the order of 14 kcal/mol, which explains why it appears in the early stages of combustion. It is also less sensitive to temperature variations [5]. Prompt NO_x formation is not found in the case of non-hydrocarbon combustion processes.

2.1.3. Nitrous oxide mechanism

This mechanism shares similarities with the thermal mechanism, however only occurs at low temperatures. It involves the formation of N_2O as intermediate species, which is subsequently converted into NO. The N_2O molecule itself is not a nitrogen emission. This mechanism will play a more significant role in lean premixed laminar flames or in a situation of highly diluted reactants [5] [8]. The N_2O -intermediate mechanism unfolds as:



which subsequently reacts into N_2 and NO by:



2.1.4. NNH mechanism route

NO is formed via two different routes under the NNH mechanism:



This mechanism becomes especially important when combusting hydrogen gas or hydrogen containing fuels with large carbon to hydrogen ratios. The NNH route can play a significant role in producing NO_x in the flame zone under specific lean conditions, according to Rutar et al. [15].

2.2. Techniques to lower NO_x emissions

This section focuses on different approaches and conceptual designs that have been developed over the years to reduce NO_x emissions. Many novel concepts are initially developed for stationary gas turbines or furnaces, where weight, volume limitations and re-light capabilities are less stringent. Many such developments are demonstrated in stationary applications, which can act as a test bench before their application is extended into the aeronautical sector. Therefore, these stationary systems will first be discussed before the discussion is extended to aeronautical applications.

2.2.1. Stationary Gas Turbines

As discussed in the previous section, the Zeldovich mechanism is the most substantial contributor to the formation of NO_x in gas turbine systems. Many newly proposed combustion techniques try to prevent high peak temperatures from occurring while keeping the residence time low and avoiding high oxygen concentrations in the hottest zones. The following NO_x reducing techniques have been developed for stationary systems.

Flame Cooling

Flame cooling aims to reduce peak temperatures in the reaction zone. This can be achieved by withdrawing enthalpy from the reaction zone or mixing with cooler exhaust gasses or water/steam. Water or steam injection are well-established techniques, as the energy is used for evaporation and dilution. However, this type of cooling technique has both practical limits and requires more regular inspections and maintenance operations, rendering it unsuitable for modern gas turbines.

Staging

Staging can be subdivided into either fuel or air staging. In the first case, fuel is separated and injected into different zones within the combustor to control and maintain an approximately constant temperature throughout the combustor. This technique aims to keep the temperature within a specific range corresponding to low NO_x emissions. Fuel staging systems are designed both radially or axially, creating two separate zones or stages; one designed to operate at partial-load and one optimised for full-load operation. On the other hand, air staging requires the air to be supplied to the combustion zone through small holes positioned in the downstream direction within the combustion chamber. An example of such a system is the COSTAIR combustion system, developed in the framework of the NGT project [16].

Exhaust Gas Recirculation

Exhaust gas recirculation (EGR) can also be used to lower peak flame temperatures. Exhaust gasses are recirculated and injected upstream, into the oxidiser stream or the mixing zone. The flame temperature is reduced due to the combined effect of a decrease in heat-release rate, due to fuel oxidation, and because of an increase in heat capacity in the reaction zone, due to an increase in CO₂ and H₂O concentrations. EGR can be achieved by both external and internal recirculation systems. External recirculation is preferred in existing systems, the exhaust gas is transported via piping outside the combustion chamber towards the combustion air inlet, where it mixes with the fresh air. Internal recirculation is achieved aerodynamically, by optimising the burner design. The advantage of internal recirculation is that there is no need for additional piping or structures. Flameless combustion is also based on internal flue gas recirculation.

2.2.2. Aeronautical gas turbines

This section will extend the discussion on low NO_x combustion techniques for aerospace applications.

RQL

The Rich-burn, Quick-mix, Lean-burn (RQL) technique is a type of staged combustion system aimed at reducing both the CO and thermal NO emissions. The combustor effectively consists of three stages.

1. The fuel-rich burning stage
2. Injection and quick mixing stage where the majority of the combustion air is supplied
3. The fuel-lean burning stage

In both the first and the third stage, the temperatures will be relatively low due to an excess of either fuel or air, respectively. In the second stage, most of the oxidiser is added to the mix; hence this is the critical stage in terms of emission formation. The fuel-rich air from the first stage will have to mix rapidly enough with the fresh air to cool the gas and avoid near stoichiometric conditions. Near stoichiometric conditions will promote high flame temperatures producing NO_x emissions following the thermal mechanism.

Lean Premixed Combustion

The working principle of the lean premixed combustion technique is based on the premise that the adiabatic flame temperature is a function of the amount of excess air. Therefore, increasing the air-to-fuel ratio lowers the flame temperature; hence, the NO_x formation via the thermal path is mainly prevented. However, this regime is limited by the flame's stability, which approaches the extinction limit for very large excess air ratios.

Trapped Vortex Combustor

The trapped vortex combustor architecture aims to increase the rapid mixing of air and fuel in small cavities within the combustion chamber by trapping turbulent flow structures. When injecting the reactants in such a cavity, the highly turbulent local flow promotes the rapid mixing of hot combustion products and reactants. Since this technique sees combustion partly occurring within a recirculation zone, flameless combustion could be achieved [17]. Furthermore, combustion stability is increased using this architecture as the recirculation of hot products can provide continuous sources of ignition to the reaction zones [17].

Lean Direct Injection

The working principle of the lean direct injection combustor is based on the rapid evaporation and mixing of fuel which is directly injected into the combustion chamber. For stability reasons, this requires multiple injectors and swirlers. The swirling flow quickly atomizes the fuel into very fine droplets. This will enhance the rapid and efficient mixing of fuel and air before combustion occurs. This helps to avoid hot spots at near stoichiometric conditions, preventing the formation of thermal NO_x .

Flameless Combustion

Flameless combustion is a technique based on the recirculation of hot products of combustion. It has been developed for furnace applications and is currently being considered for gas turbine applications. Internal recirculation of inert exhaust gasses will dilute the freshly injected reactants, lowering the oxygen concentration. This will decrease the heat-release rate and results in a more homogeneous well-distributed reaction zone, where a visible flame is absent. The more uniform temperature field will have lower temperature gradients without temperature hot spots. This will result in very low thermal NO_x emissions. This combustion technique is inherently stable due to the strong recirculation of hot gasses, induced by the high momentum jets, which supply continuous sources of ignition to stabilize the flame. Although not as mature as other proposed techniques such as RQL and LDI for aerospace applications, flameless combustion has the potential to achieve ultra-low NO_x emissions, outperforming the other proposed techniques [7].

2.3. Flameless Combustion

2.3.1. Definition of Flameless Combustion

Flameless combustion is a combustion technique based on the dilution of fresh reactants by recirculating burned gasses. This lowers the concentration of oxygen (O_2) and limits the reaction rate of the chemistry. In the case of a non-premixed system, the reduced reaction rate allows for increased mixing between fuel and oxidiser and results in more distributed combustion. The reaction progresses over a larger volume and as such, the reaction zone will become more homogenous in temperature compared to a conventional flame, where the reactions take place in a thin zone, the flame front. In order to sustain stable combustion, the reactants have to be at the auto-ignition temperature to overcome the activation energy of the reaction. The reactants have to be either preheated, or enthalpy has to be supplied to the reaction zone. The enthalpy is supplied as thermal energy by the hot recirculated flue gases. The primary benefit of this reduction in peak temperatures is the restriction on the formation of thermal NO and hence low NO_x emissions are achieved. The concept of flameless combustion has first been described by Wünnig and Wünnig [18]. During experiments with a self-recuperative burner developed for furnaces, the authors noticed the absence of a visible flame with an increase in operating temperature. The fuel was still being fully burnt as the CO concentration at the exhaust exit was below 1ppm. Moreover, the measured NO_x was also reduced to the single-digit range. The authors called this Flameless Oxidation or in short FLOX[®]. Further experiments were conducted to gain more insight into FLOX[®]. It was revealed that strong recirculation of inert exhaust gasses was a prerequisite in obtaining this condition. Wünnig and Wünnig determined a parameter called the recirculation ratio K_v shown in equation 2.13

$$K_v = \frac{\dot{M}_E}{\dot{M}_F + \dot{M}_A} \quad (2.13)$$

This equation relates the externally recirculated exhaust gas mass flow, denoted by the subscript E , to the sum of the fuel and fresh oxidizer mass flows F and A respectively. The authors based the boundaries of the flameless oxidation regime based on two parameters; the recirculation ratio and the furnace temperature. The limiting values for both parameters were obtained from their practical experience with furnaces and industrial burners. Figure 2.1 shows a schematic overview of the different combustion regimes identified. Stable conventional combustion is denoted by region 'A', for recirculation ratios of 0.3 or lower. With further increasing recirculation ratio, the flame will become unstable leading to lift-off and eventually blow out; region 'B'. However, if the furnace temperature is sufficiently high, another stable region is reached, region 'C', where flameless combustion occurs. The horizontal line at 700°C delimits a region where no reaction can occur for recirculation ratios over 0.3, this is the self-ignition limit of the natural gas-air mixture. The figure shows that high recirculation ratios and high furnace temperatures are prerequisites for flameless combustion. Several different acronyms have been used to refer to the FC regime such as MILD (Moderate or Intense Low Oxygen Dilution), HiTAC (High Temperature Air Combustion), HiCOT (High Temperature Combustion

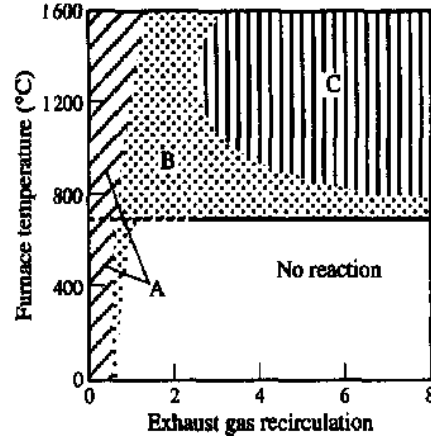


Figure 2.1: Depiction of different flame regimes according to Wünnig & Wünnig [18]

Technology) and CDC (Colourless Distributed Combustion). This demonstrates the absence of general consensus on the terminology, definition, boundaries and characteristics of the regime in literature.

In a review paper by Cavaliere and de Joannon, an attempt has been made to distinguish between the different designations of this regime [19]. It defined HiCOT as an overall concept, describing combustion at high temperatures, with HiTAC being a subset of HiCOT. The authors also defined a new regime, Mild combustion (different from the MILD acronym). The paper provides insights into the fundamentals and applications of the Mild combustion regime. It is characterized by both a high reactant inlet temperature, above the mixture auto-ignition limit, and a mild temperature increase in the combustion process, smaller than this auto-ignition temperature. In the mathematical form given as

$$\Delta T < T_{si} < T_{in} \quad (2.14)$$

Where T_{in} is the reactant inlet temperature and T_{si} the mixture self-ignition temperature. The self-ignition temperature is defined as the point at which any increment in temperature, moves the reaction from the lower to the upper branch of the S-shaped curve. The definition of Mild combustion shares many similarities with the FC regime. The authors acknowledged that this definition of the Mild regime could partly overlap with the FC regime because the definition of FC (and also CDC) is simply a regime with limited flame luminosity. Although the definition of Mild makes sense from a theoretical point of view, from a practical standpoint it is very hard to achieve, due to the prerequisite of the premixed fuel-air mixture to be above the auto-ignition limit at the inlet.

The definition of MILD is given by Oberlack et al. [21]. This definition is based on premixed flamelets

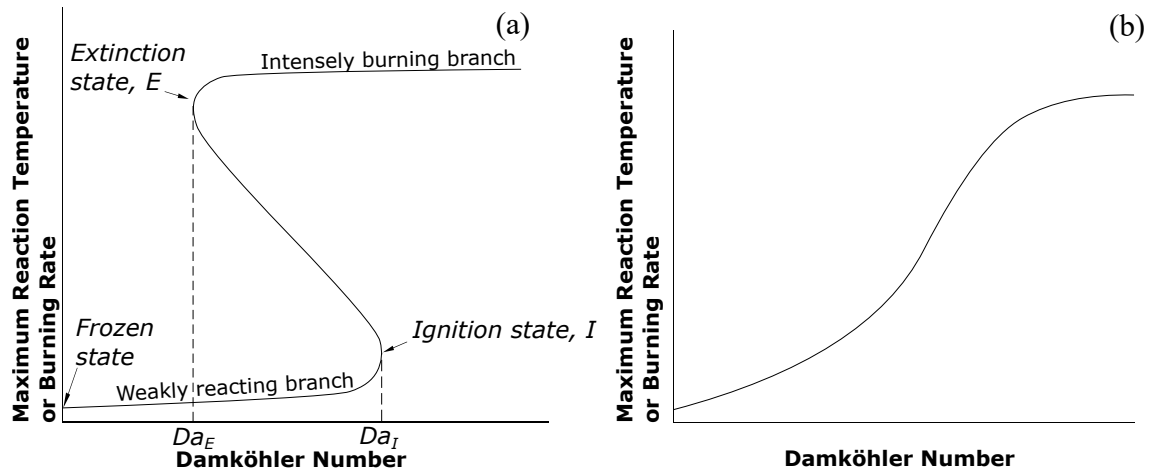


Figure 2.2: S-shaped curves based on the Damköhler number and Temperature. Folded S-shaped curve (a), and stretched S-shaped curve (b) [20]

simulations. This requires MILD (or FC) combustion to behave monotonically, without clear ignition and extinction points. This newly proposed definition is based on the well-known S-shaped curves for premixed conditions. The usual folded S-shaped curve for conventional combustion is visualised in figure 2.2 (a), with the Damköhler number Da and maximum reaction temperature on the horizontal and vertical axes respectively. The extinction and ignition points are located at the positions E and I . At the lower branch of the curve, the 'frozen state' branch, the reaction rate is weak and increases slowly for increasing Da . When Da increases beyond Da_I , the ignition point, the system jumps to the upper branch, the stable burning branch. For stable combustion to occur, it is thus key to keep the system in this upper branch. Following this curve in the opposite direction, decreasing Da , makes the system jump from the upper branch to the lower branch at the extinction point E . The heat loss from the flame becomes too high in this case, with chemical reactions which occur too slow to sustain steady combustion. The 'middle branch' $Da_E < Da < Da_I$ represents an 'unstable' region, where multiple solutions to the system exists, this region can be considered to be physically unrealistic. In the case of MILD combustion, as pointed out by Oberlack et al. [21], the local temperature increase is so small, that transition between burned and unburned is a monotonic function of the Damköhler number which makes the system inherently stable. This situation is shown schematically in figure 2.2 (b). The points of ignition and extinction coincide, this situation does not permit a switch between the different combustion states.

Following this line of thought, Evans et al. [22] made the assumption that MILD (or FC) combustion should not exhibit auto-ignition and extinction in their structures. The system can adopt any position on the monotonic S-shaped curve. In their work, an extension to the discussion on Mild combustion for non-premixed flames is given. It also shows the overlap between the different Mild combustion definitions; conventional auto-ignition and gradual ignition structures both exist within the PSR-defined regime proposed by Cavaliere and de Joannon [19]. In the work of Evans et al. a new non-premixed flame diagram is introduced, in which a distinction is made between auto-igniting non-premixed and gradual combustion regimes, based on the proposition by Oberlack [21]. Moreover, the definition by Evans suggests that MILD combustion may even occur following forced ignition, implying that auto-ignition is not a phenomenon necessary for achieving flameless combustion.

Many of the different definitions discussed, seem to oppose each other. Nonetheless, they all do share some similarities in their operating regimes, highlighted by both Perpignan et al. [23] and Evans et al. [22]. A more practical definition of FC has been proposed by Rao et al., with the focus on gas turbines [24]. The authors proposed a diagram, shown in figure 2.3, which emphasizes the role of T_{in} , the oxygen concentration and the recirculation ratio. This diagram is an advancement of the diagram of Wüning & Wüning shown in figure 2.1. The combustion regimes depicted in this diagram are only indicative, with the recirculation ratio at the top of the diagram, typical for furnace applications.

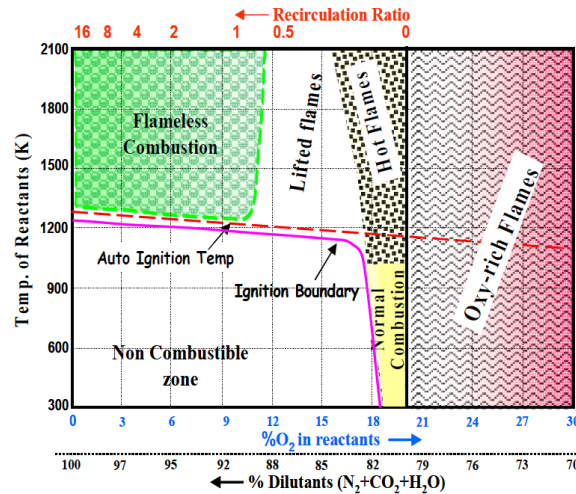


Figure 2.3: Combustion regime map according to Rao et al. [24]

An often returning parameter in the discussion on flameless combustion is the Damköhler number Da , given in equation 2.15, which relates the chemical time scale (reaction rate) t_L to the flow (turbulence) time

scale t_0 . It is a good indicator for flameless combustion as the interaction between turbulence and chemistry is strong under the flameless regime [25].

$$Da = \frac{t_0}{t_L} = \frac{l_0 \nu_L}{\nu' l_L} \quad (2.15)$$

Highly turbulent flow structures occur in the reacting region due to strong recirculation and entrainment of flue gasses, whereas slower chemical reaction rates are observed, due to the dilution of the reactants. The turbulence and chemical timescales become of the same order of magnitude, which results in low Damköhler numbers near unity. The reaction rates are controlled by both turbulence and chemistry.

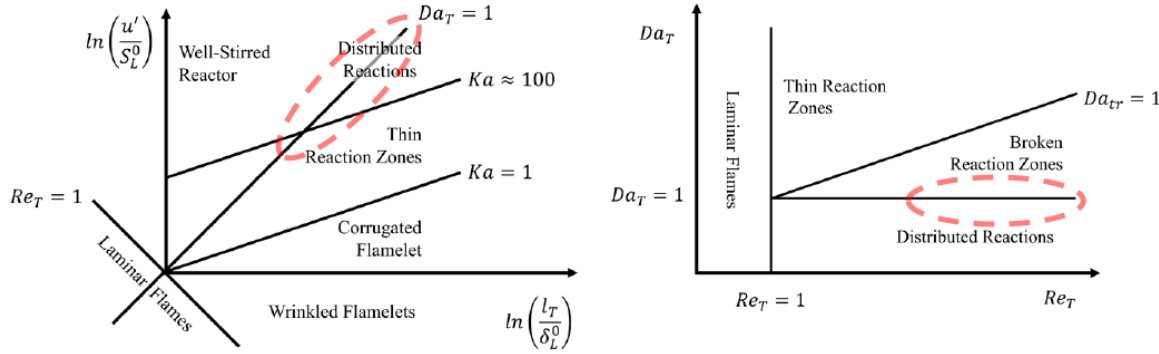


Figure 2.4: Combustion diagrams for premixed (left) and nonpremixed flames (right). Taken from Perpignan [7], based on diagrams proposed by Borghi [26], Peters [27] and Law [20]. Combustion regions related to the flameless regime are highlighted by the dashed lines.

Figure 2.4 shows two combustion diagrams proposed by Borghi [26], Peters [27] and Law [20] for both premixed and non-premixed flames. The flameless combustion regime features a distributed reaction zone, around $Da = 1$. This regime also corresponds to high Karlovitz Ka numbers, as observed from the Borghi diagram for premixed flames (left). Equation 2.16 relates the turbulent Karlovitz, Damköhler and Reynolds numbers, based on the Kolmogorov microscales. The Reynolds number is shown to be a function of the Karlovitz number in the case of the Damköhler number close to unity.

$$Re = Da^2 Ka^2 \quad (2.16)$$

Due to significant variations in local turbulence intensities between the centre of the jet or recirculation zone and the shear layer between both, the local Damköhler number may vary as well throughout the combustion chamber. According to Perpignan et al., given the complexity of using global parameters, a new FC definition should be defined based on local Da and Ka numbers. In that case, the flameless regime could be perceived as a local property instead of a global one and the attainment of the flameless regime could be based on a statistical approach [23].

2.3.2. Conceptual FC Combustor Designs

Different combustor designs are discussed that are able to transition to and operate under the FC regime.

FLOX®

The FLOX® combustor is a patented prototype combustor design of WS Wärmeprozessstechnik. The name is deduced from the phenomenon that the flame luminosity reduces and almost disappears during operation. The burner was initially designed for usage in industrial furnaces, and later further developed for gas turbines. The original design configuration, for use in furnaces, consisted of multiple air nozzles surrounding a central fuel nozzle. The fuel and air are injected separately into the combustion chamber resulting in a non-premixed mixture, the multi-air-nozzles design seen in figure 2.5. In the prototype FLOX® burner for gas turbines, the fuel is injected into the air stream before it enters the combustion chamber, the multi-single-nozzles design, the right schematic in figure 2.5. This results in a partly premixed stream of fuel and air, which ejects into the combustor.

DLR adopted this design to research the application of the FLOX® concept to gas turbines. To test the design under typical gas turbine conditions, the burner was installed into a high-pressure setup, with pressures up to 30 bar [10]. The burner has later been equipped with additional mixing tubes, to improve the mixing of

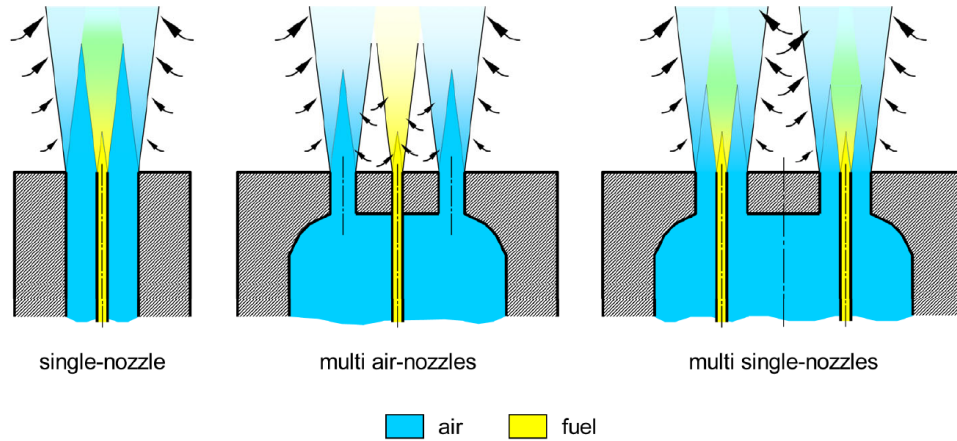


Figure 2.5: Different FLOX[®] burner designs. Figure taken from [18] and adapted by Vaz[8]

oxidiser and fuel, to increase the stability range of this concept, the HiPerMix[®] [28]. The burner developed by Vaz is also based on the multi-single-nozzle design. The final design is a four-fold scaled-up version of the FLOX[®] design, to achieve nominal operating power in the range of about 60 to 200 kW. This system was able to operate under pressures of up to 5 bar (abs.). The combustion system has a can-type configuration and is as such not readily applicable in existing aero-engine concepts which employ annular combustor designs.

FLOXCOM

The FLOX[®] design discussed in the previous section, relies on recirculation induced by the jet momentum. Another approach is to achieve FC in a combustor by recirculating the primary flow. This strategy was adopted by the FLOXCOM combustor, a reverse flow combustor for small to medium size gas turbines. Levy and Rao published several papers on the thermodynamics and principles of operation of this combustor concept [29, 24]. The combustor operates in a non-premixed regime. The primary air stream is injected into a circular combustion chamber, with a second air stream, the stirring air, that acts to create a large recirculation vortex where the fresh air mixes with the products of combustion. The fuel is subsequently injected into this recirculation region where it mixes before combustion occurs. The authors anticipated a pressure loss over the combustor similar to conventional combustors. This concept was further developed by Melo et al.[30]. Experiments on a 60°annular section investigating different air inlet configurations showed to have a significant influence on the emissions measured. In another work by the same authors, the temperature at different locations within the combustor had been measured. The relatively uniform temperature profiles suggested the attainment of FC [31]. The benefit of this concept over the FLOX[®] concept is the possibility to develop it into an annular combustor, making it easier to integrate into current gas turbine architectures.

A more recently developed concept, similar to the FLOXCOM combustor, is the Flameless Oxidation Gas Turbine or FOGT. This is also an annular combustor concept developed by Levy et al. A numerical parametric analysis of the performance of the FOGT was performed to identify a design that could attain FC. Subsequently, the chosen design was optimized to achieve ultra-low NO_x and low CO emissions in the FC mode [32], with NO_x emissions of < 7.5ppm and CO < 35ppm, with only a small pressure drop of < 5%.

COSTAIR

The Continued STaged AIR combustor or COSTAIR is a combustion concept developed to overcome problems often seen in fully premixed combustion systems. These systems have been optimised for base load operations, however, can cause operational problems such as flame flashback, increased CO emissions, and a restricted operating range, when operated at part load. This concept, developed in the framework of the NGT project [16], uses the continued staging of air to reduce NO_x emissions. The air injection is distributed axially over a certain length inside the combustion chamber, with the fuel supplied separately. The system thus operates in the non-premixed or partially premixed mode. This type of combustor has proven to operate stably over a range of operating conditions while keeping NO_x and CO emissions at extremely low levels [33].

TVC

Other combustor designs may also contain flameless combustion zones within their domain. The Trapped Vortex Combustor (TVC) is such an example. The induced vortices trapped in small cavities within the combustor enhances rapid mixing of fuel and air. The hot combustion products which are recirculated mix with the fresh reactants prior to combustion, reducing the oxidizer concentration, basically resulting in flameless combustion [17]. The difference between both concepts lies in the architecture of the combustion chamber. In the TVC, only a small amount of the reactant stream is involved in this combustion process, whereas in a dedicated FC combustor, the full stream is involved. Additionally, in the TVC the combustion process is not necessarily completed within this FC region, but may continue downstream in the main stream oxidiser [17].

2.3.3. Earlier work on a comparable combustor

Previous work on a comparable combustor has been performed by Vaz [8]. The research concluded that most opportunities for future work were found to be in the use of advanced measurement techniques during reacting flow experiments. To do so, the steel three-cylinder configuration should all be replaced by a single quartz glass tube. To provide full optical access for PIV, Rayleigh thermometry, chemiluminescence and Schlieren imaging techniques. Another uncertainty regarding Vaz his work is the absence of conclusive evidence for the attainment of flameless combustion. Difficulties in clearly discerning between flameless and conventional combustion in a lean environment became evident. For all situations reported, the flame temperature lay significantly below the adiabatic flame temperature resulting in measured NO_x values, low in the single digit ppm range. No conclusions could be drawn on the effect of the combustion regime on the NO_x emissions. The eventual distinction between the flameless and conventional regime has primarily been based on the absence of a visible flame as seen by the naked eye.

The following operation parameters have been identified as being instrumental in transitioning toward FC.

1. Reactant inlet temperature
2. Fuel-to-air equivalence ratio
3. Oxygen concentration
4. Thermal power input

Although a variation in jet momentum also has a direct influence on the attainment of FC, this parameter is not mentioned separately, as it is dependent on variations in all four above-mentioned parameters. This shows the difficulties which arise when an attempt is made to separate the influence of each unique parameter. Many of these parameters are not necessarily independent in the system [23]. This makes it difficult to extrapolate results from one setup to other setups, and generalise conclusions. It is necessary to further characterise the different combustion regimes at the current setup.

2.4. Focus of Research

2.4.1. Grey Areas

Most fundamental research into flameless combustion focused on single burner experiments. The advantage of these experiments is the possibility of using advanced laser-optical experimental techniques. However, for FC research to further mature, different tests have to be developed to research the application in gas turbines as well. Key features of the FC regime in gas turbine applications should be investigated on a more fundamental level, for example the characterisation in terms of Damköhler and Karlovitz numbers.

The existing definitions of FC are based on global system parameters such as the global equivalence ratio and furnace/reactant inlet temperatures. However, the FC regime is primarily influenced by local parameters such as the local flow and chemical timescales [7]. Therefore, investigating the attainment of FC on a local level could provide a different approach to the mapping of the different combustion regimes.

Additionally, the initial discovery of FC is made on non-premixed setups, for example, the original FLOX[®] design by Wünnig and Wünnig. The advantages in terms of emission reduction of the FC regime over the existing lean premixed method should be investigated more in-depth.

The reduction in flame luminosity as observed by the naked eye is the main evidence for the shift towards flameless combustion in the research by Vaz [8]. However, the background radiation from the steel walls could bias those observations. Next to the visual observations, fundamental evidence for attaining FC is missing.

No clear differences between the conventional and FC regimes were found. The longitudinal emission profiles that should support this conclusion are inconclusive. The measured NO and CO levels were consistently low, irrespective of the operating conditions. Moreover, the accuracy of the measurements was low. Changes in NO with operating conditions remained within the uncertainty range of the experimental setup. It is thus necessary to measure local NO_x and CO emissions within the combustor with higher accuracy to be able to draw a conclusion on the influence of changing operating conditions. Also, radial temperature and gas composition measurements near the reaction zone could provide additional evidence for a shift in combustion regime.

Comparing the results with a conventional diffusion flame is also recommended. This would require developing a different type of burner head that does not create internal recirculation ratios and does not rely on jet entrainment for stabilisation. Emission measurements on both burners, with a special focus on NO_x, could provide a better comparison between conventional and flameless combustion.

The current understanding of the flow field within the existing combustor, is limited to a RANS-CFD simulation and non-reacting flow PIV data [34]. The existing PIV measurements provide a global overview of the flow field, focussing on the length and stagnation point location of the recirculation zone. However, the spatial resolution is low, and more detailed flow field information is missing. For example, the presence of the PRZ is not visible in the data. PIV data with a higher spatial resolution is required to increase the understanding of the local flow behaviour under both reacting and non-reacting conditions.

The research by Perpignan [7] describes the use of N₂ in diluting the oxidiser stream and hence transitioning towards FC. Even though the experimental data is obtained on a different type of combustor, it is interesting also to investigate this behaviour for the current FLOX type combustor. Furthermore, it might be interesting to investigate the transition towards FC in general for the current setup by diluting the oxidiser stream to decrease the oxygen concentration.

2.4.2. Research Objective

Based on the identification of grey areas in the research on flameless combustion, the following research objective is formulated. The main objective is:

The experimental characterisation of a flameless combustor under varying operating conditions.

This research focuses more on the characterisation of the flameless combustor setup rather than the characterisation of flameless combustion. The thesis provides the tools and procedures necessary to further the fundamental research into this topic. In addition, an attempt is made to quantify the low emission window because this is the most important result to be obtained; how to reduce the emissions of the currently developed combustor. In a later stage, it can be investigated if and how these operating conditions for ultra-low emissions relate to the flameless combustion regime.

2.4.3. Research Question

The research objective is translated into more specific research questions:

1. Which experimental techniques are best suited to be used on a flameless combustion setup?
2. Is the flameless combustion setup able to achieve the ultra-low emission combustion (CO & NO_x < 10ppm)?
3. Which of the following parameters will have a positive influence on the reduction of CO and NO_x emissions?
 - I Thermal power input
 - II Fuel-to-air equivalence ratio
 - III Oxygen concentration in the oxidiser
4. What are the observed differences in flow field characteristics under reacting and non-reacting conditions?

3

Flameless Combustor Setup

This section will discuss the experimental combustor setup at the faculty of aerospace engineering. The chapter is subdivided into a section dedicated to the combustor itself and the different configurations it can be used in. The second section describes the surrounding systems, that support the operation of the combustor.

3.1. Combustor

The combustor consists of the burner head, combustion chamber, and exhaust duct. The other supporting components and systems, such as the gas cabinet, gas bottles, ventilation system and data acquisition system are discussed in section 3.2.

3.1.1. Overview

A schematic overview of the combustor is given in figure 3.1. The expected flow streamlines are shown in red, these streamlines have been estimated based on the CFD solution by Vaz [8]. Part of the flow is recirculated either in the central recirculation zone (CRZ) or the peripheral recirculation zone (PRZ). The remainder of the flow will continue downstream in the direction of the exhaust. The system can be fitted with either a quartz glass tube or a stainless steel tube that will function as the combustion chamber. The quartz glass tube provides full optical access to the reacting flow field, allowing the use of laser optical measurement techniques. The steel chamber is used for emission and/or temperature measurements. The blue lines near the burner head represent the cooling flow directed through slots in the flange along with the combustion chamber to cool the outside of the wall. The blue lines near the exit represent the exhaust cooling flow, which cools the exhaust flow leaving the combustor system.

3.1.2. Pilot burner

The pilot burner is used to ignite the system during startup. The pilot flame itself is ignited by a spark plug inside the pilot burner system. The pilot flame is kept burning until the system reaches a steady-state condition where the reaction is self-sustaining. In order for this to happen, sufficient amounts of hot reacted products will have to be recirculated to supply the necessary enthalpy to the reaction zone. Even after the pilot burner has been shut down, a small flow of air is supplied through the pilot burner system to prevent the nozzle from overheating. The ZMI 16B200R type pilot burner is manufactured by Kromschroder. The system is designed to operate under atmospheric pressure conditions and to use methane as fuel. The fuel and air mix within the pilot burner system can be adjusted to produce a stable premixed flame.

3.1.3. Burner head

The burner head is the component where the fuel and air flows enter via separate inlets, mix in the mixing chamber, and exit into the combustion chamber through 12 nozzles. The burner head also houses the pilot burner in the centre. The 12 nozzles are located at equal distances on a circumference of 126.6mm on the burner head. A schematic of the burner head with the nozzle arrangement can be seen in figure 3.2, where the nozzles are highlighted in red. The pilot burner is not included in this image, however, it normally sits in the centre pocket. The oxidizer inlet line is connected to an external heater upstream. In case of dilution with

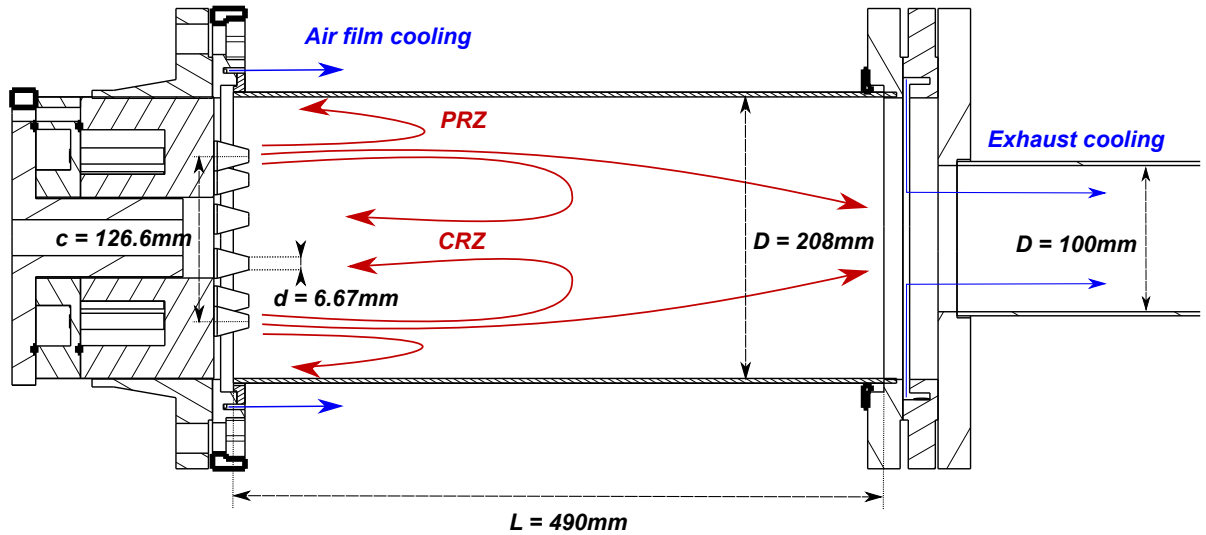


Figure 3.1: DUT flameless combustor layout

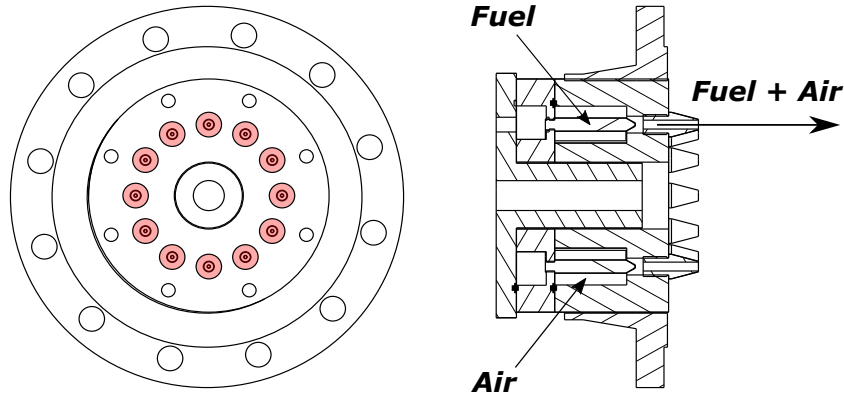


Figure 3.2: Schematic of the burner head and cut through with the fuel and oxidizer nozzles highlighted

either NO_2 or CO_2 , these diluents are mixed and also heated with the air upstream of the burner head. The fuel line is connected to the methane and hydrogen lines but is not heated in the current system. Both the fuel and oxidizer come together in a mixing chamber in the burner head. This should provide sufficient time for both flows to fully mix before being injected into the combustion chamber.

3.1.4. Quartz glass chamber

As discussed previously, the setup is designed in such a way, that the combustion chamber is interchangeable depending on the type of measurements performed. For (laser-) optical measurement techniques, full optical access to the reaction zone is required. Therefore, a quartz glass combustion chamber has been produced. Quartz glass can withstand temperatures up to 1100°C , while it also displays high thermal shock resistance and a low thermal expansion coefficient. The combination of these characteristics makes quartz glass well suited for use in our setup. The glass chamber has an inner diameter of 208mm, a length of 490mm, and a wall thickness of 3.5mm. Due to the transparent nature of the quartz glass, the reaction zone loses heat to the environment by thermal radiation. This heat loss may affect the flame structure compared to the situation with a steel chamber.

3.1.5. Steel chamber

For temperature and/or gas composition measurements a steel combustion chamber has been used. The chamber is constructed from stainless steel (SS 316). This type of stainless steel has been used because it can handle high temperatures up to 925°C . To enable the use of thermocouples and a gas sampling probe, the chamber has been fitted with 6 ports on the outside of the tube. Custom ferrule fittings have been manu-



Figure 3.3: Photo of the steel chamber inserted in the combustor setup

factured to enable the use of different diameter thermocouples and probes through the same port. The ports seal tight onto the thermocouple and probe by means of a ceramic rope gasket inside the ferrule fitting, that is compressed by tightening the nut. Using this kind of sealing, the thermocouple and probe are able to traverse inwards, to obtain measurements at different radial positions, without having any gas leakages. The stainless steel chamber has an inner diameter of 208mm, a length of 490mm, and a wall thickness of 3.0mm.

3.1.6. Combustor exhaust

The combustor exhaust system consists of two different elements. First, the exhaust pipe that is mounted at the exit of the combustion chamber, see figure 3.1. This pipe houses four thermocouples radially inserted to measure the exhaust temperature. These thermocouples are inserted up to a distance of 1/3th from the exhaust centerline. This provides a 4-point temperature measurement and the average temperature is calculated as the arithmetic mean. The exhaust pipe has a smaller diameter (100mm) than the combustion chamber and thus acts as a contraction to the flow. Second, a duct connected to the exhaust pipe that passes the exhaust gasses away from the setup into the atmosphere outside the lab facility.

3.1.7. Cooling ring

The cooling ring is located at the exit of the combustion chamber. The gas temperature at this location will be well above the maximum allowable temperature in the exhaust duct. Therefore, the flow has to be cooled by radially injecting cold air which is then entrained downstream to cool the duct surface. This is schematically shown in figure 3.1.

3.2. System components

This section will discuss all system components that support the combustor and are not part of the combustor itself.

3.2.1. Air supply system

The air used by the combustor system is sourced from a large tank outside the lab, that is pressurised between 20 and 40 bars. The tank provides dry air that is filtered to remove any particulate matter. From the tank, the air first flows through a pressure conditioning system to reduce the pressure to an acceptable operating level between 1-12 bar. This pressure conditioning system consists of two parallel lines with separate mass flow controllers, one suited for a high volume flow capacity and the other suited for a lower flow capacity. The system has been fitted with two lines, as the larger mass flow controller may become unstable handling low flow rates. The low flow rate range is 80-3400 NLPM, whereas the high flow rate range is 9700-30000 NLPM. This also means there exists a gap in the 3400-9700 NLPM range, where no air can be supplied to the system. The mass flow control unit consists of a mass flow meter and valve, that is adjusted based on the measured flow. This operating principle causes small fluctuations in the delivery of air to the combustor, as the valve is constantly adjusted to reach the set point flow rate. According to the data sheet supplied by the manufacturer, the accuracy is 1% FS (or full span). Inside the lab facility, the air supply is further split into 2 more lines that

supply the main air for the combustor and air for the exhaust cooling. The main air for the combustor is distributed over the burner head, secondary airflow for cooling the probe, and the external cooling flange. An overview of the air supply system is provided in appendix B

3.2.2. Electric heater

A 48kW heater is used to preheat the oxidiser stream before it enters the combustor. The air can be preheated up to 700°C when the air flow rate is limited to 0.1 kg/s. Diluent gasses (N_2 or CO_2) are mixed with the air before the flow enters the heater and are thus preheated as well. The heater has a dedicated control cabinet, that is interfaced with the main control system. Three thermocouples are positioned at the outlet of the combustor. Two of those are in direct contact with the control cabinet to provide feedback to the controller. The third thermocouple is connected to the main control system to be logged for data processing.

3.2.3. Gas rack

The gas rack houses the pressure conditioning and control system of the O_2 , H_2 , CH_4 , O_2 , and N_2 lines inside the lab. The gas rack contains 4 manually operated valves for the fuel and diluent lines which have to be opened before starting the experiment. By opening and closing these valves the operator can pressurise the combustor system inside the lab. The gas rack is also equipped with ventilation, to draw any explosive or harmful gasses away in case of a leakage.

3.2.4. Ventilation system

A large fume hood is positioned over the combustor setup. Before the system can be started, first the fume hood should reach a minimum flow rate, to create a safe environment around the combustor, where any combustible gasses are drawn away. The fume hood is kept running during and after the experiments are finished, this will ensure the setup is ATEX compliant. The ventilation system is extended into the gas rack. The ventilation system extends into the atmosphere outside the building. This area has to be cleared before the system can be started. The flow rate through the fume hood is around 4600 m³/h and the flow rate through the gas rack is 1650 m³/h.

3.2.5. Gas supply system

The gas supply is located outside, behind the lab, in a closed-off area. The gas supply houses four different stacks of gas bottles containing the fuels (H_2 and CH_4) and also the diluents (N_2 and CO_2). Each stack consists of 16 B50 bottles each with a volume of 33.3 litres, at pressures ranging from 60 to 180 bar. Lines run from this stack to the lab, where they connect to the gas rack. The bottles outside have a manually operated valve which has to be opened by the operator to pressurize and feed the lab with fuel and diluents. In case of overpressure on the system, the gasses are vented to the atmosphere. Therefore, before the system is pressurised, the area behind the lab is cleared and closed off, adhering to the ATEX regulations. An overview of the gas supply system layout is provided in appendix C.

3.2.6. Data acquisition system

All the data acquisition, monitoring, and control of the combustor system are done by a NI cRIO-9067 embedded industrial controller. The control of the system is done through a LabView program and GUI, which interfaces directly with the data acquisition system. Different NI models are used for the data acquisition and control of the different system components. The data from the thermocouples are acquired with a NI9213 module, with in-house cold-junction temperature compensation. The mass flow controller data is acquired through a NI9870 module, the fuel/air/diluent source pressures are monitored via a NI9205 module, while the heater interfaces with the embedded controller via a NI9265 module. There are separate modules to control the solenoid valves and I/O interfaces for system warning lights and other monitoring requirements. The control cabinet housing the NI controller and modules is seen in figure 3.4.

3.3. Operating range

3.3.1. PIV Campaign

The parameter values corresponding to the different operating conditions for the PIV campaign are tabulated in table 3.1. These values have been decided upon based on a preliminary chemistry analysis.

As discussed in section 2.3.1, to achieve flameless combustion, the oxygen concentration of the fresh

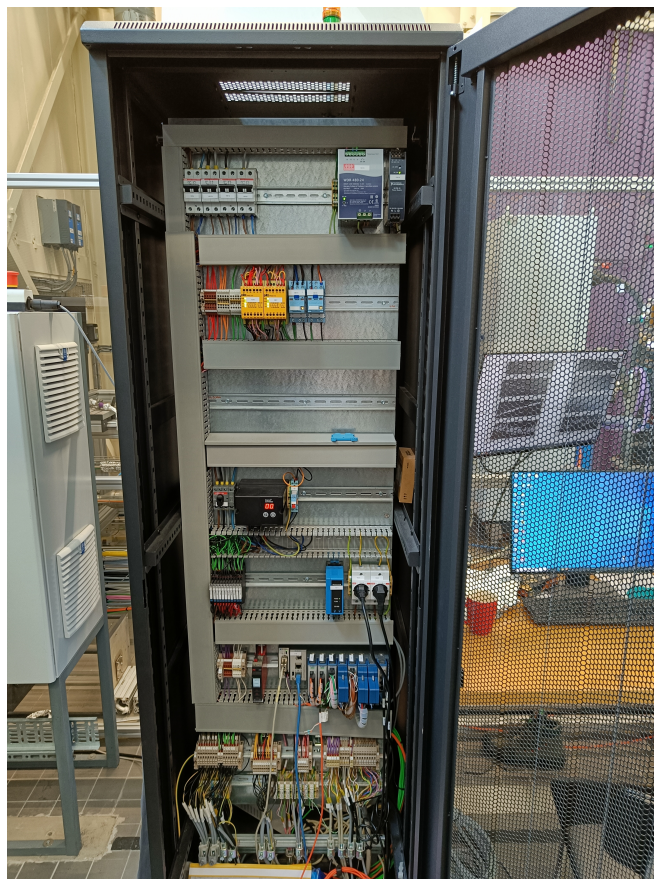


Figure 3.4: Data acquisition cabinet, with cRIO-9067 embedded controller and different NI modules

oxidizer has to reduce below 10%, see figure 2.3. This can either be achieved by increasing the recirculation ratio ($RR > 0.8$) or by increasing the diluent fraction by mixing the fresh air with either N_2 or CO_2 .

To calculate the reactant gas composition for different operating conditions, a single perfectly stirred adiabatic reactor has been modelled in Cantera using the GRI3.0 mechanism [35]. The equivalence ratio and level of N_2 dilution have been varied while keeping the power level constant. For a given absolute nitrogen flow rate, the lowest oxygen concentration is achieved by lowering the thermal power (for constant ϕ). Based on experiences with operating the experimental setup, a thermal power setting of 60 kW and an equivalence ratio of 0.8 resulted in stable combustion over a prolonged period of time. In addition, less methane is needed to run at this power level, making it economically more attractive for longer campaigns. The condition $P=60$ kW, $\phi=0.8$ is thus assumed as the base operating case. For the preliminary simulations, a total recirculation ratio (both the CRZ and PRZ combined) of 1 has been assumed. This is in accordance with the research by Vaz [8].

Figure 3.5 shows the oxygen concentration to reduce for an increase in equivalence ratio and N_2 dilution level. A N_2 flow rate of 450 NLPM has been chosen for the diluted flow experiments. Assuming an ideal fully premixed case, this results in an oxygen concentration in the reactants of around 9-10%. Referring to figure 2.3, this is on the limit of the FC regime. This level of dilution will also result in a jet velocity that is nearly identical to the case of 60 kW and $\phi=0.6$. Keeping the jet velocity nearly constant will omit the effect of a difference in jet momentum and hence the different cases are better comparable. In addition, a similar jet velocity is also preferred for PIV. This choice is thus a trade-off between the reduction in oxygen concentration, the ability to sustain a stable flame and compatibility with the PIV method. Due to the long time the PIV experiments take, it has been decided to only simulate those three operating points.

The air is preheated up to 320°C for all operating cases, this is the maximum temperature the heater could achieve. It is lower than the maximum preheat temperature the heater should be able to achieve theoretically. However, due to reasons unknown, the temperature could not be increased over 320°C. This may be related to the location of the heater far upstream of the burner head. Although the heater and heated air-line are

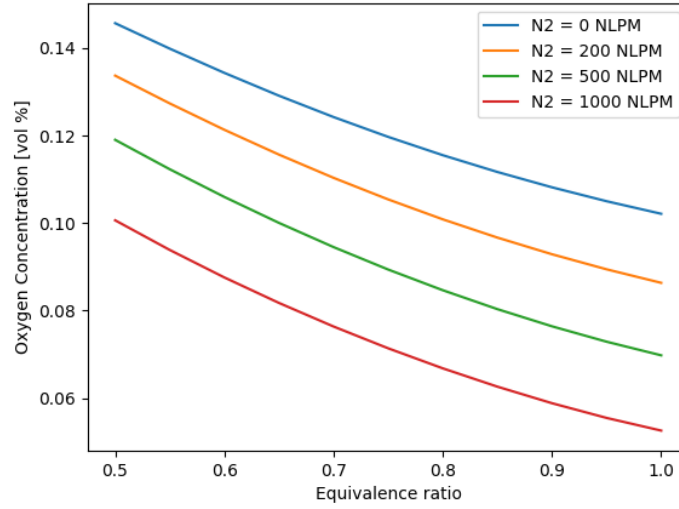


Figure 3.5: The oxygen concentration of the reactants for different equivalence ratio's at 4 levels of N₂ dilution

insulated, there may still be a considerable heat loss over the length of the line.

An overview of the different operating conditions that have been experimentally achieved is given in table 3.1.

Case	Thermal Power (kW)	Equivalence Ratio (ϕ)	Fuel mass flow rate (kg/s)	Air mass flow rate (kg/s)	N ₂ flow rate (NLPM)	Air Preheat Temp. (°C)	O ₂ %	Jet velocity (m/s)
Isothermal flow at 17°C								
NR1	n/a	n/a	0.0012	0.0259	0	17	21	35
NR2	n/a	n/a	0.0012	0.0345	0	17	21	47
Isothermal flow at 320°C								
NR _H 1	n/a	n/a	0.0012	0.0259	0	320	21	72
NR _H 2	n/a	n/a	0.0012	0.0345	0	320	21	96
Reacting Flow								
R1	60	0.8	0.0012	0.0259	0	320	21	72
R2	60	0.6	0.0012	0.0345	0	320	21	96
R3	60	0.8	0.0012	0.0259	450	320	15.5	97

Table 3.1: Operating conditions for PIV campaign

The non-reacting flows are assumed to be isothermal at either 17°C or 320°C. These cases are numbered NR1 to NR2 and NR_H1 to NR_H2 respectively, with the subscript H corresponding to the preheated 'hot' condition. In the non-preheated case, the airflow temperature is close to the ambient temperature. In the pre-heated case, the temperature is measured at the burner head inlet and this temperature is kept constant at around 320°C. Heat losses are assumed to occur in-between the heater and the burner. When the jet is injected into the combustion chamber, the flow is assumed to be isothermal.

For the reacting flow cases, numbered R1 to R3, the power and equivalence ratio per operating point is provided. The corresponding air and fuel mass flow rates are also given in table 3.1. However, in the case

of non-reacting flows, the use of a thermal power input and equivalence ratio may be confusing. Therefore, these values are omitted in those cases, and only the fuel and air mass flow corresponding to the same operating conditions are presented. These mass flows are thus kept constant between all cases NR1, NR_H1, R1 and NR2, NR_H2, R2. For the non-reacting flows, fuel is still being added to the mixture, as it carries the seeding material.

3.3.2. Gas composition measurements

Table 3.2 provides an overview of the different operating conditions that have been investigated for the gas composition measurements. The thermal power of the system has been increased from 30 to 60 kW in steps of 10 kW. For every power setting, ϕ has been varied between 0.6 and 0.9. For $P=30/40/50$ kW at an equivalence ratio of $\phi=0.9$, N_2 or CO_2 flows have been added to the mixture, to achieve a specific the oxygen concentration in the oxidizer flow, see table 3.2. For 60 kW with N_2 dilution, the variation in diluted operating condition is limited to only 450 NLPM at $\phi=0.8$, equal to the diluted operating condition in the PIV campaign.

The operating range for the gas composition measurements is considerably larger compared to the PIV campaign. This is in part due to the fact that these measurements take less time. During the same operational time, more measurements can be done. Next to this, gas composition measurements are also indicative of the stability of the flame under varying conditions. For example, an increase in CO indicates incomplete combustion, which is expected to occur approaching the lean blow-off limit [36]. On the other hand, the measurement of CH_4 indicates the extension of the reaction zone, where unburnt methane is found. The stability limits of the combustor are investigated over a range of operating points between 30-60kW, where stable combustion could be achieved as low as 30 kW. This difference in achieved stable combustion between the PIV and gas composition measurements might be due to the use of the steel chamber. The heat loss due to thermal radiation is lower as compared to the PIV where a transparent chamber is used. This reduction in heat loss from the reaction zone may help achieve stable combustion at lower power settings. Because the temperature measurements have been performed simultaneously with the gas composition measurements, the cases defined in table 3.2 are also used to denote the gas temperature measurements. The different operating conditions are represented by the case numbers G1 to G31. The measurements inside the combustor are performed at 5 discrete radial positions, from the wall up to the combustor centreline. The positions of these measurements relative to the wall and the flow field are shown in figure 3.6. The blue points represent both temperature and gas composition measurements near the reaction zone. The red points represent temperature measurements and the green points represent gas composition measurements of the gas flowing towards the exhaust.

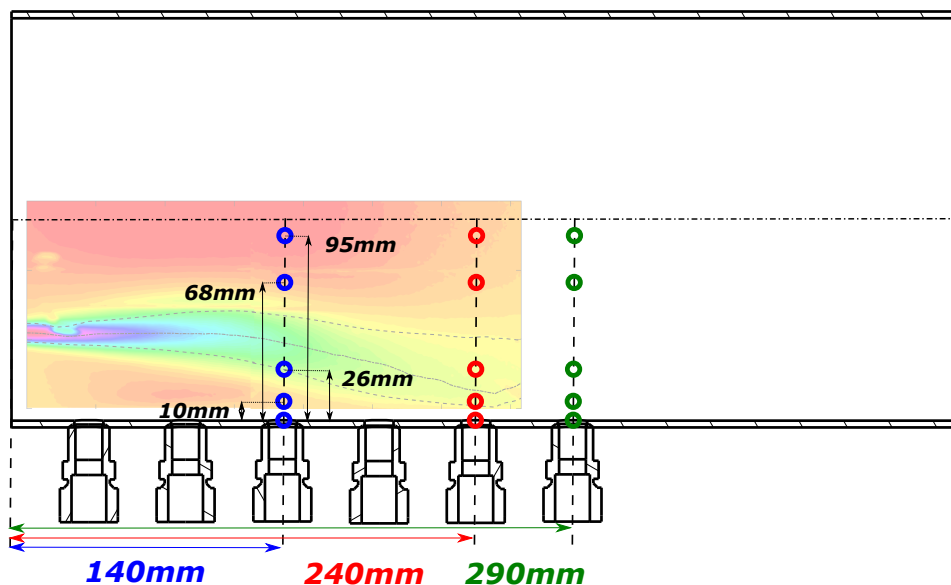


Figure 3.6: Gas composition and temperature measurement locations relative to the flow field

Case	Thermal Power (KW)	Equivalence ratio (ϕ)	N ₂ flow rate (NLPM)	CO ₂ flow rate (NLPM)	Air Preheat Temperature (°C)	O ₂ %	Jet velocity (m/s)
G1	30	0.6	0	0	320	21	48
G2	30	0.7	0	0	320	21	41
G3	30	0.8	0	0	320	21	36
G4	30	0.9	0	0	320	21	32
G5	30	0.9	113	0	320	17.5	38
G6	30	0.9	285	0	320	14	48
G7	30	0.9	0	59	320	19	35
G8	30	0.9	0	113	320	17.5	38
G9	40	0.6	0	0	320	21	64
G10	40	0.7	0	0	320	21	55
G11	40	0.8	0	0	320	21	48
G12	40	0.9	0	0	320	21	43
G13	40	0.9	151	0	320	17.5	51
G14	40	0.9	379	0	320	14	64
G15	40	0.9	0	79	320	19	47
G16	40	0.9	0	151	320	17.5	51
G17	50	0.6	0	0	320	21	80
G18	50	0.7	0	0	320	21	69
G19	50	0.8	0	0	320	21	60
G20	50	0.9	0	0	320	21	53
G21	50	0.9	189	0	320	17.5	64
G22	50	0.9	474	0	320	14	80
G23	50	0.9	0	98	320	19	59
G24	50	0.9	0	189	320	17.5	64
G25	60	0.6	0	0	320	21	96
G26	60	0.7	0	0	320	21	82
G27	60	0.8	0	0	320	21	72
G28	60	0.8	450	0	320	15.5	97
G29	60	0.9	0	0	320	21	64
G30	60	0.9	0	118	320	19	71
G31	60	0.9	0	226	320	17.5	77

Table 3.2: Operating conditions for gas composition measurements at port 6

4

Flow Field Characterisation

Particle Image Velocimetry or PIV is a measurement technique that allows for the visualisation of the instantaneous flow field within a plane. In contrast to single-point methods such as hot-wire anemometry and laser-Doppler anemometry, PIV provides insights into the instantaneous coherent flow structures. It is currently the most used flow visualisation technique in experimental campaigns. A schematic overview of a typical PIV setup is shown in figure 4.1. The figure shows the components required in a basic PIV setup; one or two cameras, a laser system, different optics, and an image acquisition system. The seeding generator is missing in this schematic.

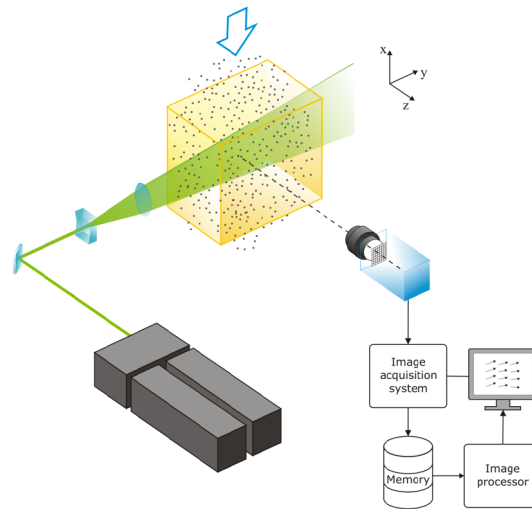


Figure 4.1: Schematic overview of PIV system [37]

The clever use of different optical devices such as lenses and mirrors transforms the beam from a pulsed light source into a laser sheet with a certain thickness in the region of interest. The FOV, the visualised region, is determined by the camera, lenses and optical layout. To obtain the highest resolution, it is beneficial to minimize the variation in thickness in the FOV. The optics have to be arranged in such a way that the beam waist, the thinnest beam diameter, falls outside this area. It is advised to have an approximately constant beam thickness in the FOV of one or two millimetres. The scattered light is captured onto subsequent image frames by one or two digital cameras. A system with one camera can only capture two velocity components within the region of interest and is therefore only suitable if the out-of-plane velocity component is negligible. In the case of combustion research, capturing the out-of-plane velocity component is also important as this provides information on the degree of turbulence. In which case, a system with two cameras should be used.

4.1. Theoretical Background

PIV is based on a phenomenon called Mie Scattering. Mie Scattering is the elastic scattering of light of particles with a diameter similar to or bigger than the incident laser light wavelength. Mie Scattering is much stronger than Rayleigh scattering and can therefore already be obtained at smaller incident light power levels. In short; PIV relies on the presence of small particles which follow the flow accurately and which are illuminated by an external light source to measure the velocity (field) of the flow considered.

4.2. System Components

4.2.1. Seeding

Stokes Law

This technique relies on the assumption that the seeding particles follow the flow closely and in the mean-time are seeded with a high enough density to provide a good spatial and temporal resolution. This first assumption follows from the equation of motion of a very small spherical particle, which is dominated by the viscous Stokes drag. The velocity difference between the particle velocity v_p and flow velocity U is called the slip velocity, given in 4.1 [37].

$$v_p - U = \frac{2}{9} \frac{a^2(\rho_p - \rho_f)}{\mu} \frac{dv_p}{dt} \quad (4.1)$$

For tracer particles to accurately follow the flow, the slip velocity should be small. For gas flows, this is very difficult to achieve, because the ratio ρ_p/ρ_f is of $\mathcal{O}(10^3)$. Hence, the user has to resort to particles with a very small diameter of only a couple of microns ($1\text{--}3\ \mu\text{m}$). In equation 4.1 is a the tracer particle radius. The usability of tracer particles in turbulent gas flows is quantified by the Stokes number S_k , the ratio between particle response time τ_p and the flow time scale τ_f , see equation 4.2. The particle response time is the time needed for the particle velocity to adjust to a step-wise variation in flow velocity. For accurate results, τ_p should be kept smaller than the smallest time scale of the flow. As a rule of thumb, $S_k < 0.1$ gives good flow tracing accuracy. The lower limit of the seeding particle diameter is governed by the laser wavelength, as the scattering will have to lay in the Mie regime, thus $d_p > \lambda$.

$$S_k = \frac{\tau_p}{\tau_f} \quad \text{with} \quad \tau_p = d_p^2 \frac{\rho_p}{18\mu} \quad (4.2)$$

For a PIV system to provide accurate measurements over the whole flow region, the seeding particles must be homogeneously distributed within this flow region. However, this is not always possible due to physical processes in the flow which affect the density, such as compressibility effects and flames.

Seeding material

For accurate tracking of the tracer particles, it is important to use the appropriate seeding material. For non-reacting cold flows, a glycol-water solution or vegetable oil is often used for PIV experiments. However, in the case of reacting flows, another type of seeding material should be used. These particles have to be chemically inert, non-abrasive, inexpensive and should be able to withstand the high temperatures in the combustion chamber. The particles should also be safe to handle in a lab environment; non-toxic, non-corrosive, and harmless. Several different materials are available according to the literature, metallic oxides or silicate powders for example. A review by Chen and Liu, comparing different tracer-particle materials, concluded that titanium-oxide TiO_2 is most suitable for these experiments [38]. It has good scattering characteristics, a high melting temperature of 1750°C , and is less abrasive upon impact with the glass wall due to a lower Vickers hardness.

The flow-tracking characteristics of the TiO_2 particles have been investigated by Scarano and Van Oudheusden. The particle response time for TiO_2 particles is measured across an oblique shock wave [39]. This shock wave represents a well-known abrupt velocity gradient and is therefore suited to characterize the particle response time to a flow velocity discontinuity. According to Scarano and Van Oudheusden [39], the response time of a TiO_2 particle is less than $3\ \mu\text{s}$ for an effective particle diameter of $0.27\ \mu\text{m}$, which is ample for our case. TiO_2 has thus been used for the experimental campaign.

Seeding Generator

The difficulty in using powder-based seeding particles such as TiO_2 is the continuous and well-distributed introduction of these particles into the flow. Different approaches are available such as atomization and

fluidisation of the solid particles. For this experimental campaign, a small cyclone seeding generator is used. This seeding generator is developed at the TUD and is previously used on high-pressure systems. The fuel line containing methane for a single nozzle is seeded and not the main air line. This means that the flow rate through the seeding generator is very small. It also means that the volume of the seeding generator should be reduced as well, to achieve sufficient fluidisation and entrainment of the seeding.

Two different versions of a fluidized bed seeding generator are shown in figure 4.2. Both operate on the same principle that a powder of submicrometre particles are suspended in the bed and the seeding is drawn from the top of the seeding generator. However, most particles dispersed in the flow are several times larger than the nominal particle size of the powder. According to Melling, this is a result of coagulation of particles due to the humidity of the gas, moisture content of the particles, and rate of flow through the seeding generator [40].

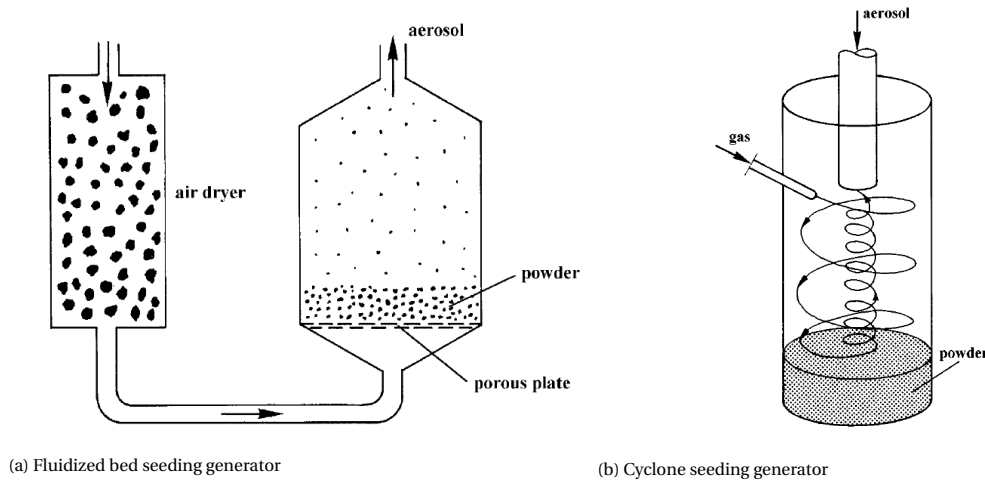


Figure 4.2: Various fluidized bed seeding generator designs. [40]

The seeding generator design used for the current PIV experiments closely resembles the one in figure 4.2b. The used seeding generator consists of a turbulent jet that impinges onto the bed of seeding powder. The outlet is on the top of the vessel next to the inlet, such that the flow changes direction and recirculates inside the seeding generator. Larger clumps of particles will be ejected by the centrifugal forces resulting from the recirculation inside the vessel. Larger particles which are still being entrained by the flow will be broken up in a throttle valve at the outlet of the seeding generator that exerts a high strain on the flow.

The mean diameter of the TiO_2 particles is $0.5 \mu\text{m}$ according to the manufacturer specifications. However, the effective particle size can vary throughout the experiment due to the agglomeration of particles in the seeding generator over time. This problem is being countered by heating and drying the seeding material before filling the seeding generator. It is also recommended to reduce the supply line length between the seeding generator and injection point into the flow. This will avoid secondary agglomeration of the particles in the supply line. Even with applying these best-practice suggestions, the control of the seeding density in the flow is still an empirical process, which will introduce variations in seeding density, heavily impacting the PIV results. These issues will be further discussed in section 4.4.1.

4.2.2. Light Source

Lasers are the obvious choice to use in PIV because they create a pulsed monochromatic collimated light beam. Most commonly used at the Aerospace Faculty, is a frequency-doubled Nd:YAG laser emitting green light with a wavelength of 532nm . The principle of PIV is based on a very short illumination period of the particles by the laser, the pulse duration δt . If the duration is too long, the particles will look like streaks and not like dots, this would make post-processing of the images impossible. This further means, that particle displacement during the illumination or pulse duration must be significantly smaller than the particle image. Also, the pulse energy has to be of such a level, that the cameras can capture the scattered light. According to the Handbook of experimental fluid mechanics [37], energy levels of 100mJ should be sufficient to illuminate an area with a length of 10 cm in air.

4.2.3. Camera

The particles are photographed by a digital camera, with either a CCD or CMOS sensor. The lens of the camera is characterized by the focal length (f), f-stop ($f_{\#}$), and the magnification factor (M). $f_{\#}$ is the lens's focal length divided by the aperture diameter, and M is the ratio of the image size or distance to object size or distance. These parameters can be combined in several equations, such as the basic lens formula. When imaging a particle on the sensor, effects due to the diffraction of light have to be taken into account as well. This will limit the minimum particle image diameter and results from the resolution of the optical system used in the experimental setup [41]. An approximation of the particle image diameter, taking into account both diffraction and the original particle diameter is given in equation 4.3.

$$d_{\tau} = \sqrt{(Md_p)^2 + (d_{diff})^2}, \quad \text{with} \quad d_{diff} = 2.44\lambda(1 + M)f_{\#} \quad (4.3)$$

For optimum resolution, the particles in the laser sheet must be in focus. Hence, the light sheet thickness in the FOV has to be smaller than the focal depth δz of the optical system. The definition of the focal depth is given in equation 4.4

$$\delta z \approx 4 \left(1 + \frac{1}{M}\right) f_{\#}^2 \lambda \quad (4.4)$$

4.2.4. Evaluation of images

Once the experiments have been performed and all the images are acquired, the evaluation of the images starts. To obtain the velocity vectors from the images, the following 4 operations have to be conducted.

1. **Image windowing:** The sensor image is divided into smaller windows, usually of the order of 16x16 to 128x128 pixels. Within these 'interrogation windows', the local displacement and velocity vector will be determined. To obtain optimal results, each window will have to contain a significant amount of tracer particles.
2. **Image cross-correlation analysis:** A statistical tracking operation is performed, on two consecutive images, part of the two consecutive exposures. For each window, as defined in step one, the operation returns a 2D map, with the highest peak at the displacement position relative to the origin which denotes the average displacement of the tracer particles between the two exposures 'A' and 'B'.
3. **Correlated peak sub-pixel interpolation:** The position of the highest peak, is located at the closest integer pixel position. However, to increase the accuracy of the peak positioning and subsequent velocity magnitude and direction. The peak position is more accurately determined by estimating the peak position via sub-pixel interpolation of the peak.
4. **Calculate velocities:** The resulting particle motion in terms of pixel shift, between both windows of exposure 'A' and 'B', is divided by the time separation between both laser pulses and magnification M . When multiplied by the size of the pixel, this gives the velocity vector over this specific window.

The aforementioned operations are performed for all windows, to provide a plot showing the flow field as a collection of velocity vectors. This whole methodology is visualised in figure 4.3.

4.3. Setup

To obtain a high resolution in an extended FOV, 2 cameras in the planar configuration are used simultaneously next to each other. The FOV of both cameras partly overlap, so no information is lost between both cameras. This overlap will also help in stitching the two frames together in the post-processing phase. The position of the FOV of both cameras in relation to the burner head is visualised in figure 4.4.

The following equipment is used in the experimental campaign:

- Quantel Evergreen 200 Nd:YAG laser with 200 mJ per pulse at 532 nm
- Two LaVision Imager sCMOS cameras with a sensor size of 2560x2160 pixels and pixel size 6.5x6.5 μm
- Micro Nikkor 105 mm lens with $f_{\#}$ 11

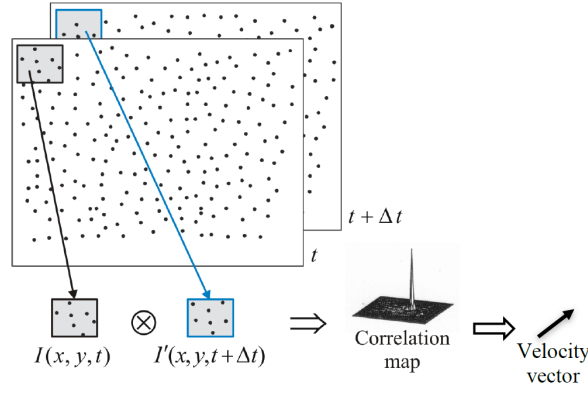


Figure 4.3: Image windowing and window cross-correlation procedure resulting in a velocity vector [41]

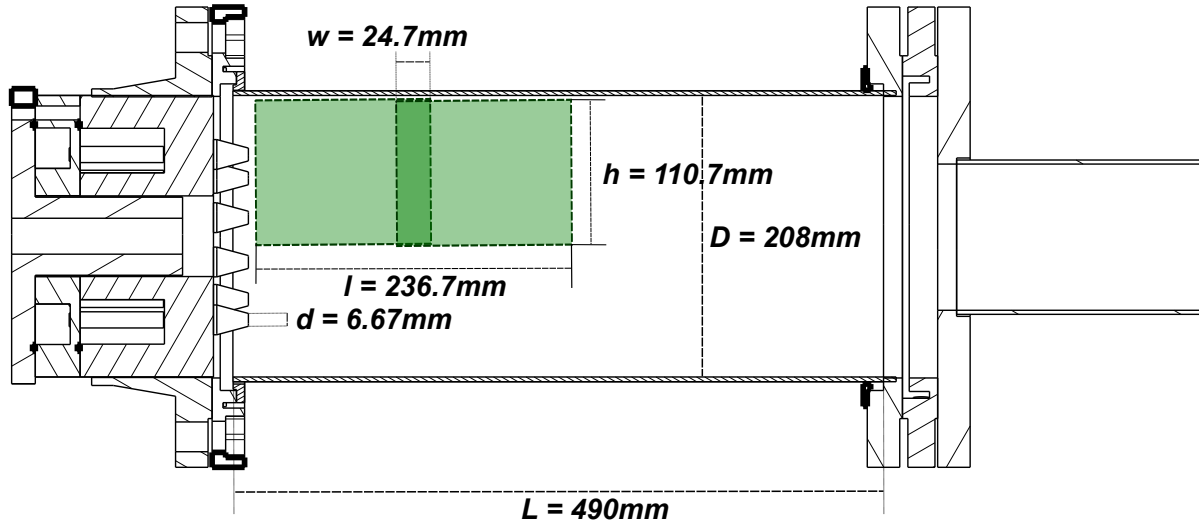


Figure 4.4: Combustor cut through schematic with PIV measurement plane. The green dashed lines represent the overlapping FOVs of the two cameras

- LaVision Programmable Timing Unit (PTU)
- Polarization filters
- 532 nm bandgap filters

The LaVision PTU is used to coordinate between the laser trigger and camera acquisition. Polarization filters are placed in front of both cameras to reduce reflections from the tube. The 532 nm bandgap filters are placed on the Nikkor lenses and will eliminate background noise and flame luminescence.

4.4. Methodology

This section will discuss the experimental method used to obtain PIV results. From setting up the system to the optimization of the laser separation time, and finally the estimation of the experiment uncertainty.

4.4.1. Setting up the system

The usability of the TiO_2 particles in a turbulent jet has been verified by estimating the Stokes number. The Stokes number is the ratio between the particle response time and the characteristic flow time. The particle response time τ_p is taken from Scarano and Van Oudheusden [39], $\tau_p < 3 \mu\text{s}$. The characteristic flow time is the smallest flow timescale, the Kolmogorov time scale τ_η , calculated according to equation 4.5.

$$\tau_\eta = \left(\frac{\nu}{\epsilon} \right)^{1/2} \quad (4.5)$$

With the average rate of dissipation of turbulence kinetic energy, and ν the kinematic viscosity. The dissipation rate is approximated by

$$\epsilon \propto \frac{\mathcal{U}^3}{\mathcal{L}} \quad (4.6)$$

with \mathcal{U} and \mathcal{L} the velocity scale and length scale of the flow respectively. This dissipation rate thus scales with the flow macrostructures [42]. \mathcal{U} and \mathcal{L} are related to the flow geometry, as a rough estimate, the turbulent velocity is assumed to be the nozzle exit velocity, and the length scale is assumed to be the nozzle diameter. This gives $\mathcal{U} \approx 97.0$ m/s, and $\mathcal{L} \approx 0.00667$ m. Using these values, the dissipation rate is estimated at $\epsilon \approx 1.37 \times 10^6$, and the kinematic viscosity is assumed to be that of air at 1500 K. The Kolmogorov time scale is thus estimated to be 13 μ s. The Stokes number in this case, according to equation 4.2, is $3/12.7=0.23$. The particle response time is 4 times smaller than the smallest flow timescale in a highly turbulent environment. This is deemed sufficient for the current experimental campaign.

As mentioned before, the seeding particles are introduced in the fuel flow rather than the airflow. This approach has been followed because of the benefits of having low humidity in the methane flow, which is supplied on a dry basis, and the low flow rate of methane compared to air. Both should have a positive effect on the entrainment of seeding in the cyclone seeder, according to Melling [40]. Moreover, only a restricted portion of the flow field had to be visualised. Because the planar PIV only focuses on a plane through the centre of the top nozzle, only the stream tube passing through this FOV should be seeded. This results in a seeding layout where the fuel flow to a single nozzle is being seeded. This way a higher seeding concentration can be obtained by passing only a fraction of the flow through the seeder, compared to the full fuel or even airflow. In the latter cases, the maximum attainable seeding concentration may not meet the high seeding requirements needed in reacting flow measurements. Additionally, by seeding only the top nozzle a longer experimental run could be achieved because the rate of transparency decrease in the glass tube is reduced

The cameras have been set up and focused according to the following procedure:

1. The light sheet thickness has been measured using a millimetre paper and optimised to be around 1mm in thickness in the FOV.
2. The cameras are focused on the desired plane using a still image of the millimetre paper.
3. Using the aforementioned still image, the FOV and magnification of the cameras are determined.
4. Seeding particles are introduced in the combustion chamber. When the seeding density is sufficient the flow is halted and a still image of the seeded flow is obtained to set and adjust the $f_{\#}$ of the camera and focus the camera on the particles.
5. A very short $\Delta t \approx 1 \mu$ s has been set to check the overlap between the two light beams, by checking the number of particle pairs between the time-separated images. In theory, no particles should be lost between these frames. Simultaneously, the laser pulse intensity has been optimised to show equal particle light intensity in the recorded images between the two frames.

An overview of the specifications of the PIV setup are tabulated in table 4.1.

4.4.2. Separation time optimization

The separation time Δt is the time between subsequent laser pulses. This is an important parameter, as it determines the number of particles which are present in the interrogation window in both exposures. For good PIV results the Δt should be optimized in such a way, the number of particle pairs is large enough. In case of a turbulent flow, the following condition should be met to achieve optimal results.

- The maximum out-of-plane displacement should be smaller than 1/4th of the light sheet thickness

Appropriate values for Δt have been calculated before the experiments, to provide an idea of the order magnitude of Δt . The final iteration window size in the cross-correlation procedure is taken to be 24x24 pixels with an overlap of 75%, to achieve a spatial resolution in the flow of 1230 μ m and a vector spacing of 308 μ m. The pixel size of the sCMOS cameras is 6.5 μ m and the magnification is 0.128/0.127 for both cameras. The calculated Δt has been determined based on the 1/4th sheet thickness limitation, shown in the second row. To get this value, the laser sheet thickness is assumed to be 1 mm and the out-of-plane velocity component

General system specifications	
Field of View camera 1 & 2	130.2 & 131.2 mm
Overlap between both cameras	24.7 mm
Laser sheet thickness	1 mm
Mean particle diameter	0.5 μm
Acquisition frequency	15 Hz
Focal length of the lens for both cameras	105 mm
Depth of focus of camera 1 & 2	24.5 & 24.8 mm
Resolution of camera 1 & 2	19.6 & 19.5 pixel/mm
Magnification of camera 1& 2	0.128 & 0.127
fstop for both cameras	11
Isothermal flow experiments at 17°C	
Δt for case P1/P2	7.5/7.5 μs
Number of images acquired for case P1/P2	2000/1775
Isothermal flow experiments at 320°C	
Δt for case P3/P4	6.5/7 μs
Number of images acquired for case P3/P4	3000/4500
Reacting flow experiments	
Δt for case P5/P6/P7	6/3.5/3.5 μs
Number of images acquired for case P5/P6/P7	1750/1800/600

Table 4.1: PIV setup specifications

is estimated based on a turbulence level of 30% of the in-plane velocity. The table also shows the minimum resolved velocity, assuming 0.1 sub-pixel displacements, based on Δt .

The separation times based on the maximum in-plane displacement of 1/4th of the window size are low due to the small window size required to obtain sufficient spatial resolution in the flow field. The calculated Dynamic Velocity Range (DVR) is 163, and constant for all cases. This ratio between the maximum and minimum resolved velocity (see equation 4.7) is an important quantity to evaluate the performance of a PIV interrogation algorithm.

$$DVR = \frac{U_{max}}{U_{min}} \quad (4.7)$$

For conventional PIV experiments, the DVR is of the order of 100 [41], which means that the current experiment is performing better compared to conventional PIV.

While doing the experiments, the separation time has been optimized manually by comparing instanta-

Velocity [m/s]	35	47	72	96	97
Δt , based on 1/4th out-of-plane disp. (μs)	23.8	17.7	11.6	8.7	8.6
Minimum resolved velocity (m/s)	0.6	0.8	1.2	1.6	1.6

Table 4.2: Estimated Δt for different jet velocities

neous images between both exposures. If the amount of particle pairs is deemed sufficient and the number of particles lost between both exposures is minimized, this Δt has been adopted for the corresponding operating condition. Because the particle velocity varies with changes in operating conditions, level of preheating, and whether or not heat is released, this process has been repeated for all cases separately. The adopted values per experimental case are reported in table 4.1. Care has to be taken, not to lower the Δt too much, as the resulting displacement between both exposures may become too small and the chance of finding random correlation peaks and hence spurious vectors increases. A trade-off is made between sufficient particle motion in the lower velocity recirculation zone and a minimal loss of particles between both exposures in the high-velocity turbulent jet. Moreover, because two cameras have been used, the previous procedure is repeated for both

During the reacting flow experiments, a small rotation of the burner head perpendicular to its axial axis was visible over time. In the ideal case, the laser sheet should be exactly in the middle of the nozzle, perfectly perpendicular to the burner head. In reality, it proved to be very difficult to achieve this. Due to the expansion and deformation of the aluminium frame, under thermal loading, the alignment of the laser sheet was slightly off. This issue will be further discussed in section 4.4.3.

4.4.3. Encountered problems and solution strategies

This sub-section will treat the problems encountered by the author while performing the PIV measurements. Some of these problems that are commonly encountered in reacting flow PIV are also discussed in a publication by Willert and Jarius [43].

Seeding

The degradation of seeding quality presents a real challenge when using solid nonspherical particles. Larger lumps of agglomerated seeding material form over time within the seeder, which reduces the amount of seeding material that is entrained by the flow. This process increases the measurement uncertainty due to an increase in particle slip, a typical issue when the particle diameter increases, and it accelerates the clogging of the seeder exit. During the experimental runs, the lines downstream of the seeding generator were also clogged with larger lumps, reducing the effective diameter and the amount of seeding in the flow. This problem was dealt with by purging the lines in between runs and replacing the seeding material with fresh material every other run. To keep the seeding particles from clogging before being inserted into the seeder vessel, the fresh seeding material was preheated in a small oven at 180°C for 25 minutes.

Another issue related to seeding was the difference in seeding density between both cameras. Due to the expansion of the jet, the density of the flow decreases downstream. This will also reduce the seeding density within the jet. Hence, a lower seeding density is obtained in the second camera as compared to the first camera, closer to the nozzle. To counter this problem, the jet is over-seeded in the first camera, such that sufficient seeding density can be obtained in the second camera. This problem occurred for both the non-reacting and reacting cases.

Window contamination by seeding material

Due to the internal aerodynamics, as will be shown in section 4.5, the seeding particles in the jet impinge onto the glass tube, scratching the surface. The seeding material also tends to deposit on the tube and fuse with the glass under high environmental temperatures, rendering the glass tube optically opaque. Only 60 seconds of experiments per run could be obtained before the tube had to be replaced and cleaned. After every run, the tube had to be cleaned in a water bath to remove the large particles and subsequently in an ultrasonic bath to remove any remaining smaller particles. Even by following this procedure, the tube would become unusable after a certain amount of runs, which meant it had to be refurbished by polishing the inside of the tube. This was done with a handheld angled Proxxon WP/E polishing machine and car headlight polisher. By applying this method, the whole experimental campaign is completed by using only two glass tubes. In an attempt to reduce contamination of the tube, Willert and Jarius propose to use forced-air cooling on the inner windows [43]. In our case this is not possible, as it will influence the internal aerodynamics of the flow and also because it will change the composition of the gas, basically creating a lean environment with the addition of air. Therefore, a cooling flange has been added to cool the outside of the glass tube which reduces the tendency of the seeding particles to stick and fuse with the glass tube. This proved successful as the permanent fusion of the particle with the glass is largely prevented.

Background Noise

When operating under lean conditions $\phi < 1$, the flame exhibits low luminosity, due to the absence of soot in the flame. However, a narrow-band 532nm interference filter has still been used to remove the background noise. A polarization filter has also been applied, to reduce the laser reflections from different surfaces such as the glass tube itself. By reducing the laser power of both pulses, reflections may also be reduced. Especially for the non-reacting flow experiments at 17°C and 320°C, this proved successful. Although some reflections can largely be eliminated you will never eliminate all reflections. During the image pre-processing, before the cross-correlation algorithm is applied, the influence of these reflections on the recorded images is reduced by applying a background subtraction step. The minimum intensity per pixel is subtracted over the whole ensemble set.

Frame deformation under thermal loading

As mentioned in section 4.4.2, the aluminium frame deformed while running the combustor during the experiments. The burner head, which is rigidly mounted in the frame, has been observed to rotate because of this. The heat transfer from the reaction zone to the frame follows two main pathways. A conductive heat transfer component from the burner head to the frame, combined with radiative heat transfer emitting from the reaction zone onto the frame. The latter pathway is enabled by the quartz glass tube used for the PIV experiments. Initially, the issue had been addressed by wrapping aluminium foil around the frame to reflect incoming thermal radiation. This partly solved the problem, however, a rotation of the burner head was still observed. To compensate for the rotation, the laser sheet is aligned slightly off centre with the top nozzle before the experiments are started. Before every experimental run, while running the heated flow through the combustor, the laser sheet had been checked to be aligned with the top nozzle. However, under heavy thermal loading during combustion, the burner head still shifted slightly while the shielded laser optics remained at their set location. This resulted in a small non-alignment between the nozzle and the laser sheet, and hence an out-of-plane component of the jet. This resulted in a reduction in particle pairs found between both exposures in the jet region. To counter this issue, the time separation between laser pulses is decreased. Using a Δt in the order of 3-6 μs this resulted in a sufficient amount of particle pairs for PIV.

The issue of the burner head rotation due to deformation of the frame is visualised schematically in figure 4.5. The rotation in image 4.5b is an exaggeration of the observed rotation.

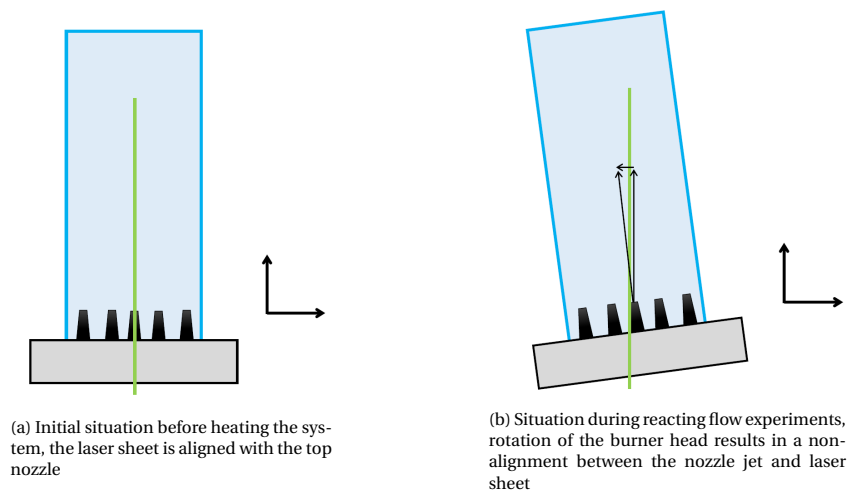


Figure 4.5: Schematic of the burner head rotation due to deformation of the frame under thermal loading. The shown rotation is an exaggeration of the observed rotation

4.4.4. Image processing procedure

Pre-processing

Acquisition of the images is done using the Davis 8.4 software package. The pre-and post-processing is done using the Davis 10.0 software package. For every operating point, between 2000 and 5000 images are recorded over several different runs, under similar conditions. In the pre-processing phase of the image processing procedure, the main aim is to increase the particle image quality. This is done by a minimum subtraction

Window size	Weight	Overlap (%)	Passes	Vector Post Processing
64x64	1:1	50	1	Remove if Q<1.1
24x24	1:1	75	3	Remove if Q<1.1

Table 4.3: PIV post-processing steps, equal for all cases

procedure. For the whole set of images recorded, the minimum intensity per pixel is determined and this is subtracted from all images in the set. This process removes the background noise in the recorded images.

Using a masking procedure, regions of low particle density or high seeding deposition are masked out from the frames. These regions will create spurious vector data and as such are not useful to our discussion.

Quality Check

In between experimental runs, the quality of the recorded images is constantly checked by cross-correlating random image pairs throughout the obtained set. By checking the instantaneous peak ratio and velocity fields, as an example see figure 4.7, a rough estimation of the general quality of the data set is obtained. After the experiments, all data sets have been reviewed and the best quality images from the different sets are selected to be used in the statistical analysis of the flow field.

Post-processing

The PIV post-processing parameters are tabulated in table 4.3. The final window size of $w \times h = 24 \times 24$ pixels results in a spatial resolution in the flow field of approximately $1230 \mu\text{m}$. Estimating the Kolmogorov length scale, a rough estimation of the smallest scale turbulence in the flow is provided. The Kolmogorov length scale is defined by relation 4.8

$$\eta = \left(\frac{\nu^3}{\epsilon} \right)^{1/4}. \quad (4.8)$$

The values for ν and ϵ have already been determined in the evaluation of the Kolmogorov time scale. Using these values, $\eta = 16.9 \mu\text{m}$. The resolution of the PIV in this case is $w/\eta = 1230/16.9 \mu\text{m} = 73$ Kolmogorov. The current setup is thus not able to resolve the micro scale turbulence characteristics and associated energy dissipation. However, this resolution is large enough to resolve the macro scale and intermediate scale (taylor scale) flow characteristics, which include the energy transfer from the larger to the smaller scale turbulence. This approximation assumes isotropic turbulence and is purely dependent on the fluid mechanics properties. The influence of heat release under reacting conditions is not taken into account.

Image stitching

To extend the field of view, the images of the two cameras are stitched together. This creates an image of the flow with a higher resolution than would have been possible using a single camera. The overlap of the two images is obtained from cross-correlation between two instantaneous images.

4.4.5. Flow field statistics

The flow field statistics have been calculated for the three different operating conditions. Calculate the Root-Mean-Square (RMS) of the velocity fluctuations and the Turbulence Intensity (TI).

The RMS of the turbulent velocity fluctuations is given by u' following

$$U' = \sqrt{\frac{1}{2}(u'^2 + v'^2)} \quad (4.9)$$

and TI according to

$$TI = \frac{\sqrt{\frac{1}{2}(u'^2 + v'^2)}}{U_{ref}} \quad (4.10)$$

with U_{ref} the local centreline mean velocity U_c .

The Reynolds shear stress in the x-y plane is calculated according to

$$R_{xy} = \langle u' v' \rangle \quad (4.11)$$

4.4.6. Uncertainty Estimation

The uncertainty estimation of PIV results is important in quantifying the validity of the obtained results. Using commercially available software for the post-processing of PIV such as DaVis, underlying problems with data quality that may influence the resulting flow field remain hidden. Many times the software will still produce plausible results, even when the recorded images are of lower quality due to illumination issues, out-of-window particle motions, or under-seeding of the flow.

Measurement uncertainty on velocity

Because the PIV data processing method is based on the correct estimation of the particle displacements within an interrogation window, the uncertainty in displacement estimation strongly influences the resulting velocity flow field. In a review paper by Sciacchitano [44] on the uncertainty estimation in PIV, different sources of uncertainty are discussed. According to this paper, the measurement uncertainty on the velocity is a combined effect of the uncertainty on the particle displacement, uncertainty on the separation time and uncertainty on the magnification. These terms are dealt with separately in a Taylor series propagation as derived by Sciacchitano [44].

$$\left(\frac{U_u}{u}\right)^2 = \left(\frac{U_{\Delta X}}{\Delta X}\right)^2 + \left(\frac{U_{\Delta t}}{\Delta t}\right)^2 + \left(\frac{U_m}{M}\right)^2 \quad (4.12)$$

With $U_{\Delta t}$ the uncertainty on the separation time, U_M , the uncertainty on the magnification factor, and $U_{\Delta X}$, the uncertainty on the particle displacement. The uncertainty on the magnification factor is assumed negligible when the system is properly calibrated. The uncertainty on the separation time is a Type B uncertainty, it cannot be determined by a statistical approach to the experimental ensemble, and it has to be given by the manufacturer of the laser system. In subsonic flow regimes with Δt larger than $1\mu s$, this uncertainty can be disregarded as the influence is negligible [44]. This leaves the uncertainty on the velocity to be dominated by the uncertainty of the particle displacement. Different approaches to determining this uncertainty are also discussed by Sciacchitano [44]. One of the approaches uses the SNR metric. This approach has been proposed by Charonko & Vlachos [45] and Xue [46]. The idea is to quantify the PIV displacement uncertainty directly from the information contained in the cross-correlation plane [45]. The correlation plane represents the combined effects of various sources of error that govern the accurate estimation of particle displacements. It contains uncertainties related to the used cross-correlation algorithm, reflections and background noise, and uncertainties from finite spatial resolution. These uncertainties are contained within the noise superimposed upon the intensity of the image pattern. A well established measure of the SNR is the Primary Peak Ratio (PPR), the ratio of the primary peak to the secondary peak in the cross-correlation plane, equation 4.13, [46]. The definition of the PPR is visualised in figure 4.6. Where the primary peak and secondary peak are denoted by $C(0)$ and C_2 respectively.

$$SNR \propto PPR = \frac{C(0)}{C_2} \quad (4.13)$$

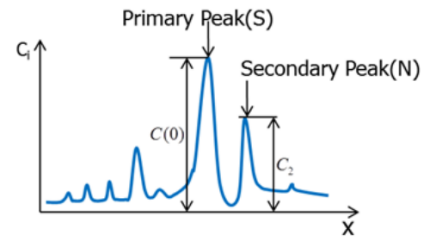


Figure 4.6: 1-D visualisation of PPR [46]

To reduce the influence of this uncertainty, the PPR metric is continuously evaluated during the acquisition of the data. Figure 4.7a shows the primary peak ratio distribution of such an instantaneous velocity field, seen in 4.7b. The upper and lower limit of the colour bar is set to 1.5 and 1.0 respectively. Most of the PPR field is red, this means that the $SNR > 1.5$. The figure also shows the influence of reflections on the tube, which have a lower PPR. As a rule of thumb, if the PPR is larger than 1.2, this is considered a valid displacement. It is therefore assumed, as long as the $PPR > 1.5$, the influence of uncertainty is small and hence the image quality is deemed good for post-processing. The influence of this uncertainty is reduced by increasing the image density N_I , and the removal of background noise. In the current approach, this is achieved by recording over 1000 images per operating point and removing the minimum intensity per pixel over the whole ensemble set. The uncertainty of the velocity varies both with time and spatial location, making it computationally difficult

to evaluate this for every instantaneous image. According to Sciacchitano [44], several studies investigated the propagation of this uncertainty to the statistical quantities of interest. These random uncertainties of the instantaneous measurements are included in the standard deviation of the mean. For the current research, we are only interested in the statistical properties of the flow, hence, this approach is also valid here. This approach is further discussed in the next paragraph.

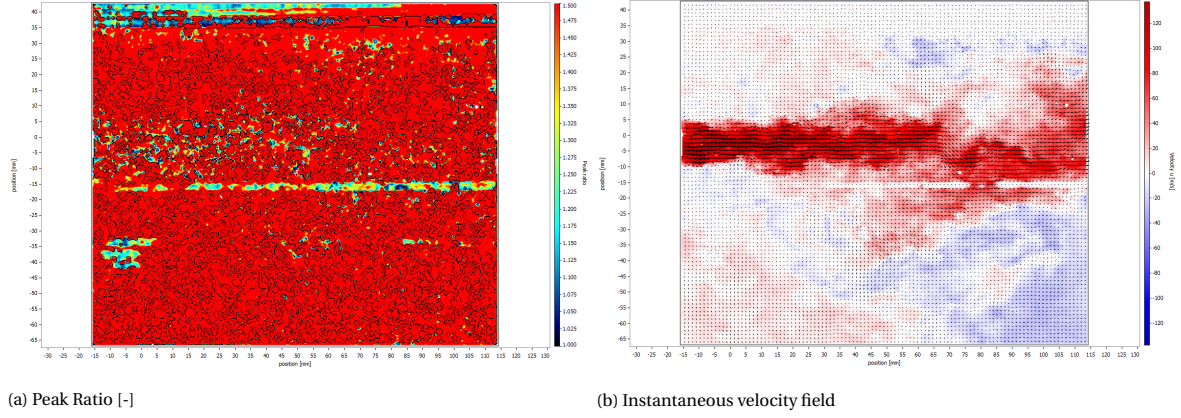


Figure 4.7: Peak ratio of PIV cross-correlation for respective instantaneous flow field for the reacting case 1.

Uncertainty from tracer particle fidelity

The error estimation based on the correlation plane only considers error sources contained within the recorded images. Uncertainties due to particle slip are not taken into account, this parameter is thus evaluated separately. The lag between the particle and fluid velocity step, the slip velocity (u_{slip}), is already discussed in terms of the Stokes number. The slip velocity is approximated according to:

$$u_{slip} \approx \tau_p \cdot a_p \quad (4.14)$$

With τ_p the particle slip time and a_p the particle acceleration. The particle slip time for different types of seeding particles including different TiO_2 materials have been experimentally studied by Ragni et al [47]. The value found for TiO_2 with a primary crystal size of 550nm is $2.78\mu\text{s}$ in the de-hydrated state. According to Sun [48], if steady flow is assumed, equation 4.14 can be rewritten as

$$u_{slip} \approx \tau_p \cdot (V \cdot \nabla V) \quad (4.15)$$

This relation holds in a region without the presence of a strong vortex. The divergence of the velocity (∇V) in equation 4.15 can be estimated using the DaVis software package. The divergence of a vector field describes the behaviour of the field, does it behave like a source or a sink? An outgoing flux is defined as positive and an ingoing flux is defined as a negative divergence. A quick review of this error showed the influence to be very small $<1\%$. This value is therefore assumed to be of negligible influence.

Finite ensemble size uncertainty

As discussed in section 4.4.6 the statistical uncertainty resembles the combined effect of different sources of random uncertainty in PIV measurements. The statistical uncertainty is strongly dependent on the ensemble size of the calculated statistics.

The uncertainty of the mean, RMS velocity fluctuations and Reynolds Shear Stress (RSS) are a function of the finite ensemble size, following the relations introduced by Benedict & Gould [49] and reproduced by Sun [48]. The uncertainty of the mean velocity is estimated as

$$\epsilon_{\bar{u}} = \frac{\sqrt{\overline{u'^2}}}{\sqrt{N}} = \frac{\langle u' \rangle}{\sqrt{N}} \quad (4.16)$$

Where N is the ensemble size, and $\langle u' \rangle$ the Root-Mean-Square (RMS) of the velocity fluctuation.

The uncertainty of the RMS of the velocity fluctuation is estimated as

$$\epsilon_{u'} = \frac{\sqrt{\overline{u'^2}}}{\sqrt{2N}} = \frac{\langle u' \rangle}{\sqrt{2N}} \quad (4.17)$$

The uncertainty of the Reynolds shear stress is estimated as

$$\epsilon_{u'v'} = \frac{\sqrt{1 + R_{uv}^2} \sqrt{\overline{u'^2}} \sqrt{\overline{v'^2}}}{\sqrt{N}} \quad (4.18)$$

Where R_{uv} is the correlation coefficient

$$R_{uv} = \frac{\overline{u'v'}}{\sqrt{\overline{u'^2}} \sqrt{\overline{v'^2}}} \quad (4.19)$$

For turbulence studies, a minimum of 1000 images is considered safe to obtain properly resolved PIV results with low ensemble size uncertainties [49]. This statement only holds if those samples are uncorrelated in time. For the current research, this is assumed to be the case. This requirement has also been adopted as the minimum sample size per operating condition for the current experimental campaign. The statistical uncertainty is included in the centreline plots that have been extracted from the planar flow field. The results are presented in the next chapter.

4.5. Results

The results of the planar PIV experiments are given in this chapter. The results are subdivided into two sections. The first will discuss the results related to the mean velocity field. The second will discuss the results related to the turbulent velocity field. The contour plots presented in this section are positioned vertically, whereas the actual setup is positioned horizontally, this is done for ease of comparison. The centreline of the combustor is located around $r/d_{noz}=0$. The combustor wall is located towards the right side of the image, just beyond $r/d_{noz}=15$. The combustor wall is not imaged because only spurious data is obtained in the near-wall region due to reflections and curvature of the wall itself. The nozzle centre is located around $r/d_{noz}=9.5$ and the burner head itself is located just below $x/d_{noz}=0$ outside the FOV. The case definition as presented in table 3.1 is used in the current discussion. Cases 1 and 2 indicate mass flows rates corresponding to a condition of $P=60\text{kW}$, $\phi=0.8$ and 0.6 respectively. Case 3 corresponds to the reacting flow case with nitrogen dilution. The leading abbreviation R indicates reacting flow, NR_H indicates the non-reacting isothermal flow at 320°C , and NR indicates the non-reacting isothermal flow at 17°C .

4.5.1. Mean velocity field

Figure 4.8a displays the normalized axial velocity contours with flow streamlines overlaid. Plotting streamlines is a powerful tool to characterize the fluid flow field because it shows the main flow features, an indication "of where the flow is going", it also shows if the flow is either accelerating or decelerating. The flow is accelerated in areas where streamlines converge, and in areas where streamlines diverge, the flow is decelerated. For the current case, with a highly turbulent jet, the flow is considered to be unsteady. The use of streamlines is thus limited to showing the streamline characteristics, indicating the general flow structures of the average flow field.

Figures 4.8(a-b) show how the jet entrains and accelerates the surrounding fluid particles. Streamlines, by definition, can not intersect; therefore, the surrounding fluid's mixing into the jet is not visible. Two different recirculation zones are observed in figures 4.8(a-b); the Peripheral Recirculation Zone (PRZ), between the jet and the wall, and the Central Recirculation Zone (CRZ), extending from the jet towards the combustor centreline. The CRZ centre of recirculation (CR) is located upstream of the PRZ centre of recirculation. Nonetheless, the PRZ seems to capture streamlines further upstream compared to the CRZ. The streamlines recirculating into the CRZ are captured further downstream, which indicates a difference in gas composition between the CRZ and PRZ. The CRZ CR lies close to the nozzle mouth, at less than $10 x/d_{noz}$ away. This result seems to be in accordance with the flow field characteristics obtained from CFD by Vaz, see figure 1.4 in section 1.2. The stagnation points (SP) that close the PRZ are located at $x/d_{noz}=0$ and $x/d_{noz}=22$. The CRZ stagnation points are both not visible in this figure. The downstream stagnation point is located beyond the upper edge of this

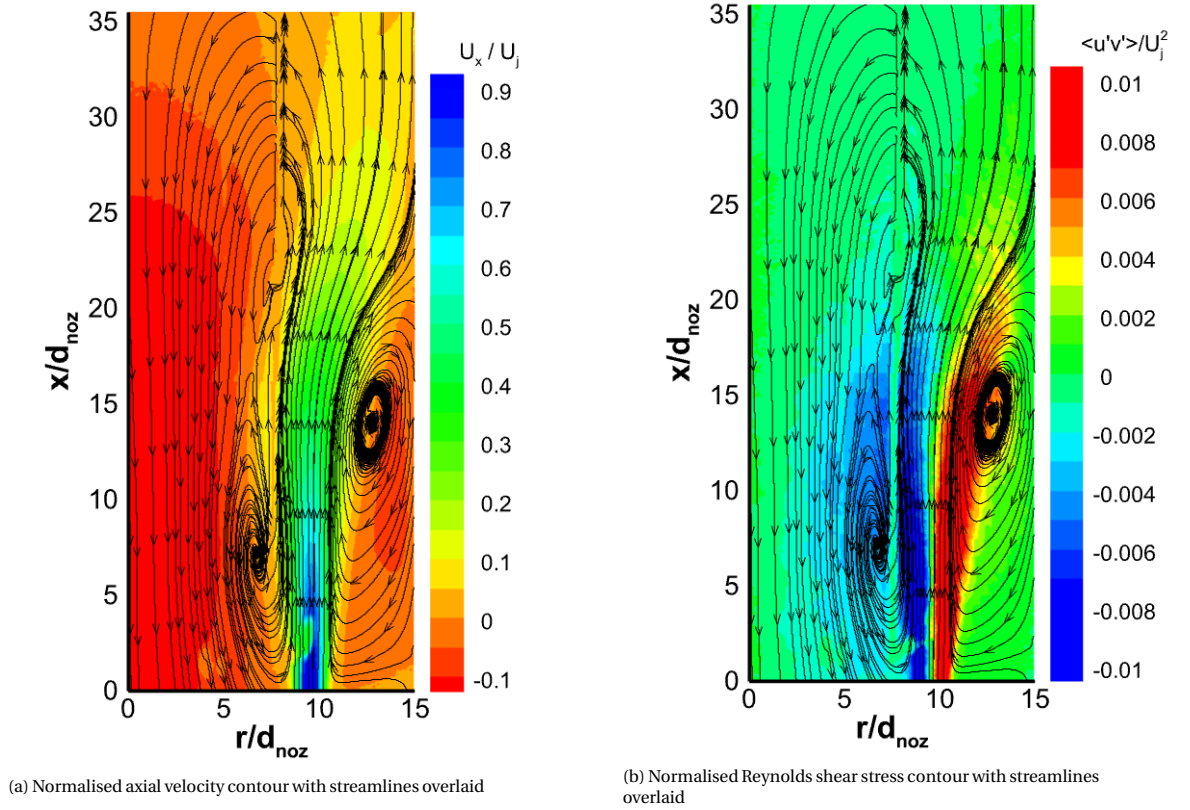


Figure 4.8: Large scale flow structures for the case R1

figure. The CRZ upstream stagnation point is located at the burner head face. The length of the central recirculation zone, the L_{CRZ} , is the distance between the face of the burner head and the downstream closing stagnation point of the CRZ [8]. For the current setup, this can not be determined accurately, as the closing stagnation points are outside our FOV. The combined FOV of the two cameras does not capture the full extend of the CRZ. Moreover, it is located just downstream of the nozzle exit plane because the line of sight towards the nozzles is obstructed by the cooling flange, as seen in figure 4.4.

Figures 4.8(a-b) shows the jet to bend towards the combustor wall at $x/d_{noz} \approx 15$, the same axial location as the CR of the PRZ. The bending of the jet is characteristic behaviour of a jet near a wall, called the Coanda effect. The entrainment of the surrounding fluid by the high momentum jet creates low-pressure zones on both sides of the jet that are filled by the surrounding fluid. This is also the driving phenomenon behind the PRZ and CRZ, the flow recirculates to equalise the pressure near the jet. However, due to the presence of the wall near the PRZ, insufficient flow is available to flow into the lower pressure zone. Hence, a pressure difference is created between both sides of the jet. The flow bends towards the lower pressure side, and the jet attaches to the wall.

Figure 4.9 presents the normalised axial velocity (U_x/U_j) contours obtained with planar PIV for the reacting, and isothermal non-reacting flow cases at 320°C and 17°C. The velocities are normalised by the maximum velocity on the jet centreline. The velocity half-width lines (dashed lines) and jet centreline (dot-dashed line) are superimposed onto the contour plots. The jet centreline is tracked by taking the maximum axial velocity over a radial line at discrete positions along the combustion chamber centreline. The velocity half-width lines are defined as the radial position where the axial velocity is reduced to 50% of the jet centreline value $U_{r_{1/2}} = 0.5U_c$. Significant similarities between the reacting and non-reacting velocity fields are revealed in the figures 4.9(a-c). The initial spreading of the jet, tracked by the velocity half-width lines, over the first 15 x/d_{noz} is similar for all cases. Past this point, all flow fields display a similar bending of the jet towards the combustor wall and show the PRZ and CRZ at approximately the same axial locations. Nonetheless, the curvature of the jet seems to be more gradual for the reacting flow case. Because the flow expands more under heat release, the jet will occupy more space, limiting the jet's ability to curve towards the wall. The jet centreline and velocity half-width lines are observed to be attached to the wall downstream from $x/d_{noz}=25$ and 28, respectively,

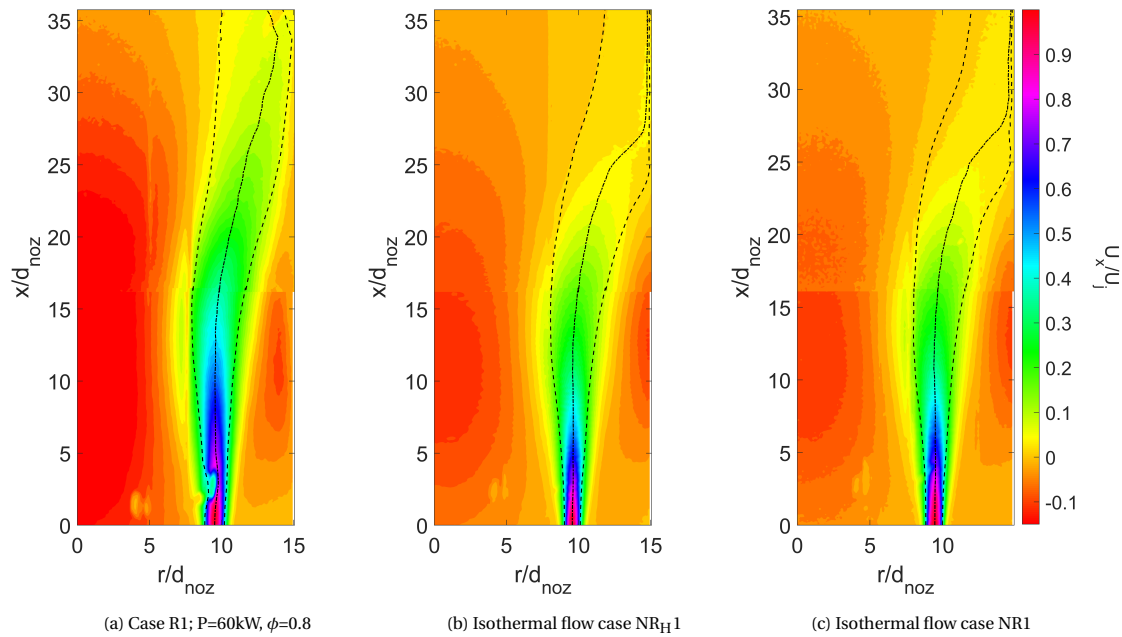


Figure 4.9: Contour plots of axial velocity for the reacting and non-reacting isothermal flow cases

for cases NR_H1 and NR1. This behaviour is assumed unrealistic and originates from the FOV that does not extend to the wall. Jet centreline data near the edge of the image, downstream from $x/d_{noz}=28$ is therefore omitted from the centreline plots in figures 4.11 and 4.22. The most obvious differences in velocity field are found in the strength of the recirculation zone, which seems to be stronger for the case R1, where the highest negative velocities are observed.

Figures 4.10(a–c) display the normalised axial velocity contours for the different reacting flow cases R1-3. All contour plots show very similar behaviour. Although it may seem that the PRZ is weaker for case R3, this results from low-quality PIV data in this region rather than a difference in the flow field. Laser reflections in the flow field are observed close to the jet centreline ($r/d_{noz} \approx 9$), together with two small patches close to $r/d_{noz}=5$. These laser reflections overexpose the camera sensor at those pixel locations, resulting in spurious vector data.

Figure 4.11 shows the normalised mean velocity (U/U_j) decay along the centreline of the jet. The black and blue lines represent the isothermal flow at 17°C and 320 °C, respectively, while the red lines describe the reacting flow cases. The triangular markers represent conditions and flow rates at $P=60\text{kW}$ and $\phi=0.8$, case designation '1'. The star markers represent conditions and flow rates at $P=60\text{kW}$ and $\phi=0.6$, case designation '2'. Finally, the square marker represents the diluted condition and flow rates at $P=60\text{kW}$ and $\phi=0.8$, with $N_2=450\text{NLPM}$, case designation '3'. Error bars indicating the uncertainty in the measured values are not shown in this figure, as it would become too packed with information. Instead, the minimum and maximum uncertainty is calculated and presented in table 4.4. The axial velocity decay along the jet centreline with the measurement uncertainty included is found in appendix F, figure F1.

Figure 4.11 shows the jet velocity to decay as the jet expands downstream. For the cases NR1-2 and NR_H1-2, the centreline velocity decays faster, showing an almost exponential decay along the jet axis. This is in contrast to turbulent free jet data available in the literature, where the centreline velocity decay mostly follows a linear behaviour, examples presented by Xu et al. [50] and Ball et al. [51]. The differences in the rate of decay between the non-reacting and reacting flow cases are explained by the heat released from combustion that accelerates the flow. This same phenomenon also explains the red line corresponding to case R1 consistently showing higher values than the other reacting cases R2 and R3. The divergence in the rate of decay between the reacting and non-reacting cases begins at $x/d_{noz}=3$. This may be seen as an indication of the onset of the flame zone within the combustor. The rate of decay reduces beyond $x/d_{noz}=18$, at which location the jet starts to bend towards the wall. Beyond $x/d_{noz}=30$, the curve flattens as the jet attaches to the wall.

Figures 4.12 to 4.15 show the radial profiles of normalised axial velocity at different locations along the length of the combustion chamber. The velocity profiles are normalised to the jet centreline velocity at that

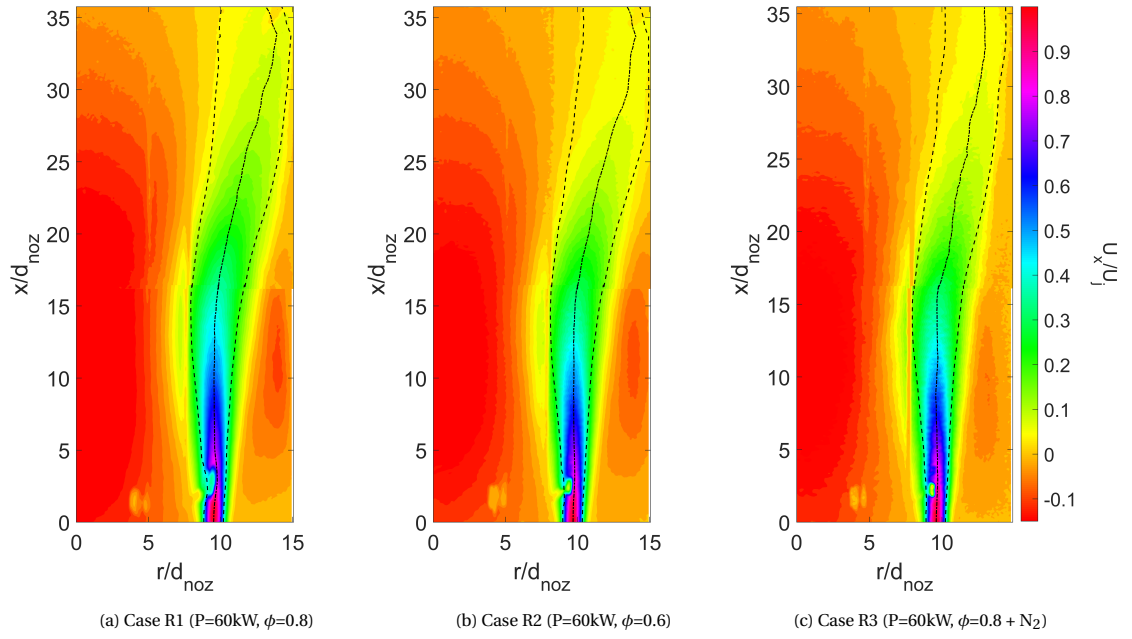


Figure 4.10: Comparison of axial velocity flow field contours for different reacting flow cases

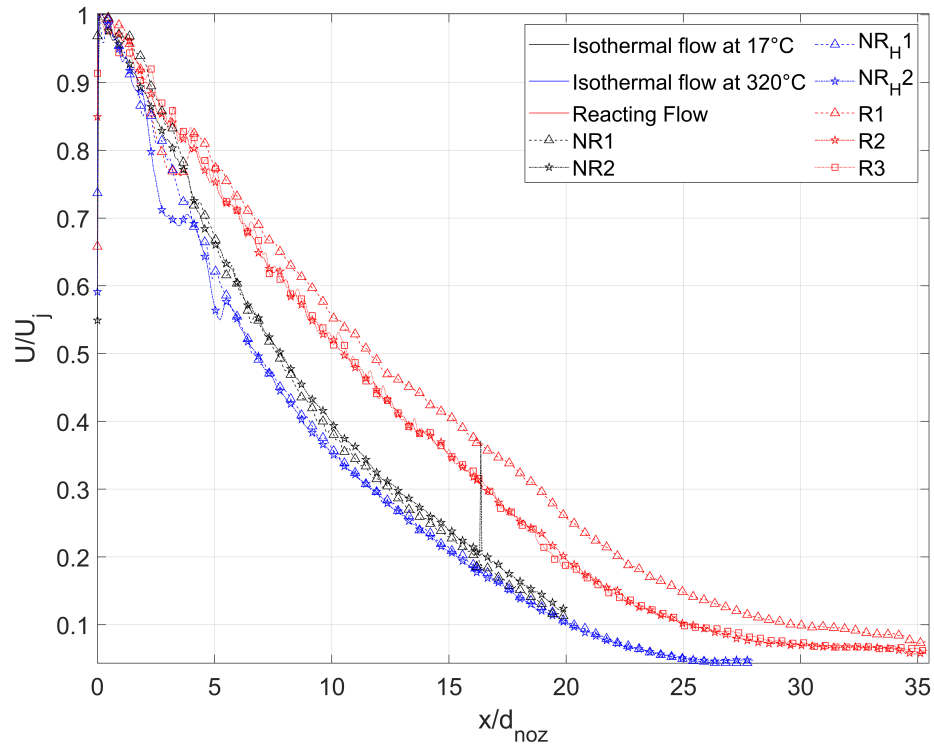
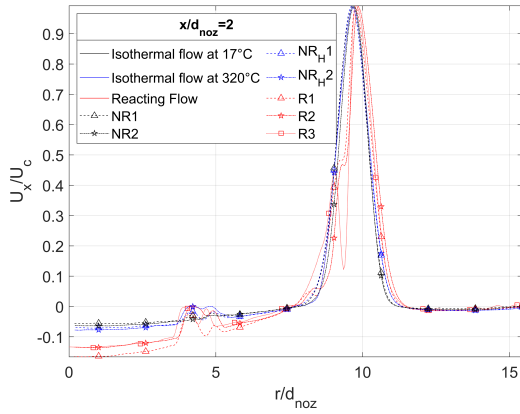
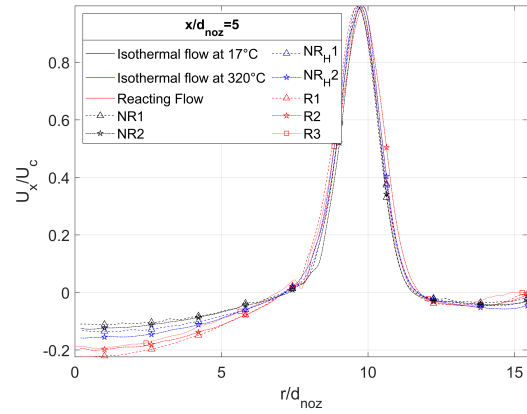
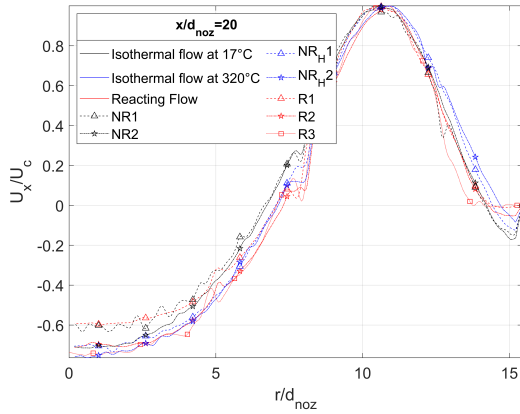
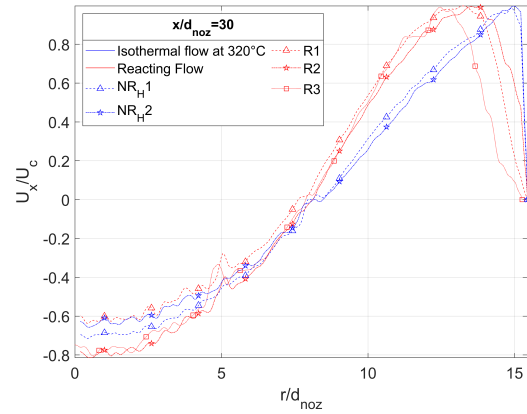


Figure 4.11: Axial velocity distribution along the jet centreline

Case	$\epsilon_{\bar{u}} \min (U/U_j)$	$\epsilon_{\bar{u}} \max (U/U_j)$
NR1	0.0014	0.0099
NR2	0.0014	0.0245
NR _H 1	0.0009	0.0057
NR _H 2	0.0010	0.0075
R1	0.0023	0.0088
R2	0.0021	0.0076
R3	0.0036	0.0138

Table 4.4: Uncertainty of the mean velocity per operating condition, normalised with U_j Figure 4.12: Normalised radial velocity profiles at $x/d_{noz}=2$ Figure 4.13: Normalised radial velocity profiles at $x/d_{noz}=5$ Figure 4.14: Normalised radial velocity profiles at $x/d_{noz}=20$ Figure 4.15: Normalised radial velocity profiles at $x/d_{noz}=30$

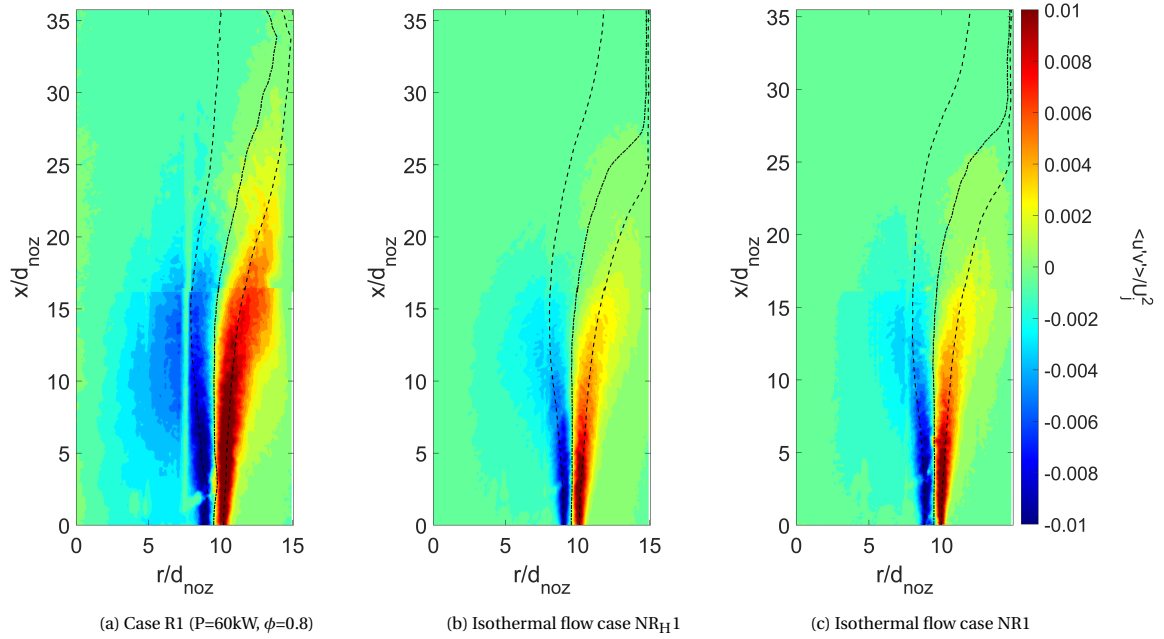


Figure 4.16: Contour plots of Reynolds shear stress for the reacting, hot and cold flow cases

location. The velocity profiles in figures 4.12 and 4.13 show similar behaviour in the jet region and the PRZ. The jet profile seems to be independent of the Reynolds number in the near field region ($x/d_{noz} < 5$) for all operating conditions investigated. Figures 4.8(a-b) reconfirm the observation of the jet widening and shifting outwards towards the wall when moving downstream due to the expansion and curvature of the jet. Downstream at $x/d_{noz}=30$, the jets are fully attached to the wall for cases NR_H1-2. Similarly to the observation from figures 4.9(a-c), the reacting flow jet is not yet fully attached as the peak in axial velocity is still a couple of nozzle diameters away from the wall. Differences between the reacting and non-reacting velocity profiles are also observed in the CRZ region ($0 < r/d_{noz} < 7$), where the negative velocity becomes relatively larger in the case of reacting flow conditions compared to the non-reacting cases. This results from the heat release, which significantly accelerates the flow recirculating through the CRZ. This same difference is not observed in the PRZ, moreover, it seems the opposite is the case at an axial position of $x/d_{noz}=20$. This asymmetry in velocity profile also causes an asymmetry in velocity gradients between the CRZ and PRZ. Due to the no-slip boundary condition at the wall, the velocity has to be zero at that position. The velocity gradient is already zero at $x/d_{noz}=12$. At the centre of the CRZ, the velocity gradient has to be zero, however, the velocity itself does not have to be zero. A non-zero velocity gradient is thus observed over a wider region in the CRZ, compared to the PRZ, up to $x/d_{noz}=2$. Under reacting conditions, the velocity gradient in the CRZ is also seen to be larger compared to the non-reacting cases.

4.5.2. Turbulent velocity field

The Reynolds shear stress (R_{xy}) distribution, normalised with the square of the maximum jet centreline velocity ($\langle u'v' \rangle / U_j^2$), and with the flow streamlines overlaid, is presented in figure 4.8b. The highest shear stress values are found in the shear layer between the turbulent jet and the recirculating environment outside the jet. Positive values are seen at the interface between the jet and the PRZ, with higher shear stresses at the location of the centre of recirculation of the PRZ at $x/d_{noz}=14$ and towards the point where the jet attaches to the wall. The negative values of shear stress seem to be distributed over a larger region towards the centre of the combustion chamber. This again coincides with the interface of the jet and the CRZ, including the centre of recirculation at $x/d_{noz}=7$. However, this region seems to extend further downstream, where a second smaller centre of recirculation is formed. This is at the location where the jet starts to curve towards the wall.

Contour plots of the Reynolds shear stress for cases R1, NR_H1, and NR1 are shown in figures 4.16(a-c). As discussed in the previous section, the peak in R_{xy} coincides with the shear layer between the jet and both the PRZ and CRZ, at which location the greatest exchange of momentum occurs. Moreover, the highest values

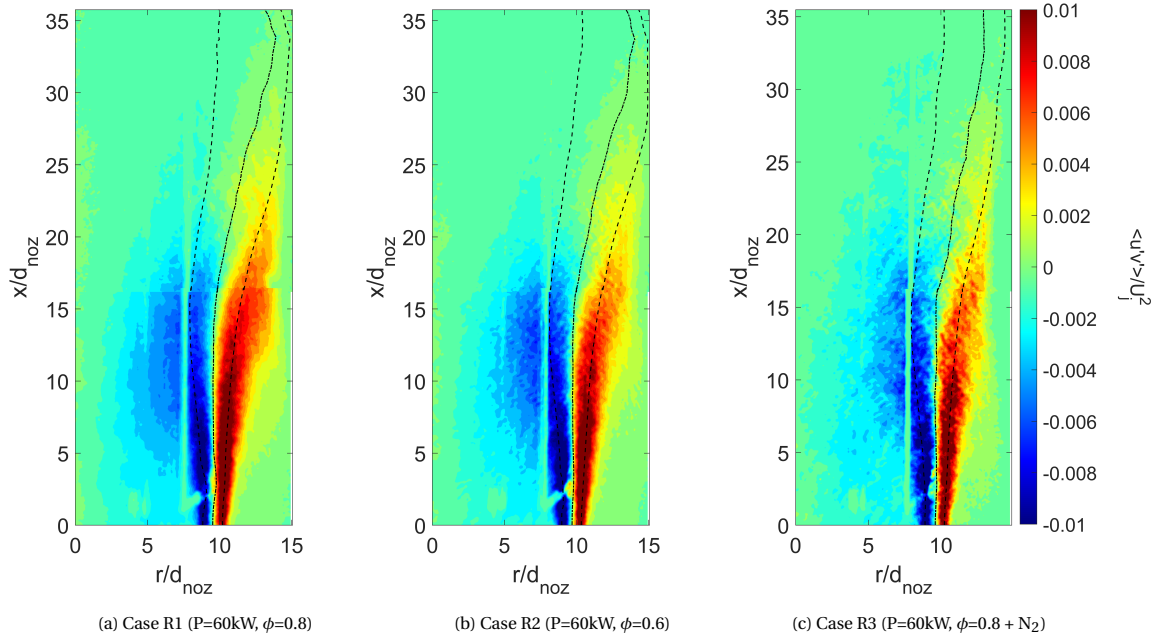


Figure 4.17: Comparison of Reynolds shear stress contours for different reacting flow cases

of R_{xy} coincide with the velocity half-width lines. Figures 4.16(a-c) show the high R_{xy} region for case R1 to be much wider compared to the cases NR_H1 and NR1. For the non-reacting cases, the R_{xy} distribution is only centred around the velocity half-width line. The region of high shear stresses does not extend further into the PRZ or CRZ. Furthermore, higher values of Reynolds shear stress extend more towards the centreline rather than the wall. The rate of decay in shear stress is also higher for the non-reacting cases, and the values have drastically reduced beyond $x/d_{noz}=15$. This indicates that the large-scale turbulent structures in the flow dissipate away quicker in case of an expanding non-reacting jet flow. These results for the first 15 x/d_{noz} are similar to the results found in the literature on a turbulent free jet [50]. The extension of the high shear stress regions is related to the previously discussed velocity gradients in the flow. The production term in the turbulence kinetic energy equation is a function of the velocity gradient. Due to the flow acceleration under heat release, the velocity gradient in the CRZ is increased resulting in larger values of turbulence and shear stress towards the combustor centreline. The difference between the CRZ and PRZ follows the same explanation, where the velocity gradient reaches zero quicker in the PRZ compared to the CRZ.

Figures 4.17(a-c) show the similarities in R_{xy} distribution between the different reacting flow cases. The highest Reynolds shear stress values are located around the jet half-width lines for all cases. The negative values of shear stress seem to be distributed over a larger region in the CRZ compared to the positive values in the PRZ. Although the highest velocity gradient near the combustor centreline is observed for the case R1 (figures 4.12 and 4.13), this does not result in an observable difference in values of R_{xy} towards the combustor centreline.

Radial profiles of Reynolds shear stress normalised by the mean velocity at the jet centreline are presented in figures 4.18-4.21. The peak in shear stress shifts outwards with respect to the jet centreline and the shear layer itself widens with an expansion of the jet in the downstream direction. Further downstream, the relative strength of the Reynolds shear stress increases due to the combined effect of decay in the mean centreline velocity and an increase in mixing between the jet and its surroundings. These findings are in line with results obtained for a turbulent round free jet as published by Ball et al. [51]. Interestingly, the normalised peak values of R_{xy} for the reacting flow cases seem to be lower than their non-reacting equivalents downstream at $x/d_{noz}=15$. This might be explained by the higher jet centreline velocity at this location, as observed from figure 4.11. This difference is less obvious at the other axial positions due to the smaller difference in jet centreline velocity. On the other hand, the spread in measured data seems to be higher for the reacting flow cases, especially for case R3. For the latter, this is most likely a result of lower accuracy of the PIV data due to the sample size being 4 times smaller compared to the other reacting flow cases and 5 to 6 times smaller compared to cases NR_H1-2. In the far-field, $x/d_{noz}>30$, the variance in measured data increases for both

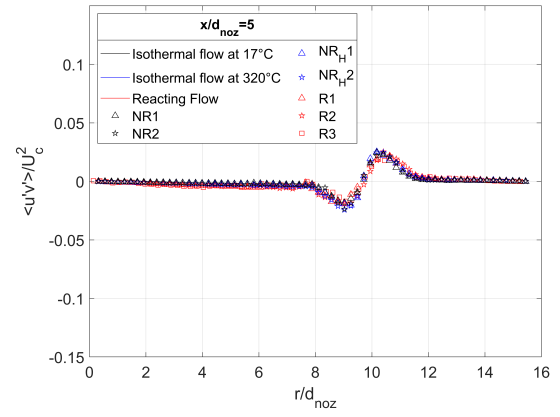
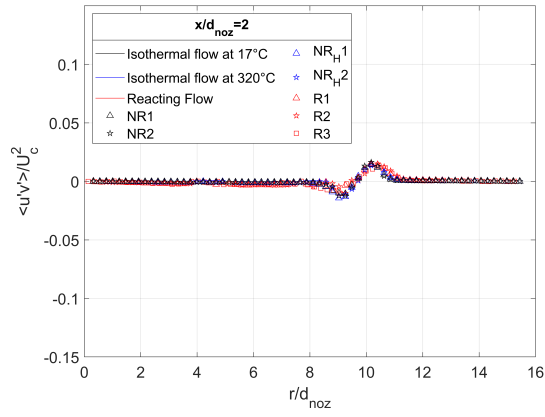


Figure 4.18: Normalised Reynolds shear stress profiles at $x/d_{noz}=2$ Figure 4.19: Normalised Reynolds shear stress profiles at $x/d_{noz}=5$

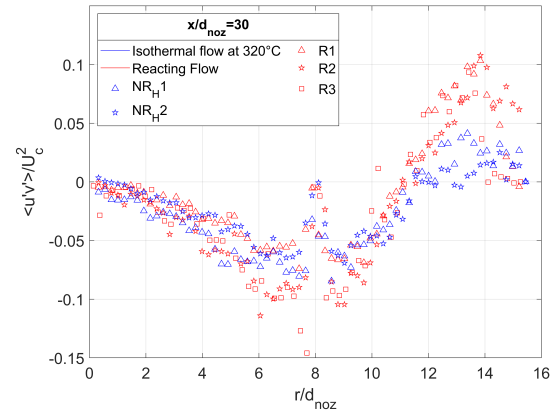
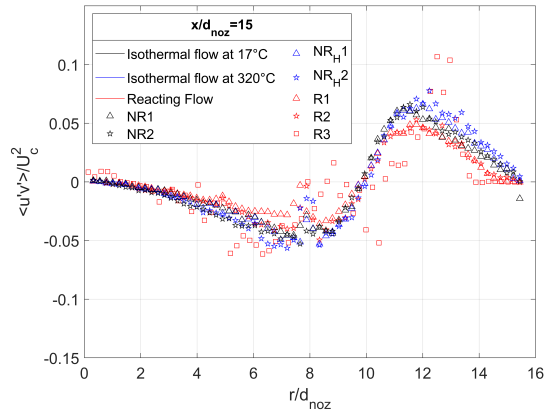


Figure 4.20: Normalised Reynolds shear stress profiles at $x/d_{noz}=20$ Figure 4.21: Normalised Reynolds shear stress profiles at $x/d_{noz}=30$

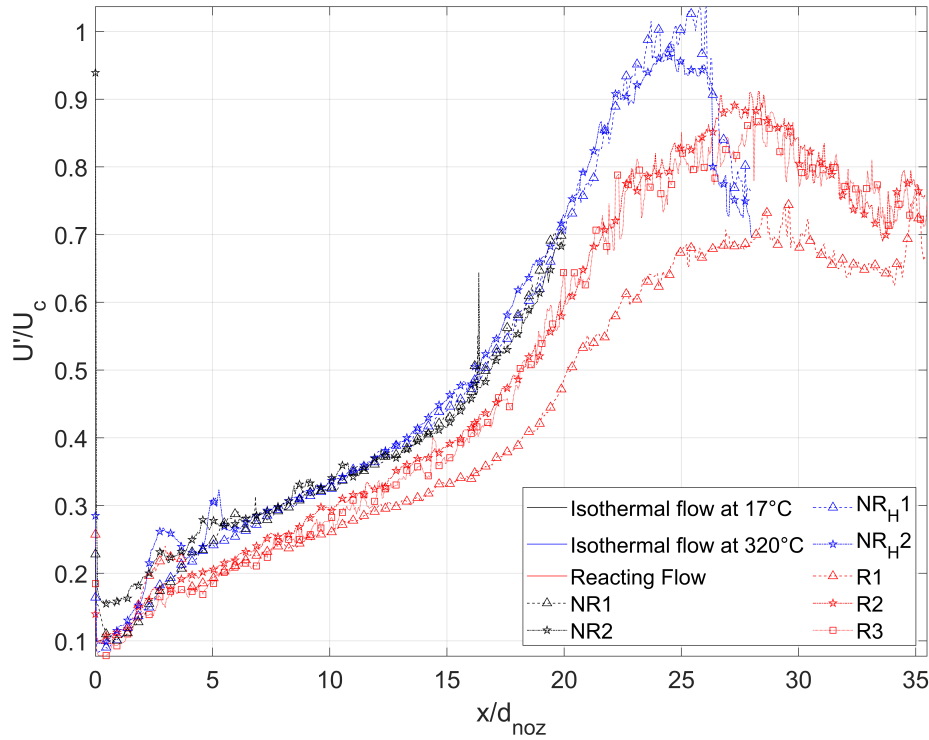


Figure 4.22: Turbulence intensity distribution along the jet centreline

the non-reacting isothermal flow at 320°C and reacting cases due to the expansion of the jet and increase in turbulence.

Figure 4.22 shows the turbulence intensity (U'/U_c) along the jet centreline. The calculated uncertainty on the measured value is tabulated in table 4.5. The turbulence intensity along the jet centreline with the measurement uncertainty included is found in appendix F, figure F2. For the first 15 x/d_{noz} , the jet resembles a 'free jet', expanding and mixing with the surrounding fluid in the downstream direction, increasing the turbulence intensity. Initially, all lines collapse onto each other, only beyond $x/d_{noz}=3$ the reacting flow lines start to deviate and show a consistently lower value. This is consistent with the flow behaviour seen in figure 4.11. It seems that the turbulence intensity is decreased in a hot environment, indicating the position of the flame. Although all lines display similar behaviour up to $x/d_{noz}=15$, the reacting flow U'/U_c lies consistently below the non-reacting isothermal flow cases. Furthermore, beyond $x/d_{noz}=10$, the line corresponding to case R1 begins to deviate from the other reacting flow lines. The difference in non-reacting and reacting flow development is explained by increased gas viscosity with an increase in temperature.

For the reacting flow cases, the higher viscosity due to the presence of a flame will dampen the velocity fluctuations. This also explains the observed difference in turbulence intensity between the case R1 and both cases R2 and R3. The latter two have similar adiabatic flame temperatures, resulting in similar TI trends. The influence of viscosity with temperature is not observable between the isothermal flow cases NR_{H1} and NR_{H2}. This is most probably due to the smaller difference in temperature between both.

Just beyond $x/d_{noz}=15$, all lines show a higher rate of increase in turbulence intensity. This point corresponds to the axial location where the flow curves towards the combustor wall and starts to resemble a jet near a wall. The turbulence intensity for cases NR_{H1} and NR_{H2} seem to stabilise on a lower level, following a significant drop in turbulence intensity beyond $x/d_{noz}=25$. This drop is smaller and postponed until $x/d_{noz}=28$ for the reacting flow cases. These axial locations coincide with the jet centrelines reaching the near-wall region, see figures 4.16a-4.17c. For a turbulent free jet, the turbulence intensity value stabilises at a high value further downstream, without showing this drop in turbulence intensity [50] and [52]. The current results thus indicate that the turbulence kinetic energy dissipates near the combustor wall. Macrostructures in the flow lose their energy via the energy cascade to the point where the microstructures are reached. At

Case	$\epsilon_{<u'>} \min (U'/U_c)$	$\epsilon_{<u'>} \max (U'/U_c)$
NR1	0.0031	0.0358
NR2	0.0051	0.0373
NR _H 1	0.0021	0.0268
NR _H 2	0.0027	0.0278
R1	0.0033	0.0257
R2	0.0033	0.0304
R3	0.0036	0.0578

Table 4.5: Uncertainty of the velocity fluctuation per operating condition, normalised with U_c

this small scale, the turbulent kinetic energy is lost through friction. This dissipative process occurs primarily near the wall, where the largest velocity gradients are observed. Because the non-reacting jet's centreline is closer to the wall than the reacting flow jets, the wall influence propagates more rapidly towards the jet centreline. The reacting flow jets experience a more gradual drop in turbulence intensity along the wall, conform the more gradual change in the flow direction of the jet centreline along the wall.

5

Temperature Measurements

Temperatures can be measured in different ways by intrusive thermocouple measurements and non-intrusive optical methods. In the early stages of this thesis research, it is attempted to obtain flow field density gradients and possibly temperature by applying the Background Oriented Schlieren (BOS) technique. Unfortunately, this did not yield any useful results. Therefore, it has been decided to focus efforts on applying thermocouples. This chapter will thus focus on the methodology and results obtained from thermocouple measurements. Some of the results obtained by the BOS method on the combustor can be found in the appendix A.

A thermocouple is a flow intrusive measurement device which is inserted into the flow to measure the local temperature. Thermocouples are very well suited to be used in a high-temperature environment such as combustion systems. Their governing principle is based on the electrical potential between the measuring terminal and a reference terminal. The difference in temperature between the two terminals creates a voltage potential, which, dependent on the materials used in the device, provides a reading of this temperature difference.

5.1. Theoretical Background

The working principle of the thermocouple is based on the thermoelectric effect, the conversion of a temperature difference between the two sides of the device to an electric voltage. The thermoelectric effect in the case of thermocouples is called the 'Seebeck effect'. The thermocouple consists of two thin wire legs composed of different metals. The legs come together and are welded in the middle at the Thermocouple Junction or measuring point, the 'hot' end. When the temperature at the measuring point rises or drops, the electron density in both metal legs also changes. The altered value of the electron density, the voltage, is measured at the end of the wires at the reference junction, the 'cold' end. This measurement of the voltage potential is proportional to the temperature difference between the hot and cold ends for the two dissimilar materials. The thermocouple now only provides a relative temperature reading, not an absolute temperature. Another temperature sensor measures the temperature at the reference junction, which, combined with the relative temperature, provides an absolute temperature reading at the measurement point. This procedure is called 'cold junction compensation'. The different types of thermocouples indicate the different metals that are used in the legs and may be selected based on the temperature range and sensitivity needed.

5.1.1. Different types of thermocouples

Fine-wire thermocouples

Fine-wire thermocouples are particularly suited for combustion research. They consist of very thin wires ($\approx 15\text{-}80\mu\text{m}$), often made of platinum alloy, supported by a slightly thicker fork ($\approx 350\text{-}500\mu\text{m}$) of the same material, cemented in a slender stem. This kind of thermocouple is relatively small and hence has a negligible influence on the flow field [53], it will not act as a flame stabiliser. Moreover, the response time is very short, because of the small wires that have a small thermal capacity. Next to this, the influence of radiative heat transfer with the wall is negligible, due to the small surface over which radiation is emitted. The downside of the bare fine-wire layout is the heat release by radical recombination reactions that can occur on the

thermocouple surface in a reacting environment [8]. This will affect the heat balance around the hot junction and thus the measured temperature.

Shielded thermocouples

An alternative approach to using a bare fine-wire thermocouple is the shielded thermocouple. In this particular configuration, the measurement bead is shielded from the reactive environment and from radiative heat losses to the combustor wall. The bead can either be in direct contact with the shielding material at the tip, or in indirect contact, where a pocket of still air separates the bead from the shield. The latter solution allows for the thermal expansion of the wires connecting to the bead, preventing the bead from exercising too much pressure onto the shield, which might damage it. For this kind of thermocouples, it is important to have a shielding material that has both high thermal conductivity and a high temperature limit. The high conductivity allows for a quick response of the system to a change in temperature.

Suction pyrometers

Another type of shielded thermocouple is the suction pyrometer. This particular configuration also protects the bead from radiative heat losses to the combustor walls. Only now, hot gas is extracted from the flow through an annulus and past the sensor to measure the temperature. In this case, the heat transfer occurs predominantly by convection.

5.2. Setup

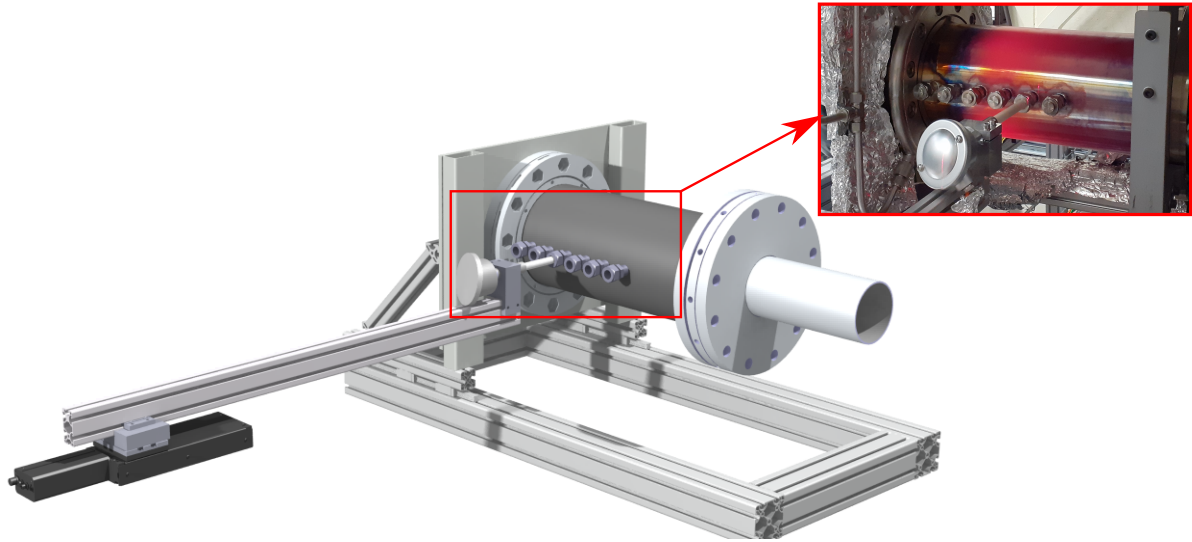


Figure 5.1: Render of the setup with combustion chamber and thermocouple mounted on linear traverse

In the present combustion system, a shielded thermocouple is used. A schematic of the used thermocouple is shown in figure 5.2. The outer diameter of the probe is 15mm, the total length is 245mm of which 165mm is shielded by a ceramic tube. The ceramic tube is connected to an aluminium stem of 80mm long and 22mm in diameter. This allows the thermocouple to be clamped onto the traverse system. The ceramic shield has a wall thickness of 3mm and is made from KER710 ceramic material (99.7% Al_2O_3). The thermocouple itself is an S-type thermocouple that can measure temperatures up to 1600°C. As seen in figure 5.2, the measurement bead is located in a small pocket inside the inner tube. This reduces the view factor for radiative heat transfer between the bead and the surrounding ceramic tube.

The thermocouple can be inserted into the steel combustion chamber through one of 6 ports that are welded onto the steel tube. In this experimental campaign, the probe has been inserted through ports 3 and 5, these ports are marked red in figure 5.3. Port 3 and 5 are located at an axial distance of 140mm and 240mm respectively from the face of the burner head.

The thermocouple has been mounted on a rectangular beam of 1.5 meters long that is mounted on a Zaber traversing system. The beam is used to create distance between the Zaber and the combustion chamber to protect the Zaber from the radiative heat. With the Zaber, the probe can be traversed to specific radial

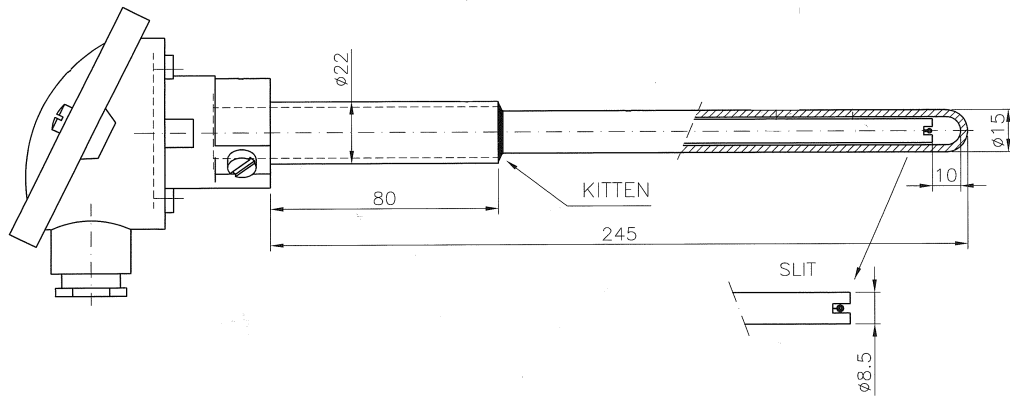


Figure 5.2: Schematic of the shielded thermocouple, highlighted the positioning of the measurement bead at the tip

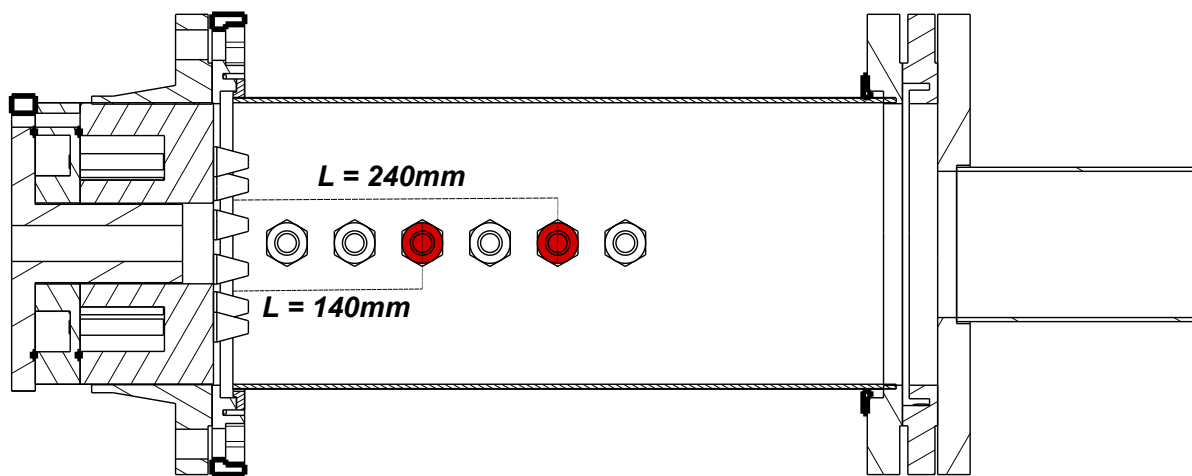


Figure 5.3: Schematic overview of the combustor including burner head, with port 3 & 5 marked in red

positions with very high accuracy, of around 0.01mm. This reduces uncertainties on the positioning and data sampling time of the thermocouple if done manually. In addition, with an automated system, a sequence of points can be provided as an input, such that the Zaber will go through the provided sequence automatically. A render of the full system is shown in figure 5.1, with the Zaber traverse shown in black.

5.3. Methodology

5.3.1. Measurement procedure

Radial measurements have been performed at an axial distance of 140mm and 240mm from the face of the burner head. The location of these measurements is highlighted in red in figure 5.3. The first location is assumed to be close to the reaction zone, while the other is further downstream. Most measurements are performed at port 3, as this provides radial temperature profiles indicative of the flame temperature under varying conditions. The measurements are taken at 5 discrete radial positions starting at the wall and extending towards the combustor centreline.

Before startup, the thermocouple is aligned to be in the centre of the access port, to reduce friction with the port wall when traversing inwards. At the same time, the position of the thermocouple tip is verified to be at the wall. During startup and heating up of the combustor, the thermocouple is kept at the wall position. When a steady-state condition is achieved at the target operating condition, the traverse is slowly moved inwards to the first measuring point. When the target location is reached, data measurements are taken. There is a small delay of a couple of seconds before the data acquisition is started. This is done to allow the thermocouple to reach a steady temperature at the target location. This time delay is verified by the live temperature output which is monitored, only when the temperature seems to have reached a steady-state

value, measurements are taken. The measurements are taken for 200 seconds, with an acquisition rate of 10Hz, this results in a data set of almost 2000 samples per radial position. After all the measurements have been completed for a certain operating condition, the thermocouple is traversed back to the wall, where it stays while the operating point is changed.

Traverse measurements have been performed to obtain radial temperature profiles at port 3 for a variation in equivalence ratio 0.6-0.9 at 50 and 60kW. The platinum thermocouple is used as it has a rapid response time. The thermocouple is traversed very slowly with approximately 0.18mm/s towards the centre of the combustor. This allows for investigating the value and location of the peak temperature and how the temperature profile changes with operating conditions.

5.3.2. Temperature correction method

The measured temperatures are corrected for thermal radiation losses. In order to do so, the heat influx and outflux are balanced according to equation 5.1. In this equation, the radiation influx from the wall and the surrounding hot gas, together with convective heat transfer from the flow, are balanced with the radiative heat loss from the probe to the environment

$$h_{c,g} T_g + \epsilon_{tc} (\sigma \epsilon_g T_g^4 + \sigma \epsilon_w T_w^4) = \sigma \epsilon_{tc} T_{tc}^4 \quad (5.1)$$

With ϵ_{tc} the emissivity of the ceramic thermocouple, ϵ_g the emissivity of the surrounding gas, and ϵ_w the emissivity of the combustor wall. The local gas temperature is given by T_g , the wall temperature by T_w , and the thermocouple temperature by T_{tc} . Equation 5.1 is solved for T_g at different radial positions in the combustion chamber. However, near the wall, equation 5.1 is simplified to equation 5.2, where the convective heat transfer from the flow and the radiative effect from the gas are assumed zero. The probe is radially retracted to a position at the wall, where the flow velocity is taken as zero due to the no-slip condition at the wall. Equation 5.2 is solved for the wall temperature T_w .

$$\epsilon_{tc} \sigma \epsilon_w T_w^4 = \sigma \epsilon_{tc} T_{tc}^4 \quad (5.2)$$

To estimate the convective heat transfer coefficient $h_{c,g}$, local velocities at the thermocouple tip are estimated from the velocity data obtained for different operating conditions from PIV. To calculate $h_{c,g}$ the Nusselt correlation by Churchill and Bernstein [54] is used, given as

$$Nu = 0.3 + \frac{0.62 Re_D^{1/2} Pr^{1/3}}{\left[1 + \left(\frac{0.4}{Pr}\right)^{2/3}\right]^{1/4}} \quad (5.3)$$

Where Pr is the Prandtl number and Re_D the Reynolds number for the probe in a cross flow.

5.3.3. Uncertainty estimation

An intrusive thermocouple such as the one presented in figure 5.2 causes significant disturbances in the temperature and velocity field.

Influence of probe intrusion

The probe-induced disturbances can have a significant influence on the flow field. Especially in recirculating flows, these disturbances can be so severe that they may change the local mixing characteristics of the flow [53]. Due to its diameter of 15mm, more than twice the diameter of the nozzles, the probe will act as a bluff body to the flow. This phenomenon has also been observed during small experiments with a laminar burner. A photo of the influence of the probe on the laminar flame is seen in figure 5.4a. When the probe had been inserted into 'the flame' the flame would actually flow around the thermocouple, like the flow around a bluff body, the probe did not necessarily penetrate the flame.

Influence of thermal and chemical effects

This measurement technique is vulnerable to different sources of measurement inaccuracies and errors, which will influence the results. Two important sources of error are *catalytic heating* and *heat transfer processes* [8]. Catalytic heating occurs in reducing environments, those containing hydrogen, water vapour and carbon monoxide. However, due to the use of a ceramic insulated thermocouple, the thermocouple wires are not in direct contact with the reactive environment, and this source of error is not applicable to the current situation.

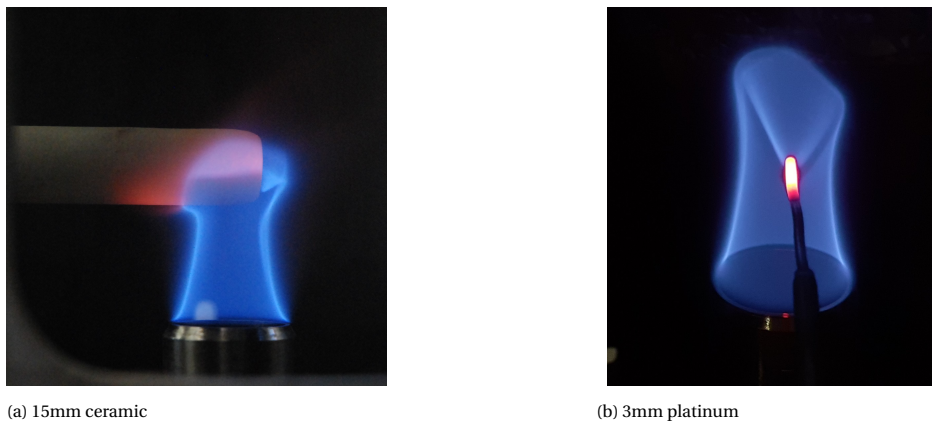


Figure 5.4: Influence of the thermocouple on a laminar flame

A steady-state difference between the measured temperature and the actual gas temperature can always be observed in thermocouple measurements because of heat transfer effects. Heat transfer occurs between the thermocouple hot junction, the ceramic insulation tube, and surrounding surfaces. Heat transfer occurs by both conduction and radiation. Conduction through the wires is mainly a function of the wire length and can only be decreased by reducing the wire diameter [53]. However, a small heat flux will always be present due to the temperature difference between the hot junction and the colder section further down the wire. The influence of the conductive effect is minimised by slowly traversing the thermocouple, to minimise the temperature gradient over the thermocouple length. For the current campaign, the effect of conductive heat transfer over the length of the thermocouple has not been considered as it is assumed that this temperature gradient is very small because the thermocouple is allowed to reach a steady-state condition before measurements are taken. The heat transfer from the hot junction through the ceramic insulation tube to the outside surface is also assumed to be negligible, because in steady-state, without active cooling, the measurement point will reach the same temperature as the surrounding ceramic shield. Heat transfer between the thermocouple surface and its surroundings is the main heat transfer process in this case and will be further discussed in the next section 5.3.2.

5.4. Results

Temperature measurements are performed at 5 discrete radial positions within the combustion chamber at port 3. These points range from a position at the wall up to the combustor centreline, see figure 3.6. The temperatures measured by the ceramic shielded thermocouple are corrected for radiation losses according to the above-described procedure. These values, together with the un-corrected values, are presented in figure 5.5.

The correction has not been applied for the measurements at a radial position of 10mm from the wall. There was no velocity data available that close to the wall. Therefore, the 'corrected' data point is equal to the raw data at this location. All measurements have been recorded at a power setting of 60kW, with a variation in equivalence ratio and level of dilution. These conditions resemble the cases investigated with PIV. In figure 5.5, the blue symbols represent the base case $P=60\text{kW}$ and $\phi=0.8$, case G27, the red symbols correspond to $P=60\text{kW}$ and $\phi=0.6$, case G25, and the orange symbols represent the case with dilution by N_2 , case G28. The radial temperatures show a significant decrease in temperature near the wall for all cases. This is explained by convective and radiative heat losses to the environment. The convective heat loss is increased by the external cooling of the combustion chamber. It further implies the system can not be considered to be adiabatic as the air used for cooling is lost to the environment. The case of $\phi=0.6$ and the case with N_2 dilution display very similar behaviour, with almost equal temperature readings at all radial locations. For the locations near the wall (up to 10mm), the temperature for case $\phi=0.8$ is similar to the other two. Outside the region of influence of the wall, the values start to diverge. The temperature gradients for the diluted and $\phi=0.6$ cases are lower and show a more uniform temperature distribution compared to the base case.

The raw measured data is consistently lower than expected for such conditions. To exemplify, the uncorrected wall temperature of 400°C is inconsistent with the observed heating of the chamber at that location. As can be seen in figure 5.1, the steel tube becomes red/orange glowing hot during operation, which would indi-

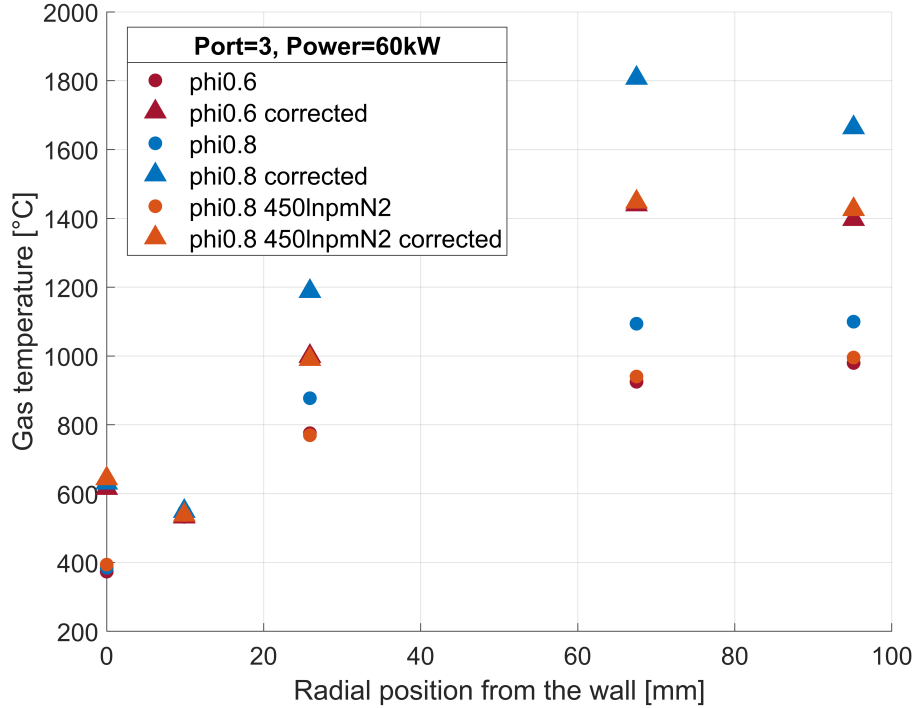


Figure 5.5: Raw and corrected gas temperatures obtained with the ceramic thermocouple for different operating points at 60kW, with $\phi=0.6/0.8$ and N_2 dilution at port 3

cate a wall temperature of 700-800°C. It seems the gas temperature is under-predicted by the thermocouple, a substantial temperature correction is thus required.

The corrected temperatures are much higher, with a peak at 1800°C for the base case. The temperatures for the $\phi=0.6$ and diluted cases are consistently lower near the centre, because of flame cooling through either the addition of additional excess air or N_2 . As seen in figure 5.5, the calculated correction is indeed large, especially towards the centreline. For the case of $\phi=0.8$ the correction is in the range of 40-60% of the measured temperature near the centre. For the other two cases, this is 40-50%. According to Heitor and Moreira [53], bare-wire thermocouples show a radiation loss of 10% of the measured temperature at 1527°C. The use of a ceramic coating might increase radiation losses by a factor of 2, however, the currently calculated correction is still a factor 2 or 3 larger. This is most likely due to the large external surface of the ceramic probe, with a diameter of 15mm, resulting in a high level of radiative heat transfer between the probe and the wall. Such a large temperature correction is not desired and therefore, it is decided to invest in a platinum alloy thermocouple that is slimmer, with a diameter of only 3mm. The measurements have been repeated with the platinum thermocouple to compare it with the results obtained with the ceramic thermocouple.

The thermocouple measurement comparison is shown in figures 5.6-5.8, for the three different operating conditions. The platinum thermocouple (Pt TC) measurements have also been corrected, following the same procedure as for the ceramic thermocouple. The maximum temperature correction is only 10% of the measured value, similar to the results presented by Heitor and Moreira. For the positions near the wall (up to 25mm from the wall), the corrected ceramic thermocouple temperature seems to be quite similar to the uncorrected values obtained with the platinum thermocouple. The corrected wall temperature measured with the platinum thermocouple is around 800-850°C. Towards the centre of the combustion chamber, the values are starting to diverge. The corrected values for the ceramic thermocouple seem to overestimate the gas temperature substantially when compared with the corrected temperatures measured by the platinum thermocouple. Nonetheless, the general trend is the same for the measurements with both thermocouples. A significant drop in temperature is observed near the wall and a relatively constant temperature near the centre of the combustor in the CRZ. Two distinct regions can be identified, a region influenced by the heat loss near the wall (up to 25mm), and a centre region where the gas temperature is nearly constant (25-95mm).

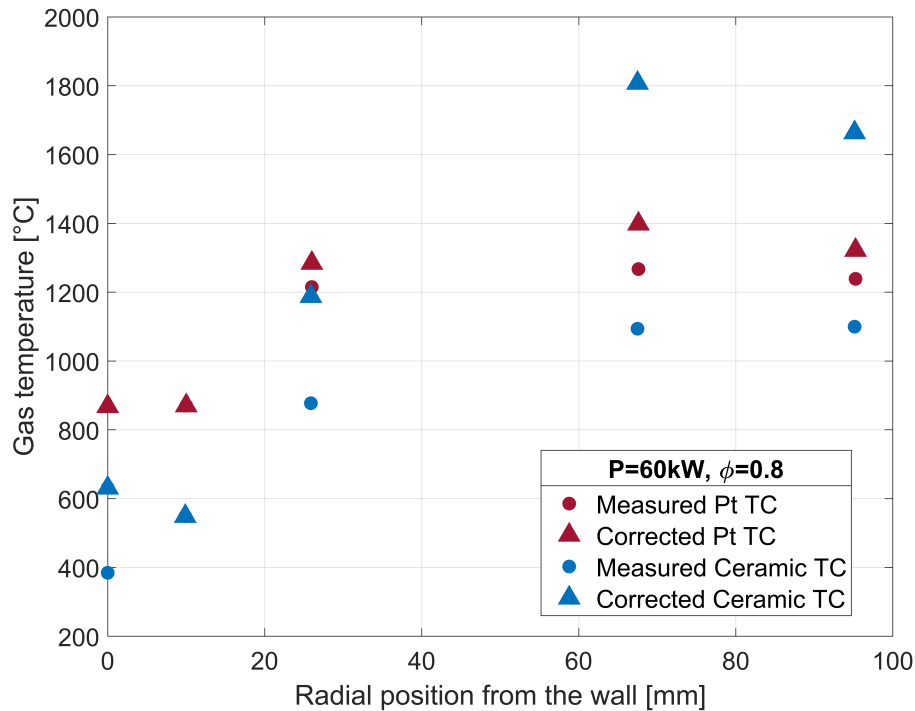


Figure 5.6: Ceramic and platinum thermocouple measurements compared, for $P=60\text{kW}$ and $\phi=0.8$ at port 3

Even though this axial location (port 3) is assumed to be near the reaction zone, a distinctive reaction zone or hot jet region, characterized by a peak in temperature is not observed. That might be due to the coarse spatial resolution of the measurements. Adding radial data points or performing a slow continuous traverse measurement could provide more details on the local temperature field.

The variation in centreline temperature with the operating conditions is shown in figure 5.9, only corrected temperatures are presented here. Because the velocity field data is only available for selected operating points at 60kW, there is no accurate estimate for the velocity in the vicinity of the probe for other operating points. It is assumed the velocity field would not change drastically with these operating points and hence the velocity data from the case of $P=60\text{kW}$ and $\phi=0.8$ is used in the heat balance for the other operating points as well. The measured temperature increases with both equivalence ratio and power setting. For the two lower power settings (30 and 40kW), the gradient is smaller over the range of equivalence ratio compared to the two higher power settings. Finally, the maximum centreline temperature obtained over this experimental campaign is 1375°C, for the case of 60kW and $\phi=0.9$.

Performing slow continuous traverse measurements (with a traversing speed of 0.18mm/s), radial profiles of temperature are obtained, see figures 5.10 and 5.11. The traverse measurements are validated with previously obtained point measurements at the same conditions and locations. These point measurements are presented by triangular markers in both plots. The plots show a gap in the radial profiles. These gaps are due to the applied temperature correction, or rather the lack thereof. At the wall, a different correction is applied, adhering to the no-slip condition at the wall. For the first 10mm from the wall, the measured temperature is not corrected, due to the absence of reliable PIV data in this region. Therefore, the corrected data over this range is omitted from the plot. For most operating points, the radial temperature profiles reach similar temperatures as the point measurements. The traversing method is thus validated to create an accurate temperature profile within the combustor. The only notable difference is observed for $P=50\text{kW}$ and $\phi=0.8$. For this case, the point measurements do not correlate well with the radial profile. The radial temperature profile at this condition is very similar to the same at 60kW. Therefore, the radial profile is still assumed to be correct, and the point measurements at this condition are considered unreliable. The radial profiles are indicative of the relative change in temperature profile with changing operating conditions.

Both figures 5.10 and 5.11 show that peak temperatures are reached near the radial position of the nozzle, most notable for the cases with equivalence ratios of $\phi=0.8$ and 0.9. The peak temperature is seen to reduce

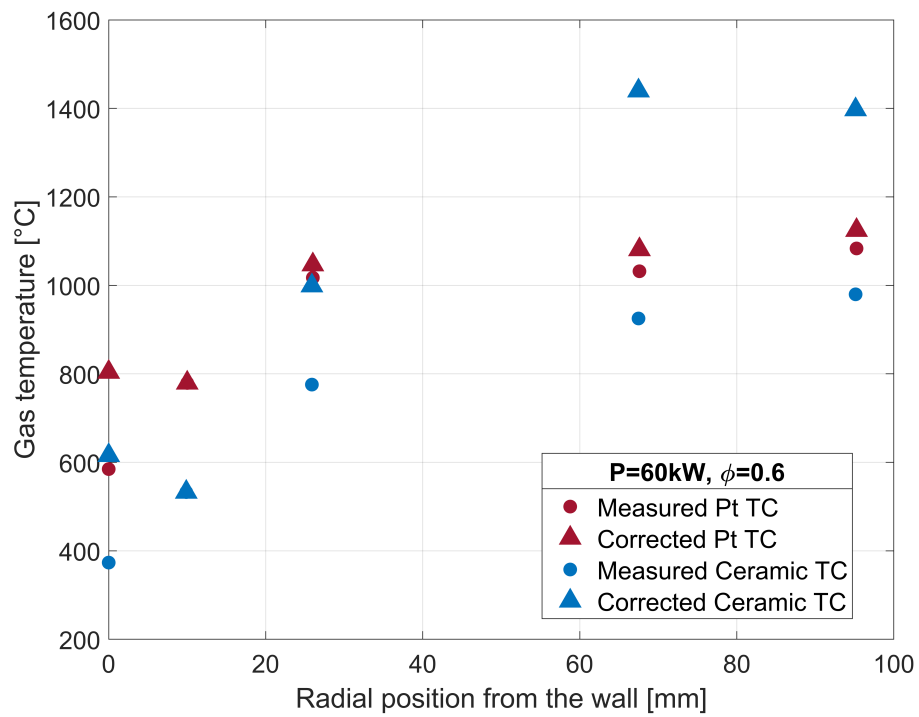


Figure 5.7: Ceramic and platinum thermocouple measurements compared, for $P=60\text{kW}$ and $\phi=0.6$ at port 3

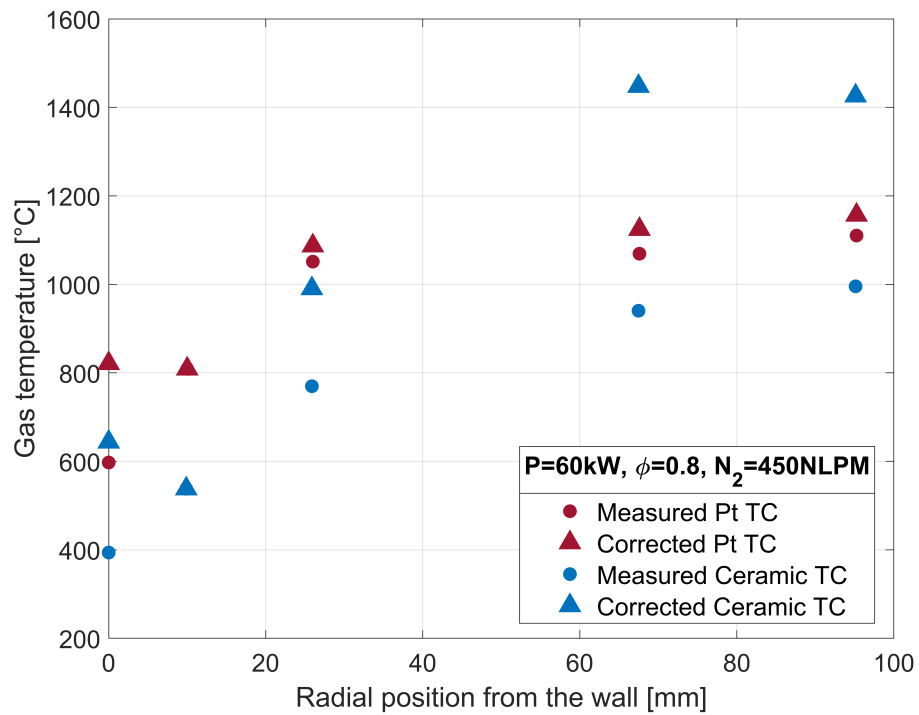


Figure 5.8: Ceramic and platinum thermocouple measurements compared, for $P=60\text{kW}$, $\phi=0.8$ and $N_2=450\text{NLPM}$ at port 3

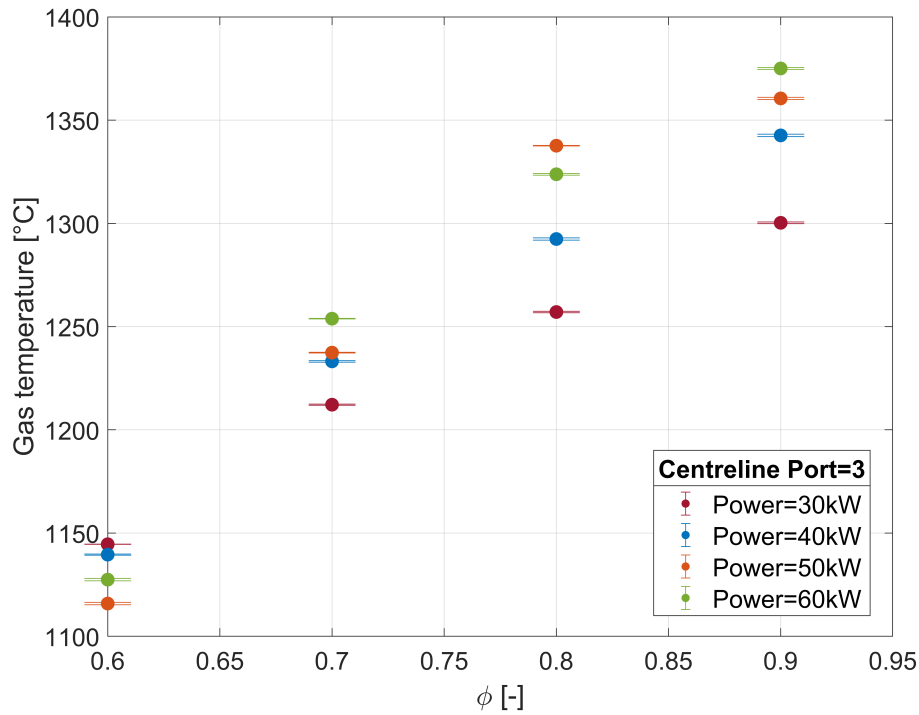


Figure 5.9: Measured gas temperature for a variation in power settings and equivalence ratio at port 3

with a reduction in equivalence ratio. Moreover, both figures show the temperature profiles to become more uniform with a decrease in equivalence ratio, which indicates distributed combustion.

The temperature profiles seem to be largely independent of thermal power input. For the same equivalence ratios at 60kW, the measured temperatures are only slightly higher compared to the case of 50kW. For both conditions, the highest temperature is reached for $\phi=0.9$, measuring 1500°C. The temperatures show a strong gradient near the wall, due to heat loss to the environment. Towards the centreline of the combustor, a mild temperature gradient is observed. This shows the difference in temperature between the jet and the central recirculation zone.

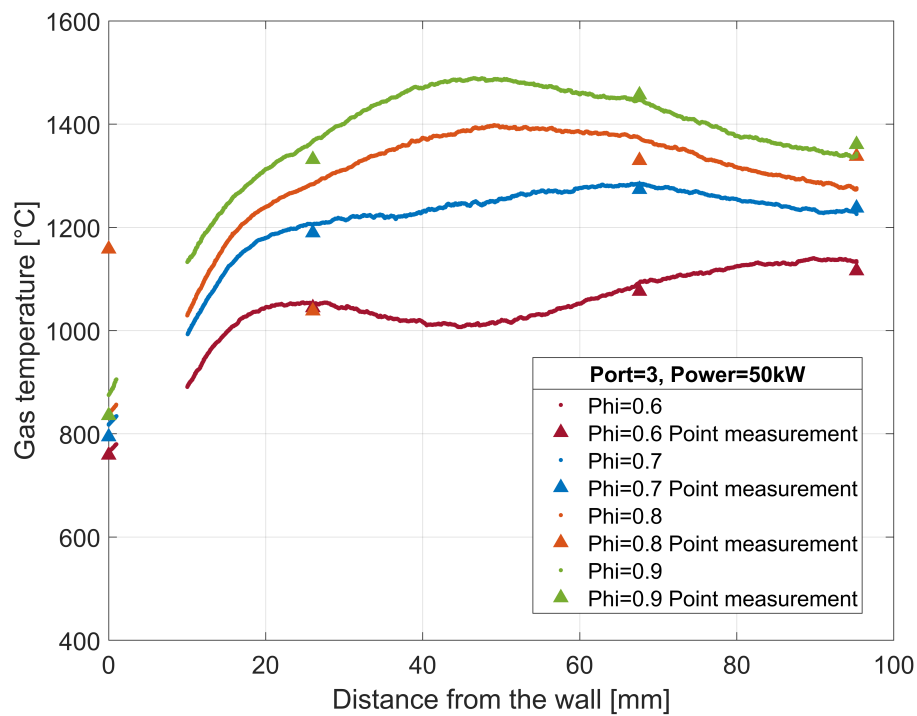


Figure 5.10: Radial profiles of temperature at 50kW for different equivalence ratios. Both the slow traverse measurements and the point wise measurements are shown at port 3

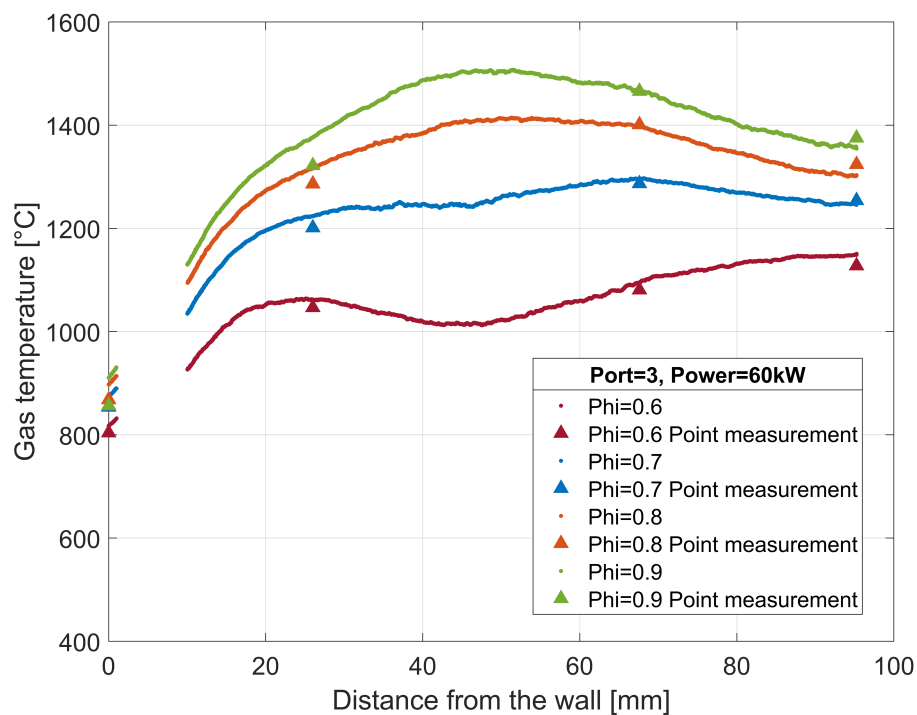


Figure 5.11: Radial profiles of temperature at 60kW for different equivalence ratios. Both the slow traverse measurements and the point wise measurements are shown at port 3

6

Emission Measurements

Emission measurements are performed inside the combustion chamber. This experimental campaign is aimed at obtaining a more practical indication of the combustion regime. The level of CO emissions indicates whether complete combustion occurs and the NO_x levels indicate whether or not flameless or ultra-low emission combustion occurs. For the current research the following emissions are measured; NO, NO_2 , CO, CO_2 , O_2 , and CH_4 .

6.1. Theoretical Background

Most often, gas concentration sensing techniques are based on the interaction of light with gas molecules. The advantage of this type of measurement technique is the short response time and high sensitivity to small concentrations. Many important molecules have characteristics of absorptivity lines in the mid-infrared (MIR) spectral region, see figure 6.1. The spatial differentiation in absorptivity within the MIR allows for the detection of several different molecules within the gas sample. Although the absorption wavelength is different for individual components, they may partially overlap and result in cross-sensitivities between different components.

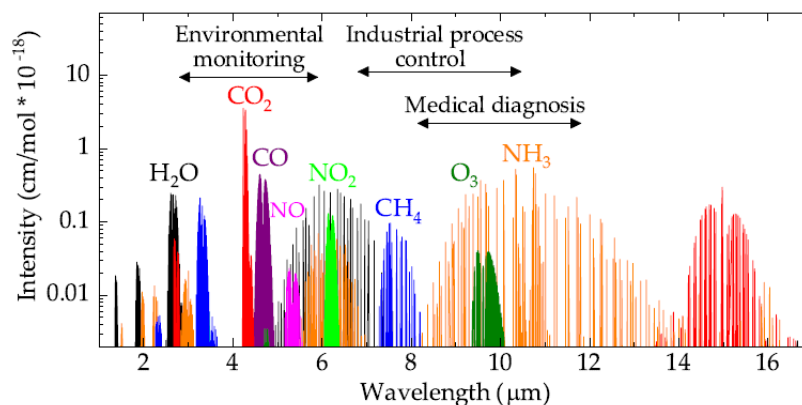


Figure 6.1: Mid-infrared absorption for different molecules with their respective intensity. [55]

6.1.1. Infrared analyser

A commonly used technique to measure CO, CO_2 , and CH_4 species concentration, is to measure the difference in infrared absorption, in the $\lambda = 2.5$ to $8 \mu\text{m}$ wavelength range, between a sample gas and a reference gas. The used Uras26 analyser uses a Non-Dispersive Infrared (NDIR) photometer suitable for continuous on-line gas analysis. The non-dispersive component relates to the fact that no dispersive element is used in the analyser to filter out the narrow spectrum suitable for the target gas measurements, unfiltered light will thus interact with the gas. The light source is an infrared broadband lamp, that directs the IR light in parallel through a gas sample chamber and a reference chamber. A schematic overview of the basic working principle

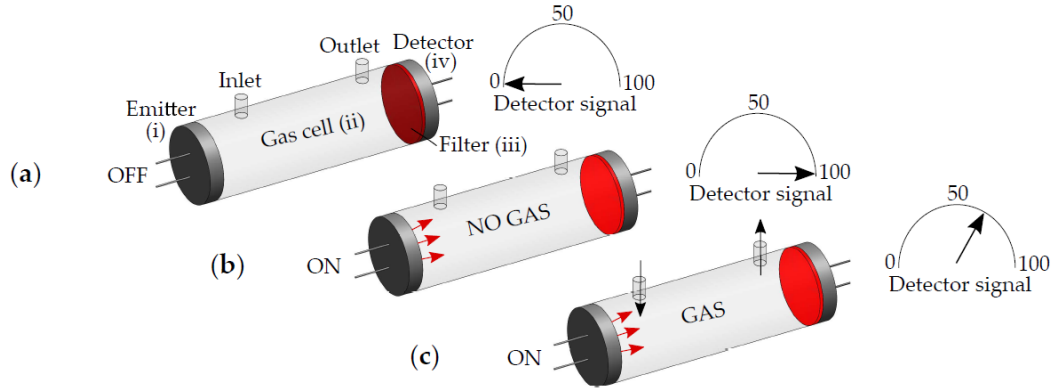


Figure 6.2: Optical gas sensor based on the Beer-Lambert's law, with (a) no signal detected when the IR lamp is off, (b) a maximum detected signal with the lamp on and no sample gas present, and (c) decreasing signal strength for an increase in gas concentration. [55]

of an optical gas sensor is shown in figure 6.2. In case of the Uras26, the emitter is an IR lamp and the gas cell represents the gas sample chamber. The detector is an opto-pneumatic detector that is filled with the gas that corresponds to the desired measuring component. This detector transforms the optical signal into a pneumatic signal.

Energy is removed from the light beam due to the absorption within a certain wavelength range depending on the gas concentration according to the Beer-Lambert law, equation 6.1.

$$I(\lambda) = I_0(\lambda)e^{-\alpha(\lambda)cl} \quad (6.1)$$

With $I(\lambda)$ the detected signal based on the emitted signal I , $\alpha(\lambda)$ the gas absorption coefficient, c the gas concentration, and l the light-gas interaction path-length, in this case, the sampling cell length. The light is subsequently filtered to eliminate all frequencies except the wavelength the selected gas molecules can absorb. The remaining energy of the beam is absorbed by the target selected component in the opto-pneumatic detector and causes a change in temperature and pressure within the detector. This induces an electrical signal via the membrane capacitor. The correlation between the sample and detector gas provides optimum sensitivity and high selectivity over the other components present in the gas sample. This also results in low detection limits for the desired measuring component. From equation 6.1 it can be deduced that the sample cell length, the light-gas interaction path-length l , determines the provable concentrations, which can range from only a few ppm (ppm < 10⁻⁴% Vol.) by volume to 100% Vol.

6.1.2. Ultraviolet analyser

The NO and NO₂ measurements are based on the sample component-specific emission absorption in the ultraviolet (UV) spectrum range $\lambda = 200$ to 600 nm. The Limas21 HW used for this purpose is a photometer for the simultaneous measurement of nitrogen compounds in hot and wet sulfur-free flue gas. The NO_x is measured on a hot and wet basis, to achieve accurate low concentration measurements. NO₂ decomposes to form HNO₂ and HNO₃ according to the reaction in 6.2, when reacting with condensed water that may be present in the sampling line when cooling the gas sample.



Where NO₂ is highly soluble in water, NO on the other hand is less soluble. The solubility of NO in water is 7% at 0°C and 0% at 100°C. It is therefore important to retain a high sample gas temperature and prevent condensation from occurring before the sample gas is put through the NO_x analyser. A schematic overview of the ABB Limas analyser is shown in figure 6.3. The Electrodeless Discharge Lamp (EDL) is the source that produces the UV beam. The EDL is filled with a mixture of N₂ and O₂ at reduced pressure. In the specific case of NO measurements, a high-frequency induction excites the NO molecules in the EDL, which will emit specific lines as they fall back to their initial state. NO-specific spectrum lines are emitted in the 200-290 nm range and N₂-specific spectrum lines in the 290-500 nm range, with the NO₂ component also identifiable in the latter range. Two main groups of NO/NO₂-specific lines are identified.

1. Cold emission lines: These lines are absorbed according to the Lambert-Beer Law (equation 6.1) by the identifiable component in the sample cell. This is the measurement beam.

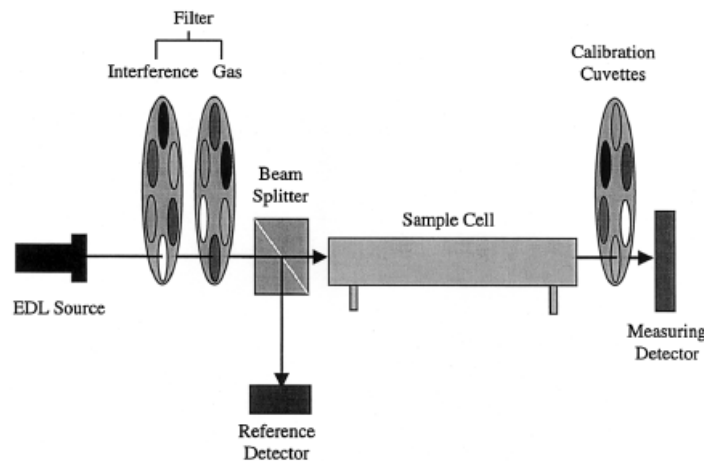


Figure 6.3: Schematic of the ABB Limas differential UV analyser [56]

2. Hot emission lines: These lines are not absorbed in the sample cell and reach the detector unchanged. This is the reference beam.

A narrow band interference filter installed on the first filter wheel will only allow the passage of the NO/NO₂ band spectral range being investigated. The second filter wheel houses a selectivity cell that contains 100% NO. This filter has to separate the hot from the cold lines, where the NO in the selectivity cell will absorb all the cold lines. To create a measurement and reference phase, the selectivity cell will alternately appear in the beam path. During measurement, the complete emission spectrum will reach the sample cell, where the appropriate wavelengths will be absorbed by the measurable components in the gas sample. During the reference phase, only the non-absorbable hot lines will reach the sample cell. A beam splitter is located between the filters and the sample cell. This consists of a partially transmissive mirror which will split the beam into two different beams. One will proceed through the sample cell up to the measuring detector, while the other will be directed towards the reference detector. Each measured component is thus assigned a measurement and reference phase, with 2 different intensities values in both phases. These four intensity measurements are used to determine the component concentration in the sample cell. This allows for a highly sensitive and selective measurement, accurately at very low concentrations.

6.1.3. Paramagnetic analyser

To determine the concentration of oxygen in the mixture, the Magnos28, a paramagnetic analyser is used. The working principle of this type of measurement is based on the magnetic susceptibility of oxygen with two unpaired electrons. The gas can be attracted into a strong magnetic field. Historically, this analyser is of the dumbbell type, the analyser incorporates two nitrogen-filled glass spheres mounted on a suspension. When the measured gas containing oxygen is introduced into this magnetic field, the oxygen molecules will tend to move towards the stronger side of the magnetic field, pushing the dumbbell aside. This will cause the dumbbell to rotate and twist the suspension. The twist in the suspension is measured by a reflective mirror attached to it that is exposed by a light source. The reflected light will move and this movement is captured by a photo-sensor. This information is fed back to a rotating mechanism around the dumbbell assembly which will apply a current to restore it to the 'zero' position. The applied current is proportional to the concentration of oxygen in the measured gas sample. This type of analyser provides stable measurements, without cross-sensitivities with other components, because only the oxygen component within the sample is paramagnetic. In the latest version of the Magnos28 analyser, the glass dumbbell has been replaced by a new silicon sensor, the microwing®, which operates on the same principle, but integrates all functionalities of the dumbbell in a single piece. This type of analyser is highly sensitive to shocks and vibrations. These should thus be minimised during the operation of the system.

The working principle of the oxygen sensor is shown in figure 6.4. This schematic differs slightly from the currently used system as the dumbbell and mirror assembly are replaced by a silicon sensor, however, the working principle is still the same.

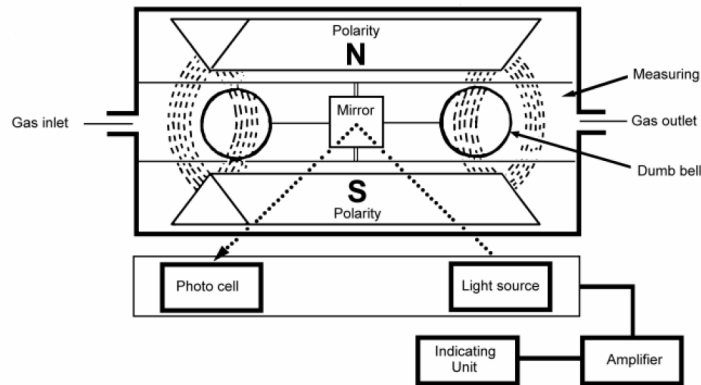


Figure 6.4: Schematic overview of the operating principle of a paramagnetic oxygen sensor [57]

Species	Range	Accuracy
NO/NO ₂	0 ... 3 ppm	0.1 ppm
CO ₂	0 ... 75 Vol%	0.1 Vol%
CO	0 ... 1000 ppm	1-10 ppm
O ₂	0 ... 21 Vol%	0.1 Vol%
CH ₄	0 ... 5 Vol%	0.01 Vol%

Table 6.1: Gas species with requested measuring range and accuracy

6.2. Acquisition New System

For the acquisition of the new gas analyser system, proposals and quotations were received from three different companies.

1. ABB Ltd
2. Siemens AG
3. Servomex b.v.

6.2.1. Evaluation Procedure

A thorough evaluation procedure is followed for the selection of the new gas analyser system. Meetings were held with representatives from the three above-mentioned companies. Following these meetings and discussions, proposals were received from all three potential suppliers. The different proposals were compared based on the following points:

1. Mission Suitability
 - (a) Ability to accurately measure all species within the required ranges with the required accuracy, with a special focus on the strict requirements regarding the NO and NO₂ species.
 - (b) Ability to use different fuels in the combustion process.
 - (c) Ability to measure within or close to the reaction zone.
 - (d) Ease of instalment in the lab.
2. Cost

The measured species, with their required ranges and accuracies, are given in table 6.1.

After a round of design iterations, the proposal by ABB Ltd showed the highest score on Mission Suitability and Cost. Their proposal has thus been chosen for the new gas analyser system to be acquired.

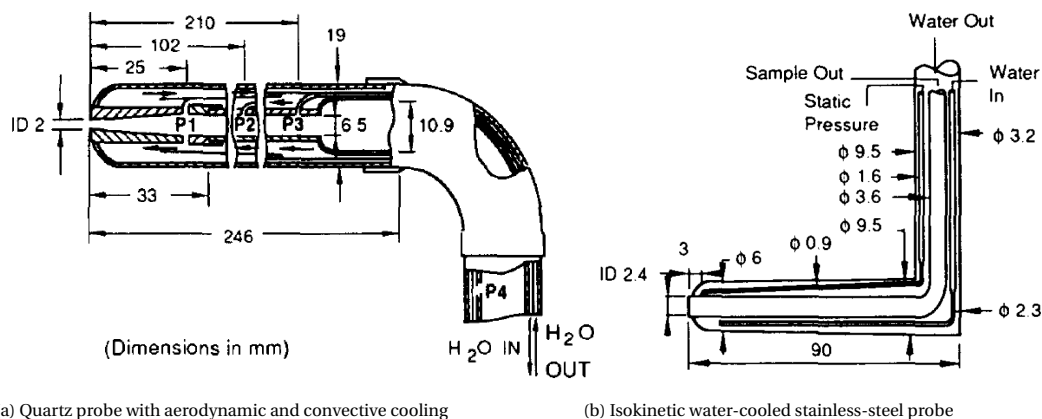
6.3. Probe Design

Although laser diagnostics have significant benefits over intrusive methods such as probe measurements for measuring species concentrations and temperature in combustion environments, they are more expensive and difficult to implement. Moreover, the use of a physical probe is important in the validation of models of practical systems. Therefore, the use of measurement probes is still common practice in the industry and in academia for measuring mean scalar quantities.

To measure the gas composition at different locations within the combustor, a new probe had to be designed. One that could withstand the high temperatures within the combustor, and also quickly quench the reactions of the extruded gas, effectively 'freezing' the gas composition at the measurement point. In addition, the probe-induced flow disturbances, an issue that becomes more critical in turbulent recirculating flows, should be kept to a minimum [53]. The probe used to extract the hot gasses from the combustion chamber has been specifically designed for the current setup and operating requirements.

Most probe designs available in the literature are either based on convective cooling or aerodynamic quenching techniques. Of the convection-cooling type probes, water-quenched and air-quenched designs are most commonly applied. These kinds of probes operate on the principle of quickly quenching the gas due to indirect contact with the cooling fluid, for reference see 6.5b. The sample gas and cooling fluid remain separated by a thin wall at all times, to reduce the system complexity. Some probes available in the industry mix the sample gas with the cooling water to enhance cooling. These direct cooling probes, however, require additional components downstream to separate both streams. The aerodynamically quenched probe operates on the principle of rapid expansion of the sample gas at the tip of the probe, for reference see 6.5a. These types of probes provide an advantage in reducing the aerodynamic disturbances in the flow, however, this may also result in slow quenching rates.

Although a quick quenching rate is required to preserve the original gas composition, a high enough sample gas temperature should be maintained with regard to condensable vapours in the mixture. Condensation of water particles in the sample gas will reduce the concentration of the minor species NO and NO₂ that are soluble in water. Retaining a minimum temperature of 100-180°C at the probe exit will mitigate this problem. Due to these considerations, the choice has been made to design an indirect convection quenched probe, that will utilize air as a cooling fluid. It is decided a double-pass cooling arrangement is required. The coolant first flows in the opposite direction to the sample gas, along with the probe, quickly quenching the gas composition. At the tip, the flow turns in the opposite direction to flow along with the outer cooling shell and cool the outer wall of the sampling probe.



(a) Quartz probe with aerodynamic and convective cooling

(b) Isokinetic water-cooled stainless-steel probe

Figure 6.5: Examples of different types of cooled probe designs, from [53]

6.3.1. Thermal analysis

The first step in the process is the development of a thermal model to simulate the temperature evolution over the length of the probe. Based on the coolant layout, three different flow directions are identified; the gas sampling flow and two cooling flow in opposite directions. These three flow paths are highlighted in fig-

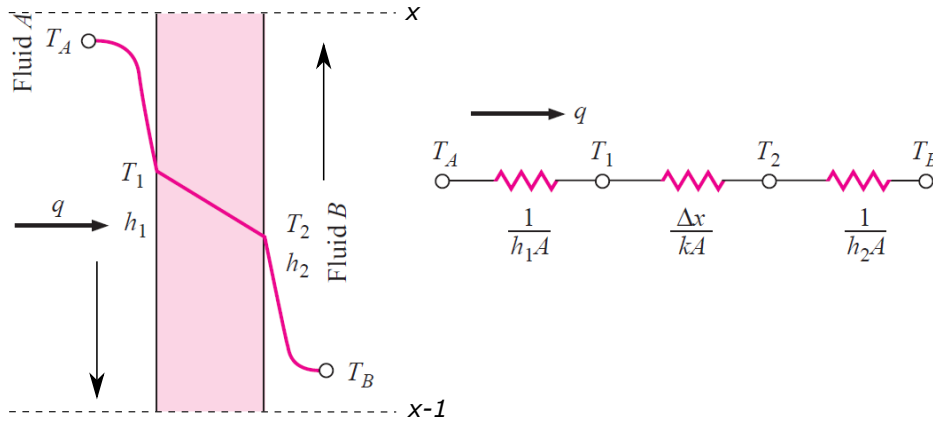


Figure 6.6: Overall heat transfer through a plane wall [58]

ure 6.9.

Overall heat transfer coefficients

Heat transfer between the different flow paths is simplified to a general problem of a heat flow across a plane wall from a hot to a cold fluid. This simplified problem is visualised in figure 6.6. The figure also displays the heat transfer process represented by a resistance network. Fluid A represents the hot fluid and Fluid B represents the cold fluid.

The overall heat transfer by combined convection and conduction is often expressed in terms of the overall heat transfer coefficient U . This relation is given by

$$q = UA\Delta T_{A-B} \quad (6.3)$$

With A the area over which the heat flow occurs, with the overall heat transfer coefficient U given by

$$U = \frac{1}{\frac{1}{h_1} + \frac{\Delta x}{k} + \frac{1}{h_2}} \quad (6.4)$$

For a system of multiple concentric cylinders, the area for convection will differ between the inside and outside of the cylinder in contact with the fluid. Combining equations 6.3 and 6.4, the overall heat transfer is expressed as

$$q = \frac{T_A - T_B}{\frac{1}{h_i 2\pi r_o} + \frac{\ln(r_o/r_i)}{2\pi k} + \frac{1}{h_o 2\pi r_i}} dL \quad (6.5)$$

for a cylinder section with length dL , where the subscripts i and o refer to the inside and outside of the cylinder.

When considering two fluids A and B, flowing in opposite directions, the total energy lost by flow A to flow B in terms of bulk temperature difference is given by

$$q = \dot{m}c_p(T_{b_{out}} - T_{b_{in}}) \quad (6.6)$$

where the heat capacity of the fluid is given by c_p and the fluid mass flow rate is given by \dot{m} . To show the temperature evolution over the length of the probe, it is subdivided into smaller volumes with differential lengths dL . As an example, the heat balance for a volume of fluid B is shown in equation 6.7. Again, referring to figure 6.6, heat is transferred from fluid A to B through the wall

$$\dot{m}c_p(T_{B_x} - T_{B_{x-1}}) = PU_{AB}dL(T_{A_{x-1}} - T_{B_{x-1}}) \quad (6.7)$$

where PU_{AB} is the perimeter of the cylindrical channel times the overall heat transfer coefficient. The subscripts x refer to discrete positions along the length of the probe. $x=1$ represents the inlet of the probe at the tip, whereas $x=0$ represents the location of the probe at the wall. The heat balance in equation 6.7 does not account for radiative heat transfer between the concentric tubes, this will have an indirect influence on the fluid temperature.

Convective heat transfer coefficients

The convective heat-transfer coefficients h_i and h_o from equation 6.5 are determined based on forced convection principles in pipe flows. For turbulent flows, the thermal entry length is short and hence the flow is assumed to be hydrodynamically and thermally fully developed, the shape of the velocity and temperature profiles are constant. The deviation of the mean Nusselt number from the locally calculated values, in this case, is less than 5% for pipes with a length of $L/D > 12$ [58]. The thermal entry length for laminar flow is much longer than for the turbulent flow [58]. For the laminar flow cases, correlations based on thermally and hydrodynamically developing flows are used, correlation 6.15, which is valid for all lengths of pipes. Because the heat transfer process is a function of the flow velocity, it is thus dependent on the pipe Reynolds number. In the case of a channel with concentric tubes, the Reynolds number is defined as

$$Re_D = \frac{uD_H}{\nu} \quad (6.8)$$

with the hydraulic diameter D_H defined by

$$D_H = \frac{4A}{P} \quad (6.9)$$

where A is the flow cross-section and P is the wetted perimeter. A pipe flow is considered laminar if the Reynolds number is less than $Re < 2300$ and the flow is considered fully turbulent at $Re > 10^4$. The transitional region is considered in the range $2300 < Re < 10^4$. The ratio of momentum diffusivity to thermal diffusivity is given by the Prandtl number, defined as

$$Pr = \frac{\nu}{\alpha} \quad (6.10)$$

this is an important parameter in the heat transfer process. To calculate the convective heat transfer coefficients, first, the Nusselt number Nu has to be known. This is the ratio of convective to conductive heat transfer at a fluid boundary. Correlations for Nu are experimentally determined based on large sets of experimental data. The mean Nusselt number is given by

$$\overline{Nu} = \frac{\bar{h}L}{k} \quad (6.11)$$

For forced convection through a channel, the following correlations for Nu are used. In case of hydrodynamic and thermal development of laminar flow $Re \leq 2300$, the correlations obtained at constant wall temperature are used.

$$Nu_{m,T,1} = 3.66 \quad (6.12)$$

$$Nu_{m,T,2} = 1.615 \sqrt[3]{RePrd_i/l} \quad (6.13)$$

$$Nu_{m,T,3} = \left(\frac{2}{1 + 22Pr} \right)^{1/6} (RePrd_i/l)^{1/2} \quad (6.14)$$

$$Nu_{m,T} = \left\{ Nu_{m,T,1}^3 + 0.7^3 + [Nu_{m,T,2} - 0.7]^3 + Nu_{m,T,3}^3 \right\}^{1/3} \quad (6.15)$$

In case of a fully developed turbulent flow $Re > 10^4$

$$Nu_m = \frac{(\xi/8)RePr}{1 + 12.7\sqrt{\xi/8}(Pr^{2/3} - 1)} \left[1 + (d_i/l)^{2/3} \right] \quad (6.16)$$

where

$$\xi = (1.8 \log_{10} Re - 1.5)^{-2} \quad (6.17)$$

This equation is put forward by Gnielinski [59] and taken from [60]. When considering the transitional region between laminar and fully developed turbulent flow $2300 < Re < 10^4$ the development of turbulence in the fluid depends on many different factors. To overcome this issue, Gnielinski proposed to interpolate between fully laminar and turbulent flow in this regime, according to equation 6.18.

$$Nu = (1 - \gamma)Nu_{lam,2300} + \gamma Nu_{turb,10^4} \quad (6.18)$$

where γ is given by

$$\gamma = \frac{Re - 2300}{10^4 - 2300} \quad (6.19)$$

$Nu_{lam,2300}$ is the Nusselt number at $Re=2300$ calculated from equation 6.15. $Nu_{turb,10^4}$ is the Nusselt number at $Re=10^4$ calculated from equation 6.16. By applying an interpolation, a jump in Nusselt number at the boundary of $Re=2300$ is avoided. The foregoing correlations have been taken from the VDI Heat Atlas [60].

Solution procedure

The fluid flowing through an annulus is subjected to a heat flux over both lateral areas. The flow through the outer cooling channel gains heat from the surrounding flue gas and the flow through the inner cooling channel. The flow through the inner cooling channel gains heat from the sample gas flow. The temperature gradient over these three flow paths is obtained by solving the heat balance for all volumes simultaneously. A linear system of equations is set up as seen in equation 6.20. The same system of equations in matrix form $A\mathbf{x}=\mathbf{b}$ is shown in 6.21, where A is the coefficient matrix, containing the overall heat transfer coefficients PU and thermal masses of the system $\dot{m}c_p$. With \mathbf{x} the vector containing the temperatures along all three flow paths, T_1 to T_{3N} . Vector \mathbf{b} resembles the right side of equation 6.20, containing any other sources of heat gain. To calculate the temperature gradients along the different flow paths, the system is solved for the vector \mathbf{x} . For the current case of $N=1000$, matrix A is of the size $3N \times 3N$, with both vectors having a length of $3N$. Because all three flow paths have to be solved simultaneously, they have to be combined in the same system. The vector \mathbf{x} is defined as $\mathbf{x} = [T_{c,in_1}, \dots, T_{c,in_N}, T_{c,out_{N+1}}, \dots, T_{c,out_{2N}}, T_{g_{2N+1}}, \dots, T_{g_{3N}}]^T$, with T_{c,in_j} the inner cooling flow temperature, T_{c,out_j} the outer cooling flow temperature, and T_{g_j} the sample gas flow temperature. The radiative heat transfer is evaluated separately after solving the system of equations, because of the non-linear dependence on temperature, and is added to the heat balance afterwards. The system is thus solved iteratively to obtain a converged solution. The convergence is tracked by evaluating the difference in temperature at the coolant exit between iterations. Temperature-dependent flow properties such as μ , ρ and k are re-evaluated with every iteration.

$$\sum_{i=j}^{3N} a_{ij} T_j = \sum q_i \quad (6.20)$$

$$A_{3N \times 3N} = \begin{bmatrix} a_{1,1} & a_{1,2} & \cdots & a_{1,3N} \\ a_{2,1} & a_{2,2} & \cdots & a_{2,3N} \\ \vdots & \vdots & \ddots & \vdots \\ a_{3N,1} & a_{3N,2} & \cdots & a_{3N,3N} \end{bmatrix} \begin{bmatrix} T_1 \\ T_2 \\ \cdots \\ T_{3N} \end{bmatrix} = \begin{bmatrix} \sum q_1 \\ \sum q_2 \\ \cdots \\ \sum q_{3N} \end{bmatrix} \quad (6.21)$$

6.3.2. Aerodynamic analysis

The probe design that followed from the thermal analysis, consists of 3 concentric cylinders of which 2 are used for the cooling in a counter flow configuration. This results in a thick probe, with an outer diameter of 12mm. Under certain critical flow conditions, this can cause vortex shedding in the wake of the probe. The Reynolds number of the flow over the probe varies between $Re \approx 300-4000$. According to an experimental investigation by J. Lienhard [61], this will result in a fully turbulent vortex street in the wake of the cylinder, see figure 6.7. This vortex shedding in the wake of a bluff body occurs with a certain frequency f_v . The vortex shedding frequency is related to the flow velocity via the dimensionless Strouhal number St , given as

$$St = \frac{f_v L}{U} \quad (6.22)$$

where L is the characteristic length, in this case, the probe diameter and U the free stream flow velocity. If the frequency of vortex shedding overlaps with the natural frequency of the probe, this will incite significant vibrations which may damage the probe. To estimate the vortex shedding frequency, first St is estimated from figure 6.8. In the Reynolds number range of 300-4000, the red hatched region, $St \approx 0.21$. With U in the range of 10-120 m/s, this results in $f_v \approx 175-2100$ Hz.

The relation between the Strouhal number and drag coefficient is also noted by Lienhard [61], where c_d is essentially constant, around $c_d \approx 1$ in the region of constant St . With c_d known, the drag force on the probe is calculated according to

$$F_d = \frac{c_d \rho U^2 A}{2} \quad (6.23)$$

with U and ρ the local flow conditions, and A the reference area perpendicular to the flow, assuming the probe to be fully inserted up to the combustor centerline. The drag force exerted on the probe is calculated to be in the range of $F_d \approx 0.01-1.67$ N. With the assumption of the probe resembling a single circular cylinder the displacement of the probe tip under a distributed load is calculated to be less than 0.01mm, negligibly small.

Mode	K_n	Nodal position/l					f_n
1	3.52	0.0					10
2	22.0	0.0	0.783				64
3	61.7	0.0	0.504	0.868			180
4	121	0.0	0.358	0.644	0.905		352
5	200	0.0	0.279	0.500	0.723	0.926	582

Table 6.2: Natural frequencies of vibration for a cantilever beam [62]

The natural frequency of a structure is the frequency at which the structure tends to vibrate in the absence of a damping force. The probe natural frequency is calculated assuming the system can be represented by a cantilever beam under distributed loading, according to equation 6.24 taken from Young and Budynas [62].

$$f_n = \frac{K_n}{2\pi} \sqrt{\frac{EIg}{wl^4}} \quad (6.24)$$

With the constant K_n different for n modes of vibration, E the Young's modulus, I the area moment of inertia, w the beam width or in this case probe diameter, and l the probe length. The values for K_n are given in table 6.2. Per mode of vibration, the respective node positions normalised by the probe length, and the calculated resonance frequency are shown. The values for f_n range between 10-582Hz. The resonance frequencies partly overlap with the range of vortex shedding frequencies in the wake of the probe. Straight fins have been added to the outside of the probe, to alter the flow field and suppress the vortex shedding. M. Zdravkovich proposed different concepts for the suppression of vortex shedding in the wake of circular cylinders [63]. Out of the different concepts investigated by Zdravkovich, the option with 4 straight fins has been chosen (concept 7 appendix D), as it has a positive effect on the suppression of vortex shedding and it is relatively simple to manufacture.

Layout Probe

A schematic of the designed probe is seen in figure 6.9. The red lines highlight the gas sampling path. The gas sample is extracted at the tip and travels down the probe's central tube to the probe outlet at the bottom. At this point, the gas sample temperature is measured by thermocouple TC11. The blue arrow represents the coolant flow entering the probe. The blue lines represent the first pass of the coolant through the inner cooling channel. At the probe's tip, the coolant reverses direction and flows back along the outer cooling channel represented by the orange lines. The exit of the coolant is represented by the orange arrow pointing out of the page. The coolant inlet and exit temperatures are measured by thermocouples TC6 and TC9, respectively. The gas sampling probe is shown relative to the wall of the combustor for the case of it being fully inserted into the combustor. A larger version of the probe schematic is shown in appendix E

6.4. Setup

6.4.1. Steel combustion chamber

A schematic overview of the steel combustion chamber with the probe entry ports is shown in figure 6.10. Ports 3 and 6, used for the current experimental campaign are highlighted in red.

6.4.2. Gas analyser system components

A drawing of the complete gas analysis system is provided in figure 6.11. The sample gas flow path is highlighted in red. The gas is first extracted from the combustion chamber by the probe. In the drawing this is not specified, only the interface with the analyser cabinet is shown as 'By Customer'. The extracted gas first arrives at the Limas21 HW analyser. Afterwards, the gas flows through the cooler unit, to extract water vapour from the sample before passing through the pump, Uras26, and Magnos28 modules respectively. After passing through all analyser modules, the gas is released to the environment. An overview of the different system components is given in table 6.3

Component	Details
Heated sample line	<ul style="list-style-type: none"> • length=3m • self-regulated heating strip 30W/m • Temperature=180°C
Cooler unit SCC-C	<ul style="list-style-type: none"> • 2 Gas paths • Temperature=3°C • Condensate drain
Pump unit SCC-F	<ul style="list-style-type: none"> • Diaphragm pump • Flow range: 20..120 l/h
Limas21 HW analyser	Based on UV absorption spectroscopy principle 1) Measured component: NO Measuring range: 0...10ppm 2) Measured component: NO ₂ Measuring range: 0...10ppm
Uras26 analyser	Based on IR absorption spectroscopy principle 1) Measured component: CO ₂ Measuring range: 0...75%vol 2) Measured component: CO Measuring range: 0...1000ppm 2) Measured component: CH ₄ Measuring range: 0...50.000ppm
Magnos 28 Oxygen analyser	Based on paramagnetic principle Measured component: O ₂ Measuring range: 0...25%vol
Rittal cabinet	<ul style="list-style-type: none"> • Houses the above mentioned components • Freely movable (placed on wheels)

Table 6.3: Overview of the ABB AO2000 extractive gas analyser system customized for the current research

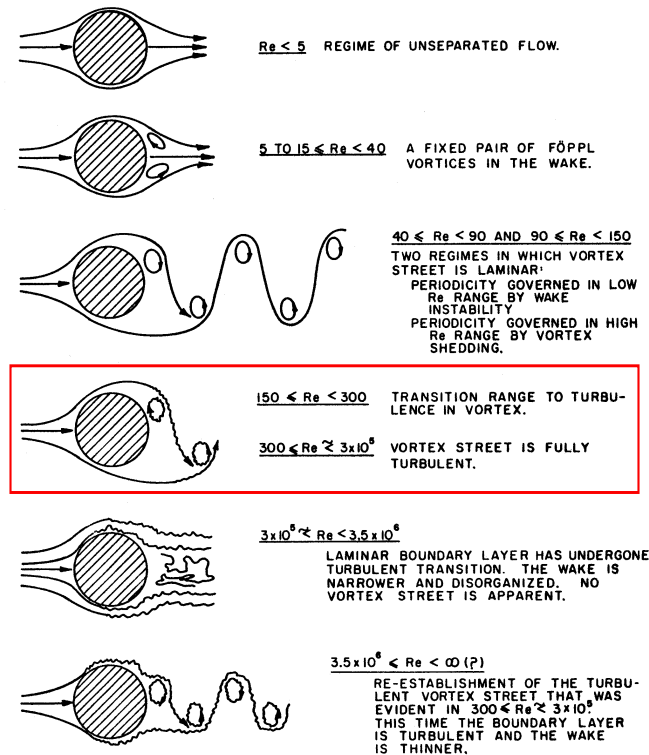


Figure 6.7: Regimes of fluid flow across circular cylinders [61]

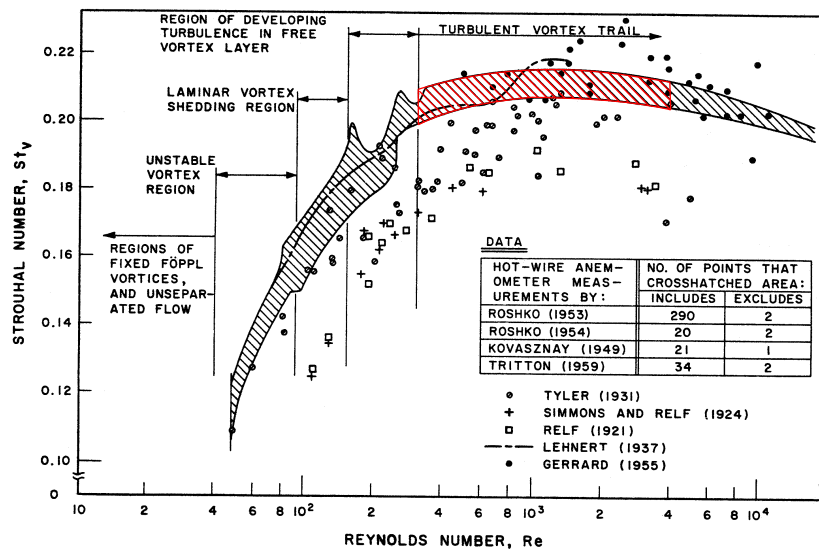


Figure 6.8: Strouhal-Reynolds number plot for circular cylinders [61]

6.5. Methodology

6.5.1. Thermal model validation

The thermal model used to design the cooled probe is validated based on a range of operating conditions. For a specific operating condition, the probe is traversed inwards towards the centre of the combustor. Per radial position, the average temperature at the coolant inlet, coolant outlet, and probe outlet is calculated over a set of 2000 samples. A schematic of the probe, including the thermocouples is shown in figure 6.9. The calculation procedure as described in section 6.3.1 is reversed to calculate the gas temperature within

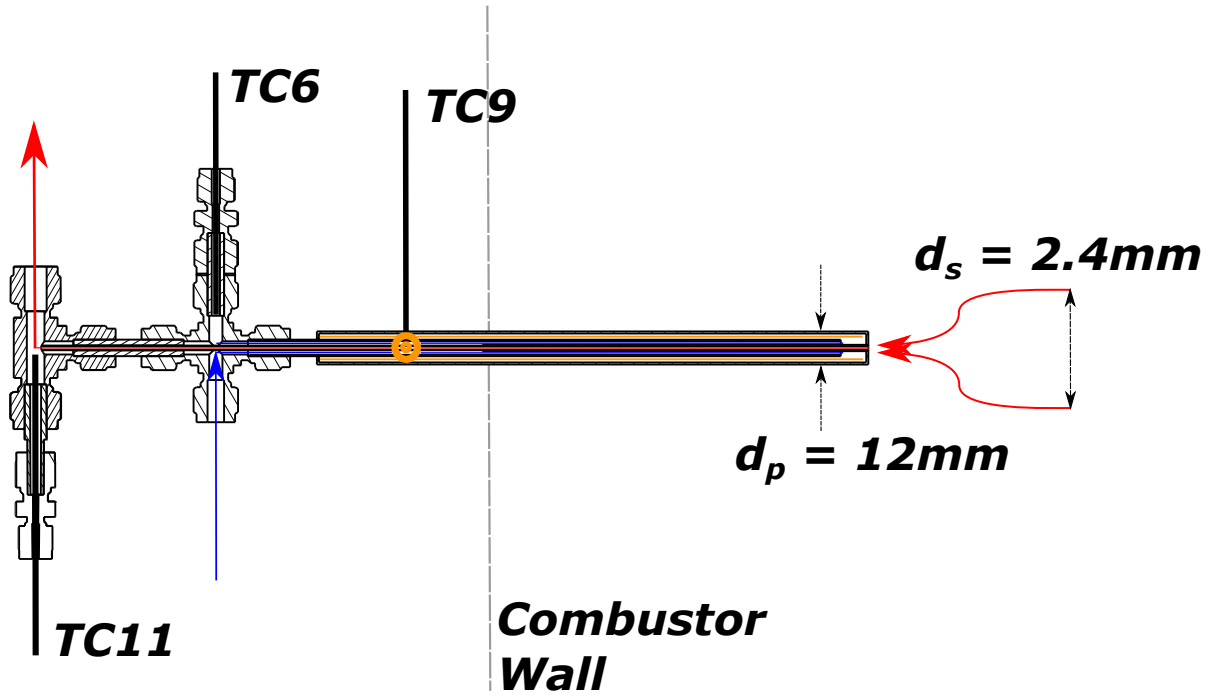


Figure 6.9: Schematic of the cooled gas sampling probe

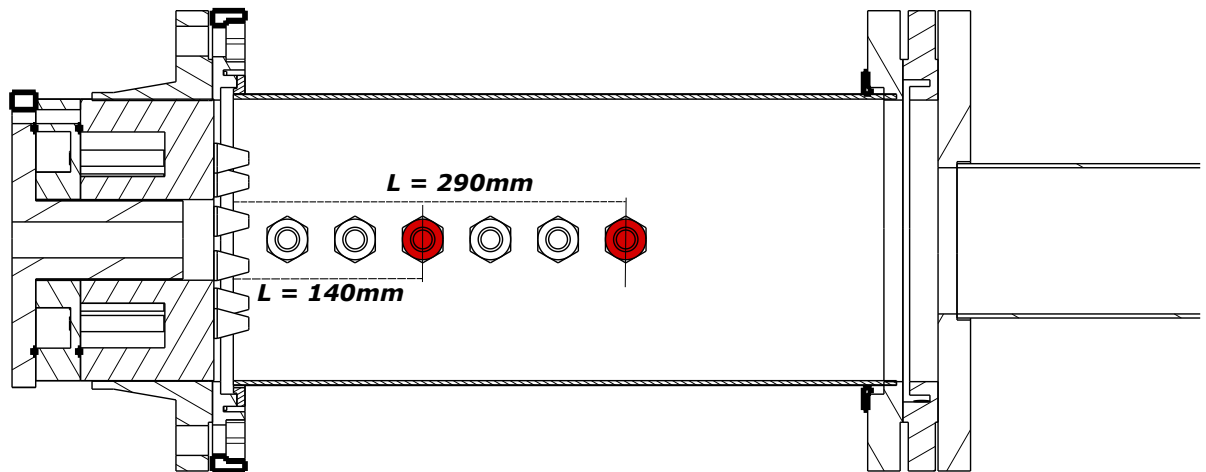


Figure 6.10: Schematic overview of the combustor including burner head, with ports 3 and 6 marked in red

the combustor. Instead of specifying a gas temperature, and calculating the coolant exit and probe outlet temperatures, the probe outlet temperature is given as an input. Based on this input the gas sample inlet and coolant exit temperatures are calculated. The results are presented in figures 6.13(a-b).

These figures show the gas temperature and coolant exit temperature to be greatly underpredicted. Figure 6.13a shows the calculated gas temperatures and the platinum thermocouple measurements at the same locations. The calculated coolant exit temperature compared to the measured coolant exit temperature is shown in figure 6.13b. The large differences between the measured and calculated values are attributed to the fact that external cooling is not modelled. The thermal model focuses primarily on the heat transfer mechanisms within the combustor. However, with every design iteration, the external section of the probe increased in size and complexity. This external section is not implemented in the thermal model due to its complex shape and combined effect of both natural and forced convection outside the combustor. Consequently, the gas sample is cooled more effectively than estimated from the thermal model. When the measured sample gas exit temperature is used in the reverse calculation, the calculated gas inlet temperature and coolant exit temperature are shown to be substantially under-predicted, see figures 6.13(a-b).

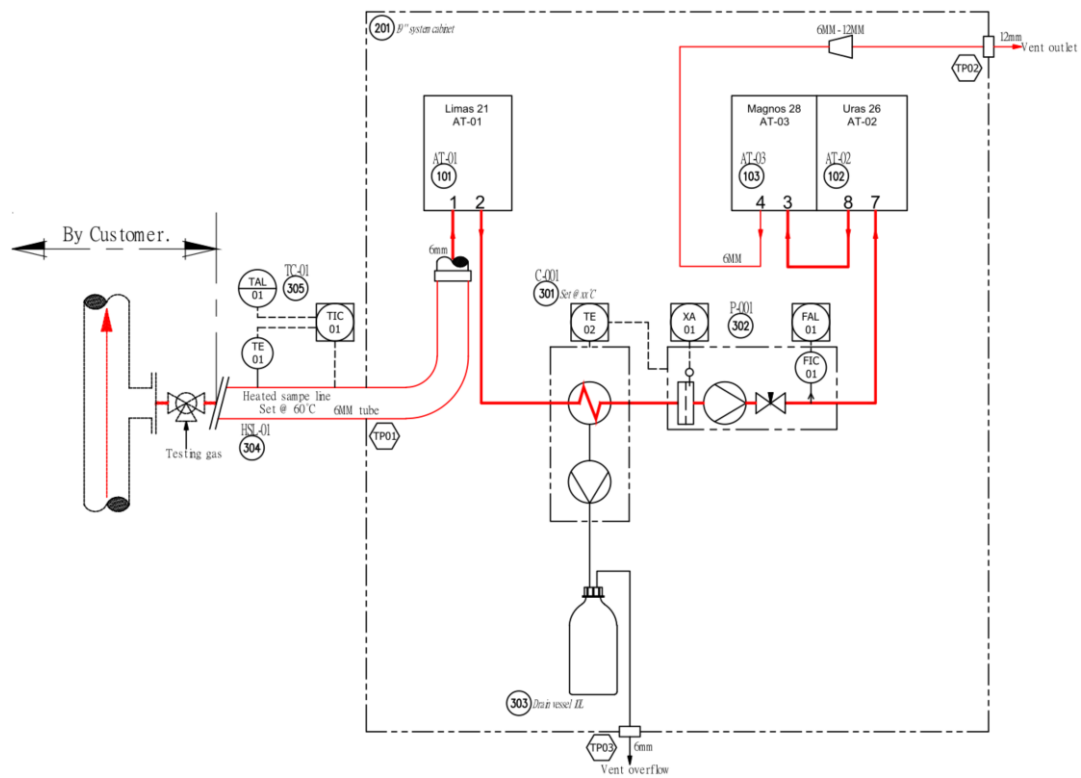


Figure 6.11: Drawing of the gas analyser system at the lab

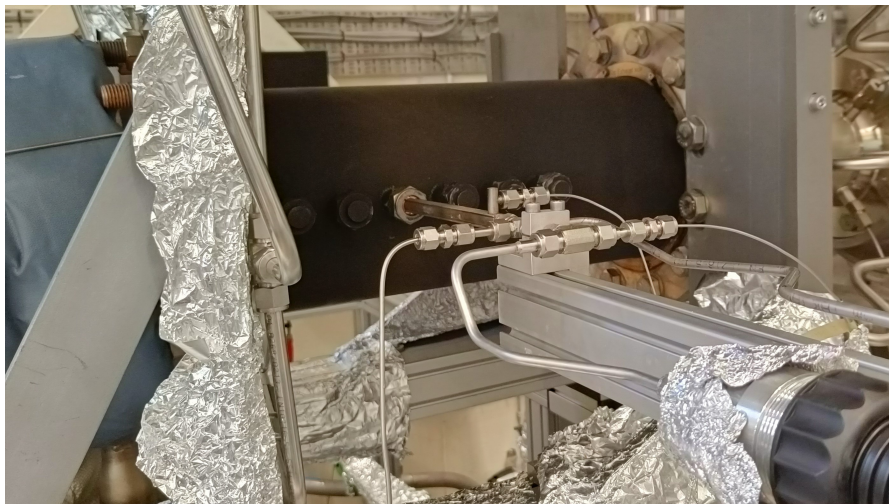
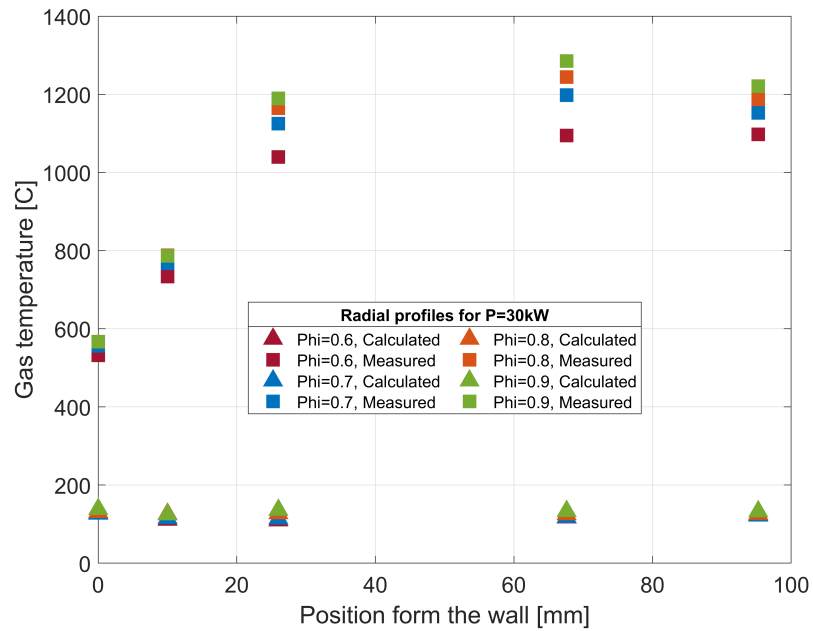
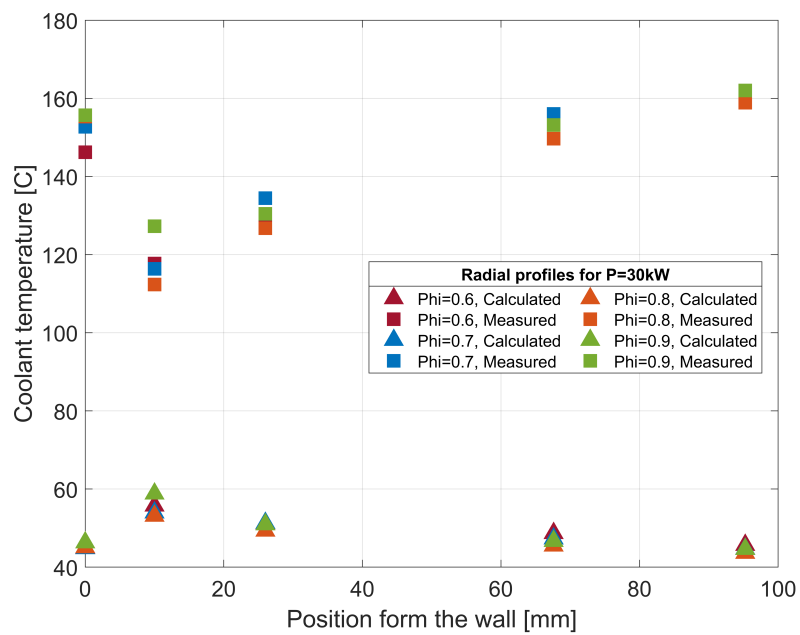


Figure 6.12: Photo of the gas analyser probe inserted in the combustion chamber



(a) Gas temperature comparison of experimental and calculated results



(b) Coolant temperature comparison of experimental and calculated results

Figure 6.13: Gas probe thermal model validation

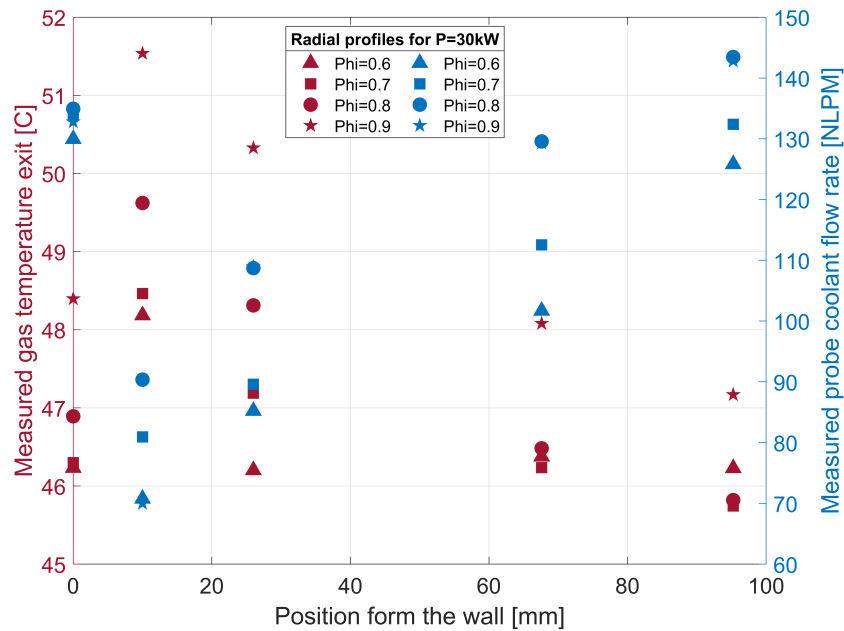


Figure 6.14: Combined plot with gas temperature and coolant flow rate vs radial position in the combustor

Bottle	Mixture species	Requested Concentration	Certified Concentration	Certification accuracy
1	CO/CH ₄ /N ₂	800 ppm/4.00 vol%/Balance	801 ppm/3.99 vol%/Balance	1%
2	NO/N ₂	8 ppm/Balance	8.46 ppm/Balance	1%
3	NO ₂ /N ₂	8 ppm/Balance	8.1 ppm/Balance	2%
4	CO ₂ /N ₂	60 %vol/Balance	59.8 %vol/Balance	1%

Table 6.4: Overview of used calibration gas bottles

Figure 6.14 shows both the measured gas temperature and probe coolant flow rate for the same operating conditions. The plot shows the measured gas temperature at the outlet of the probe, to decrease with an increase in coolant flow rate.

6.5.2. Calibration procedure

Before any gas analysis is performed, the system has to be calibrated. For all measured components a span or 2-point calibration procedure is employed. This means the sensor's output is matched to a 'known' value at two points, the 'zero' point and the span. At the 'zero' point, none of the target gas is present in the mixture. At the span, a specified amount of target gas is present in the mixture. In case the measured value of the analyser does not match the 'known' value (either zero or span), the measured value is adjusted accordingly. Following this procedure, the system is considered calibrated.

For the span calibration, custom-mixed calibration gas bottles were ordered from a gas supplier. These bottles contain a mixture of nitrogen N₂ and a specified amount of the target gas, in this case, 80% of the measurement span. An overview of the calibration gas mixtures are tabulated in table 6.4. The mixture composition is determined in consultation with the gas supplier. During calibration, the cross-sensitivity and gas component correction is disabled [64]. Therefore, the calibration mixture should be free of any components that could cause cross-sensitivity. Because of this, the NO and NO₂ gasses are supplied in separate bottles. Table 6.4 displays the requested mixture concentration, the supplied certified concentration and the accuracy with which the certified concentration has been measured. The difference in requested concentration and certified concentration follows from the mixing accuracy by the gas supplier. The bottles are produced

Step	Gas component	Mixture species	Type calibration
1	NO ₂ /CO/CO ₂ /CH ₄	NO ₂ + N ₂	Span/Zero/Zero/Zero
2	CO ₂ /NO/NO ₂	CO ₂ + N ₂	Span/Zero/Zero
3	NO/NO ₂ /O ₂	NO + N ₂	Span/Zero/Zero
4	CO/CH ₄	CO + CH ₄ + N ₂	Span/Span
5	O ₂	Ambient air	Span

Table 6.5: Step-by-step calibration procedure

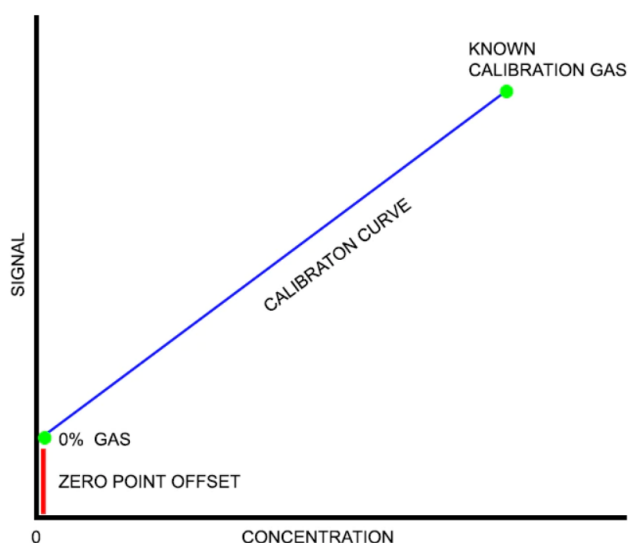


Figure 6.15: 2-Point calibration curve, schematic obtained from [65]

with a certain blend tolerance, the supplied mixture concentration lies within a range of ± 2 ppm or 5%, dependent on the gas mixture, of the requested concentration. The supplied mixture concentration is analysed and certified by the gas supplier with an accuracy of ± 1 or 2%. For an accurate zero calibration, a pure inert gas should be connected to the analyser that does not contain any traces of the target gas. Often pure nitrogen is used for this. In this case, the custom mixed bottles in table 6.4 are used. A step-by-step explanation of the calibration process is tabulated in table 6.5. The gas component which has been calibrated (either span or zero) is given in the 2nd column. This component is calibrated against the mixture as specified in the 3rd column. The 4th column presents the type of calibration per gas component respectively.

The NO₂/NO/CO₂/CO/CH₄ components are not zero calibrated in the open air, because the ambient air may still contain traces of these gasses or other species that may cause cross-sensitivities. O₂ is zero calibrated on the NO + N₂ bottle because the certificate specifically stated this bottle to contain no traces of O₂. The CO/CO₂/CH₄ have been zero calibrated on the NO₂+N₂ bottle. NO, and NO₂ are zero calibrated on the CO₂ bottle, while the NO₂ component is again zero calibrated on the NO bottle. The nitrogen dioxide component proved difficult to zero as the measured value is quite unstable and fluctuating. Getting more experienced with the system, it proved useful to zero the NO₂ component twice on different calibration bottles.

With the zero and 80% span point calibrated, a calibration curve is estimated by the analyser unit. This curve is assumed to be a linear relationship between the two points. With the calibration curve, the gas analyser unit calculates the correct gas concentration for every amount of target gas that it measures. A schematic of such a linear calibration curve, based on a zero and span point calibration is seen in figure 6.15. The difference between the sensor reading and the target gas concentration at the zero point is called the zero-point offset (the red line in figure 6.15). This value is stored in the analyser unit memory and is applied to all future sensor readings to correct the current measurement for the offset at the zero point.

6.5.3. Measurement procedure

Radial emission measurements have been performed at two axial distances of 290mm and 140mm from the face of the burner head. Normalised to the nozzle diameter this is $x/d_{noz} \approx 43.5$ and $x/d_{noz} \approx 21$. The locations of these ports are highlighted in red in figure 6.10. The first location is assumed to be outside the region of influence of the recirculation zone, the flue gas at this location flows towards the exhaust of the combustor. This location is considered to best resemble the gas composition at the exhaust. The second location is assumed to be near the reaction zone, the location where the jet impinges on the combustor wall. At this location, there should be a clear difference between the gas composition in the jet region and in the inner recirculation zone. The probe is traversed inwards from a location near the wall up to the centerline of the combustion chamber while measurements are taken at 5 discrete radial positions.

Before every experimental run, the gas analyser units are calibrated and the obtained values are saved to a 'pre-experiment' calibration file. The combustor is preheated by supplying heated air to the system. When the system reaches a minimum temperature threshold the pilot flame is started and afterwards the combustor is started. Once a steady-state condition has been achieved at the operating point to be investigated, the data acquisition is started.

The probe is traversed to the desired measurement point where the system waits for 30 seconds to adjust to the local conditions and reach a steady-state reading. Subsequently, the data acquisition is started. The T_{90} time, the time it takes to measure 90% of the actual concentration is an important parameter that determines the settling time before measurements can be taken. The T_{90} time for both the Limas21 HW and the Uras26 is $T_{90} \approx 15\text{sec}$, after which minimal output fluctuation is achieved. For the Magnos28 the $T_{90} \approx 3\text{sec}$. A settling time of 30sec is thus sufficient. For every radial position of the probe, the cooling requirement for the probe changes. Therefore, the coolant flow is adjusted accordingly during the experimental campaign to keep the probe wall temperatures within reasonable bounds.

Measurements are taken for 200 seconds per position. With an acquisition rate of 10Hz, this results in a sample size of 2000 samples per measurement. This sample size is sufficiently large for statistical analysis of the mean and standard deviation of the obtained results. When the measurements have finished at a certain condition, the probe is traversed back to its initial point near the combustor wall. The probe stays at this location while other measurements are taken and/or the operating point of the combustor is adjusted. The different operating points at which the gas composition measurements have been taken are given in table 3.2. When all measurements have been taken at a specific power setting, the combustor is shut down and cooled down. The gas analyser is connected to the calibration gas bottles to perform an 'after-experiment' calibration. The zero and span calibration are not saved in the modules themselves, however, the obtained values are saved to a file in the data acquisition system. The difference in the 'pre-experiment' and 'after-experiment' gas composition values is the drift during the experiment.

6.5.4. Data correction

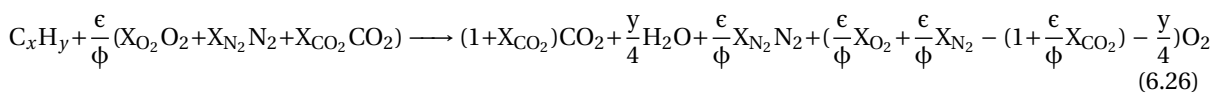
The raw gas composition data obtained from the measurements still have to be corrected, before they can be presented and discussed.

Water vapour correction

The NO and NO₂ measurements in the Limas21 HW analyser are based on a wet sample. To present the gas composition for comparison, it should be converted to a dry measurement, the presence of water vapour has to be corrected for, equation 6.25.

$$X_{dry} = X_{wet} * \left(\frac{100}{100 - X_{H_2O}} \right) \quad (6.25)$$

With X_{H_2O} the % water content of the measured gas by volume, X_{wet} the measured wet gas concentration, and X_{dry} the corrected dry gas concentration. Because X_{H_2O} is not measured with the current system, it is estimated from equilibrium calculations. This has been done for all cases investigated. The general form of the ideal combustion equation used for the equilibrium calculations is given in equation 6.26.



With $\epsilon = \frac{x+y/4}{X_{O_2}}$ and methane (CH₄) as fuel, resulting in $x=1$, and $y=4$. This procedure relies on the assumption of complete ideal combustion, where all the fuel and oxidizer are converted in the major species CO₂, H₂O,

N_2 , and O_2 . This implies that products of dissociation and other minor species are not taken into account. For port 6, in the post-reaction zone, this assumption is valid as the measured values of minor species NO_x , CO, and unburnt CH_4 are within the single-digit regime, hence negligible small. For the measurements at port 3, near the reaction zone, this assumption may become invalid. This depends on the local values of CO and CH_4 , if these become significantly large, combustion is no longer said to be complete.

Oxygen correction

Due to the changing operating conditions, the amount of excess air in the measured gas will vary, and therefore, the measured emission concentration varies as well. It is standard practice to correct the measured concentration of NO_x and CO to 15% O_2 in the reporting of emissions from gas turbines [66]. The correction is given in equation 6.27,

$$X_{corr} = X_{meas} * \frac{(20.96 - O_{2ref})}{(20.96 - O_{2meas})} \quad (6.27)$$

with X_{meas} the measured concentration in %vol, X_{corr} the corrected concentration, O_{2ref} the reference concentration O_2 (in this case 15%vol), and O_{2meas} the measured O_2 concentration in %vol at that condition. The use of equation 6.27 is recommended by the American Society of Mechanical Engineers (ASME), as discussed in the book on Flue and Exhaust Gas Analysis [67]. This method is also recommended by the Environmental Protection Agency (EPA) for the presentation of gas turbine emissions.

6.5.5. Encountered problems and solutions

Fluctuation in NO and NO_2 measurements

During some experimental runs, a sudden drop in NO_2 could be observed from the data. Examples of such a

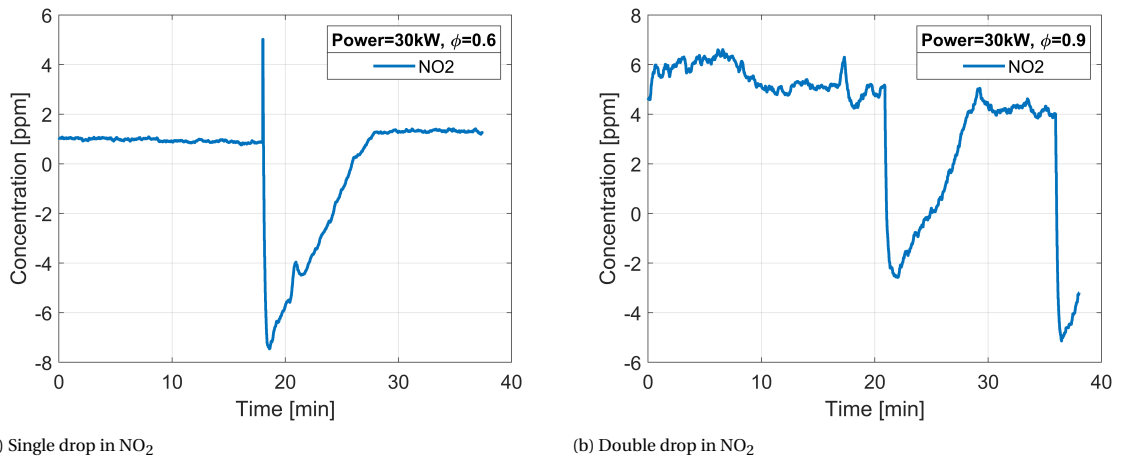


Figure 6.16: Drop in NO_2 during gas composition measurements, for two separate experimental runs

drop in NO_2 is shown for two different experimental runs; once at $P=30$ kW and $\phi=0.6$, figure 6.16a and twice at $P=30$ kW and $\phi=0.9$, figure 6.16b. This drop may be attributed to a water droplet carried by the flow into the Limas21 HW analyser, absorbing some of the UV light in the cuvette. Dust particles could also have entered the system as it was not fitted with a particulate filter. Initially, this was not deemed necessary, as the lean operating conditions in the combustor should not result in the formation of soot particulates. In addition, the hot sample gas is only cooled downstream of the Limas21 HW module to condensate any water vapour out of the sample before the flow enters the Uras26 and Magnos28 modules. The measured temperature at the exit of the sampling probe is in the range of 45–55°C, dependent on the depth of insertion into the combustion chamber. This is around the dew point temperature of the mixture, and hence, condensation might occur at the inlet of the heated sampling line. To investigate this issue, the relative humidity for different operating conditions is calculated according to

$$RH(\%) = \frac{p_{H_2O}}{p_{H_2O}^*} \quad (6.28)$$

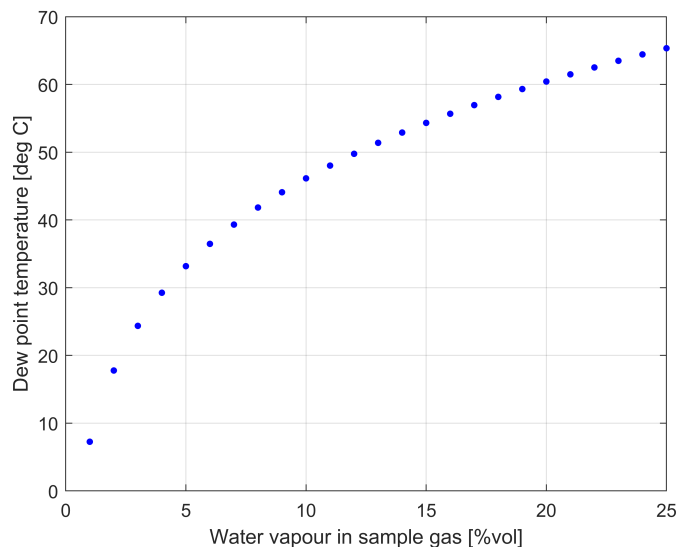


Figure 6.17: Dew point temperature as a function of the sample gas H_2O vapour pressure. Calculated using the Antoine formula [68]

where p_{H_2O} is the partial pressure of water vapour in the sample gas, and $p_{H_2O}^*$ is the equilibrium vapour pressure of water, based on the semi-empirical Antoine formula [68]. The Antoine formula is given as

$$p_{H_2O} = 10^{A - \frac{B}{C+T}} \quad (6.29)$$

with A , B , C component-specific constants, and T the sample gas temperature at the inlet of the heated sample line in $^{\circ}C$. The value for p in mmHg is converted into kPa by multiplying it with a factor of $\frac{133,322}{1000}$. For air, the constants read; $A=8.07131$, $B=1730.63$, and $C=233.426$. Equation 6.29 is used to calculate the dew point temperature assuming $RH=100\%$ for a variation in H_2O mole fraction, for which the results are presented figure 6.17. The gas temperature varies between $45-55^{\circ}C$ and is too low for most cases. For the NO_2 drop as seen in figures 6.16(a-b), the temperatures at the probe exit were $45^{\circ}C$ and $48^{\circ}C$ respectively, resulting in an estimated RH of 130% and 162%. It is recommended to keep the gas at the sampling probe exit above $60^{\circ}C$, for all cases, as this will result in $RH < 100\%$. The sampling line inlet temperature can be increased in two ways; either reduce the coolant flow rate, to reduce the amount of cooling of the sample gas or, the section of the probe outside the combustion chamber has to be insulated to reduce heat loss to the environment. The coolant flow rate can not be reduced too much, because this will be insufficient to cool the probe surface inside the combustor. A solution could be to reverse the cooling flow direction. First, it would cool the outside of the probe, before cooling the gas sampling tube. This can be achieved without requiring too many changes to the existing design. For the insulation of the probe, it is proposed to use ceramic insulation tape, as it has to withstand high temperatures close to the combustor.

Measurement drift

During the experiments, in some cases, a significant drift in NO_2 is observed. While running the experiment, there is not much the operator can do about this, as it would mean that the experiment has to be stopped to re-calibrate the analyser or purge the line. Therefore, the calibration values obtained before the experiment are saved, while the drift in the measured components after the experiments are also saved. A linear relationship is assumed between these two points and hence the measurements at specific time instants during this interval can be corrected with the estimated drift at that moment. The drift in the other measured components was negligible and therefore, these results have not been corrected.

To investigate the cause of this drift, a 24h stability test is performed for both the zero and span values. For the zero stability test, the analyser is connected to a bottle filled with pure N_2 . The analyser is zero calibrated on this bottle and kept connected for another 24 hours to see the drift in the measured value. The same procedure is followed for the span calibration. The analyser is connected and calibrated on the calibration gas bottle containing 8.1ppm NO_2 and rest N_2 . Again, the analyser is kept connected for another 24 hours to evaluate the drift in the measured value. The results for both tests are shown in figure 6.18. The results

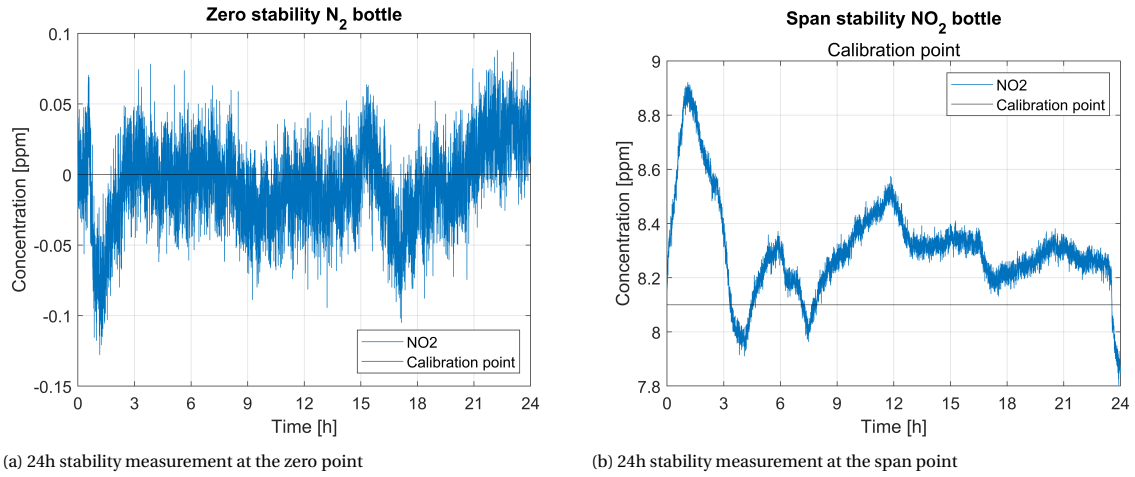


Figure 6.18: Zero and span stability test on the NO_2 component

for the zero stability test seem to be very good, the values fluctuate between ± 0.05 ppm (or ± 50 ppb). This is in accordance with the specifications as found on the analyser datasheet. The result for the span stability test shows a larger variation in measured values. For most of the time, the value is above the calibration point, with a peak value of 8.85 ppm within the first 3 hours. Moreover, the expected drift is not observed in both figures, this would be characterized by a steady decrease or increase over time, not a low-frequency cyclic behaviour. Because the analyser was connected to a bottle with dry gas, a variation in sample conditions is also unlikely due to the constant temperature and pressure. Therefore, these results seem to point towards a low-frequency cyclic behaviour originating from the analyser itself. The manufacturer will have to investigate this issue further as it might be caused by a component within the analyser module. Because the supplied dry calibration gasses do not contain any water vapour, these results seem to indicate that both the observed drop and drift in NO_2 , must be a result of condensed water droplets passing through the analyser. As discussed in the previous section, this is a very plausible explanation. The gas temperature at the inlet of the sampling line was below the dew point temperature for most of the experimental cases run. It could definitely contain condensed water droplets that accumulated and survived the heated sampling line to influence the measurement.

6.5.6. Probe induced disturbances

An overview of possible influences on intrusive gas sampling measurements for species concentrations is given by Heitor and Moreira [53]. The different aspects related to the probe design or operation relevant to the current experiments are discussed in this section. The design of the probe and the way in which the experiments have been performed, to a large extent, determine the accuracy of the gas composition measurement. During the design phase of the probe, as outlined in section 6.3, several possible sources of error have already been tackled by adjusting the final design.

Aerodynamic and thermal influences

The use of a cooled sampling probe will result in both aerodynamic and thermal disturbances to the flow. Because of the active cooling of the probe, it will act as a heat sink to the flow. The aerodynamic disturbances are twofold. First, the presence of the probe acts as an obstacle to the flow. The length scale of this disturbance is the diameter of the probe d_p . Inserting the probe in or near the reaction zone might stabilise the flame around the probe (bluff body flame stabilisation). This is a particular problem of the current setup because the probe is inserted radially. If the probe were to be inserted axially from the exhaust, this could have reduced the aerodynamic influence drastically. The influence of the probe on the flow is already estimated in section 6.3.2, the addition of 4 fins to the probe's outer surface reduced the downstream influence of the wake of the probe. The second is the influence of extracting the gas sample from the flow. The length scale related to this is the upstream diameter of the stream tube captured by the probe d_s . This stream tube diameter is estimated as

$$d_s = \left[\frac{\dot{m}_s}{\rho U 4/\pi} \right]^{1/2} \quad (6.30)$$

with \dot{m}_s the gas sampling mass flow rate, ρ the density of the gas at the sampling point, and U the free stream velocity at that point. To increase the spatial resolution of the measurements, d_s should be kept small and the variations in gas composition, temperature and velocity should also be small over this diameter. Typical values for the current setup are; the mean velocity at the sampling point, taken on the centreline at port 5 as $U=4$ m/s, the sampling mass flow is $\dot{m}_s=2.41 \times 10^{-5}$ kg/s, and the density at the sampling point being $\rho_s=0.7853$ kg/m³. This results in $d_s=2.45 \times 10^{-3}$ m, or 2.45mm. This is almost twice the sampling probe's inner diameter of 1.3mm.

Effectiveness of the quenching of the reactions

The effectiveness of quenching the reaction is important to freeze the local gas composition. According to Heitor and Moreira, the slow cooling of the gas sample can result in an error that is equivalent to an error in the positioning [53]. Care should be taken to cool the sample gas sufficiently quick, a reduction below 1000K within 1ms is desired in turbulent flames, to preserve the original gas composition. According to the thermal model developed, the reduction below 1000K is achieved in 0.4-0.6 ms, which is more than sufficient. However, the rapid cooling of the sample gas also promotes the combination of radicals, in the case of NO, the oxidation of NO in NO₂. This rate of oxidation is difficult to quantify and thus one of the reasons the total NO_x is presented in this report and not NO and NO₂ separately.

6.5.7. Influence of system inaccuracies

As discussed in section 3.2, the used mass flow control units provide air to the combustor with an accuracy of 1% FS. Due to the unit control, this results in small fluctuations in the airflow resulting in small fluctuations in the actual equivalence ratio. Moreover, an additional 10NLPM of air is supplied to the combustor through the pilot burner to prevent the nozzle from overheating. This excess air also influences the overall equivalence ratio. To quantify this influence, the actual equivalence ratio in the combustor is calculated based on the measured air and fuel flow rates during the experiments, according to equation 6.31

$$\phi_{meas.} = \frac{\dot{m}_f}{\dot{m}_{air_{comb.}} + \dot{m}_{air_{pilot}}} \frac{1}{FAR_{stoich}} \quad (6.31)$$

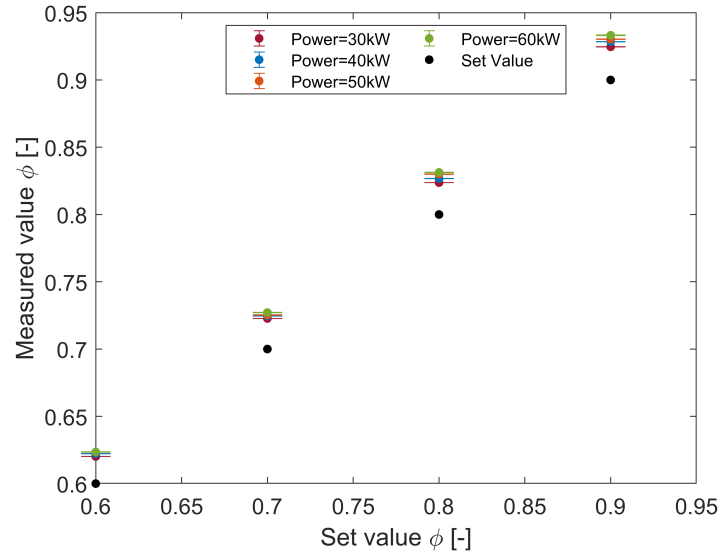
With FAR_{stoich} the stoichiometric fuel-to-air ratio by mass, in case of CH₄, $FAR_{stoich}=0.058$. The mean value and uncertainty margins have been determined for different conditions, these results are presented in figure 6.19. The measured ϕ seems to be consistently higher than the set values (given as input to the control system). When looking into the cause of this offset, the flow rate calculated by the control system was shown to be lower than it should be to achieve the set equivalence ratio. Hence, the issue seems to be with the calculation procedure used in the control system. Because this results in a constant offset, irrespective of the set operating conditions, as shown in figure 6.19, it is a systematic error. Moreover, the fluctuation in the measured flow rates is negligibly small, judging from the error bars in figure 6.19. As this approximates the actual conditions in the combustion chamber, the measured ϕ is also used in equation 6.26 to evaluate the mole fraction of H₂O and other major species under different operating conditions.

6.6. Results

Results of the gas composition measurements are presented in this chapter, with a special focus on the NO_x and CO components. The results presented are obtained for measurements on the combustor centreline at port 6. All operating conditions investigated are combined in a single figure, plotted vs the equivalence ratio ϕ . This allows for an extensive comparison between all the different operating conditions, as presented in table 3.2. The dark red markers correspond to an operating condition of 30kW, the blue markers correspond to an operating condition of 40kW, and the orange and green markers represent an operating condition of 50kW and 60kW respectively. The different marker symbols further indicate the specific cases of diluent, with the dot marker representing the non-diluted cases. For every symbol in the legend, except for the non-diluted cases, the diluent and oxygen concentration in the oxidiser stream (in %vol) is given. In all figures presented, a dotted red line is used to indicate the lower detection limit of the respective gas component. Any values that fall below the red line, are therefore assumed to be invalid.

6.6.1. O₂ concentration

Figure 6.20 shows the O₂ to decrease with an increase in equivalence ratio. Moreover, the addition of N₂ and CO₂ further reduces the oxygen concentration in the gas sample. Interestingly, the measured values are

Figure 6.19: Offset of calculated ϕ from set valueFigure 6.20: Measured O_2 on the combustor centreline for a range of ϕ at port 6

higher than expected for all the operating conditions investigated. Equilibrium values calculated from the combustion equation (eq. 6.26), show the value for O_2 to decrease from 8.4 to 1.6 %vol. with an increase in equivalence ratio. The high O_2 values might be explained by the addition of cooling air to the flow near the exhaust duct. As explained from figure 3.1, cooling air is supplied to the flow at the exit of the combustor to form a layer of film cooling between the exhaust duct and the hot gas. The sudden contraction at the combustor exit creates recirculation zones in that region. The cooling air that is radially injected might be entrained by these recirculation zones and is transported upstream towards the location of port 6. To investigate the upstream influence of this cooling air entrainment, the oxygen concentration at port 3 is also calculated near the centreline in the central recirculation zone. These results are shown in figure 6.21.

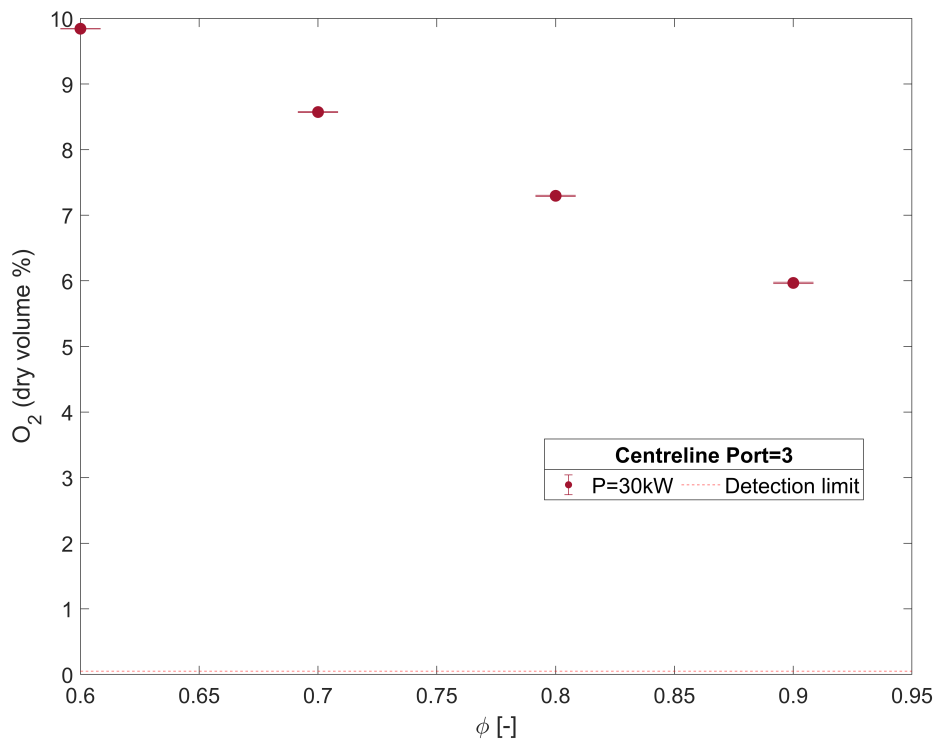
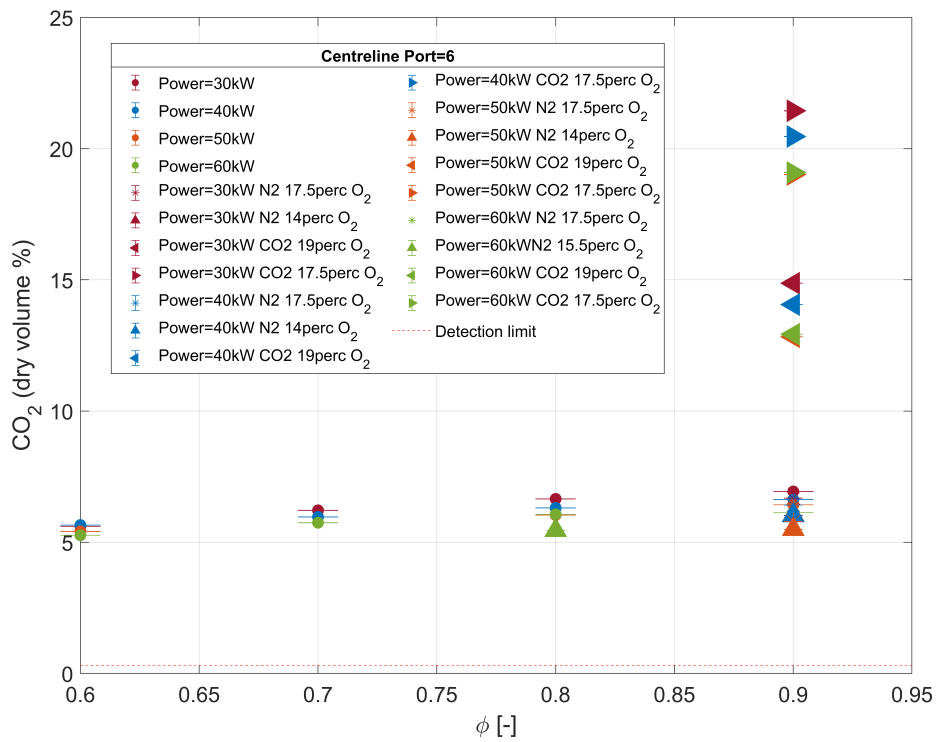
The oxygen concentration on the centreline at port 3 is seen to be lower compared to the values obtained at the exit of the combustor. Nonetheless, these values are still too high compared to equilibrium values under similar conditions. This indicates that cooling air is entrained upstream, as far as port 3, near the reaction zone. As a result, the local equivalence ratio may deviate from the set point value. In addition, the presence of cooler air might locally cool the flame.

6.6.2. CO_2 concentration

Figure 6.22 shows a steady increase in CO_2 with equivalence ratio and thermal power. The highest values in measured CO_2 are ascribed to the cases with CO_2 dilution. Adding CO_2 to the oxidizer mixture obviously increases the CO_2 measurement in the flue gas, whereas the addition of nitrogen will lower the volume percentage slightly. The non-diluted CO_2 values are lower compared to the values obtained from the equilibrium calculations. This difference is explained by the aforementioned entrainment of cooling air near the exhaust. CO_2 values are also measured near the reaction zone at port 3. These results are plotted in figure 6.23. The same trend is observed with a variation in equivalence ratio for a thermal power input of 30kW. Nonetheless, the values measured at port 3 are consistently higher, close to the equilibrium values, compared to the downstream measurement. It seems the dilution of CO_2 with excess air from the exhaust is less significant at port 3.

6.6.3. NO_x concentration

Although NO and NO_2 are measured separately, they are presented in their combined form of NO_x , the results shown in figure 6.24. Differentiation between both is difficult, as NO oxidizes into NO_2 as the temperatures

Figure 6.21: O_2 on the combustor centreline at port 3Figure 6.22: CO_2 on the combustor centreline for a range of operating conditions at port 6

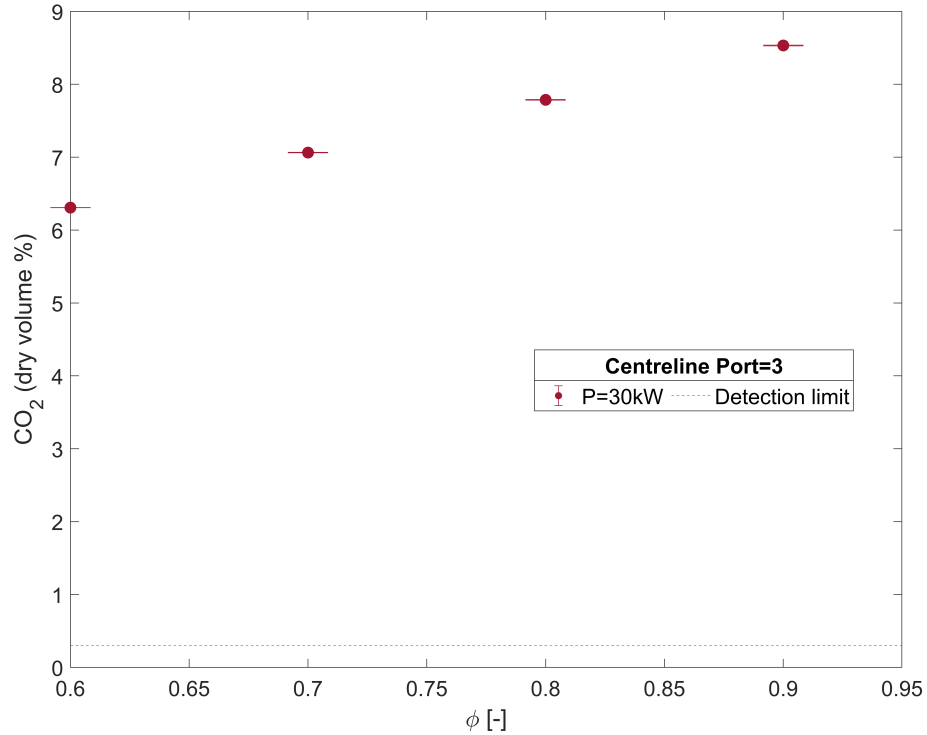


Figure 6.23: CO₂ on the combustor centreline at port 3

are reduced in zones of considerable excess air [36]. Moreover, the measured values may also be biased due to the oxidation of NO into NO₂ by quenching effects on the walls of the probe [36]. Therefore, only NO_x is presented as this omits the discussion on the oxidation of NO. At first glance, all values are seen to be in the single-digit regime, ranging between 0.5-7ppm. This is already very low, however, a clear distinction can still be observed between the different operating conditions investigated. With an increase in equivalence ratio, the values for NO_x are also seen to increase. Furthermore, with a decrease in the operating power, an increase in the NO_x fraction is observed. This seems to indicate that lower amounts of NO_x are produced at higher operating powers. This observation is most likely linked to a decrease in residence time in the combustor. The increased fuel and air flow rates at higher operating powers result in higher velocities within the combustor and hence a lower residence time limiting the NO_x production. To further focus the investigation on the influence of adding N₂ or CO₂ to the flow, the NO_x measurements are plotted against the oxygen concentration in the oxidiser as opposed to the equivalence ratio, see figure 6.25. This is shown to drastically reduce the NO_x concentration at the exhaust. Regardless of the power settings at $\phi=0.9$, the NO_x concentrations can be more than halved depending on the extent of the dilution, with most values below 3ppm. Dilution with CO₂ seems to be more effective in reducing the NO_x concentration compared to dilution with N₂. For the cases with similar oxygen concentration ($X_{O_2} \approx 17.5\%$ vol), for dilution with CO₂, the measured NO_x values lay consistently below the values obtained with N₂ dilution, as observed from figure 6.25. An explanation can be found in the higher thermal capacity of CO₂ as compared to N₂. This will result in a lower gas temperature at the same operating points and hence the production following the thermal pathway is becoming less significant. Because the thermal pathway is considered to be the main contributor to the total NO_x production in gas turbine combustion, this can make a significant difference. The lowest (valid) NO_x concentration is measured for dilution with N₂ at a condition of 60kW and $\phi=0.8$. This value lies around 0.5 ppm, just above the detection limit for this component. Because dilution with CO₂ has not been performed at this operating point, it is not possible to comment on the effectiveness of carbon dioxide dilution with respect to nitrogen under these conditions. As a final observation, it is interesting to point out the low NO_x values obtained at lean operating conditions ($\phi < 0.7$). Increasing the amount of excess air has the same effect on the production of NO_x, as adding dilution to the flow. Both options rely on a reduction in flame temperature, either by

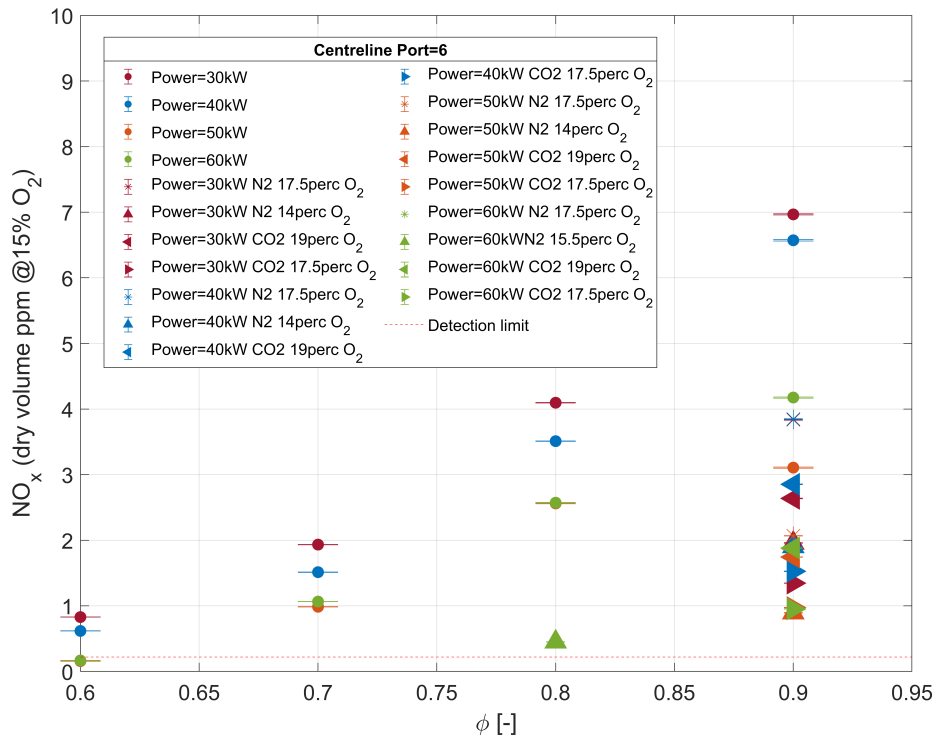


Figure 6.24: NO_x on the combustor centreline for a range of operating conditions at port 6

increasing the amount of excess air or reducing the oxygen concentration. Furthermore, lowering the equivalence ratio to $\phi=0.6$ seems to be even more effective in reducing NO_x than by adding dilution at a higher equivalence ratio.

6.6.4. CO concentration

The variation in CO with the operating conditions is given in figure 6.26. For all non-diluted cases, except for 60kW and $\phi=0.6$, the measured values are below the detection limit and are thus deemed invalid. This result is indicative of complete combustion, as CO is negligibly small. The higher value for CO at P=60kW and $\phi=0.6$ indicates that local extinction events start to occur resulting in the onset of incomplete combustion. According to Lefebvre [36], CO emissions are formed in significant quantities when the peak temperature is relatively low, due to incomplete combustion of the fuel. At lean conditions, this may occur at a higher power setting due to a reduction in the burning rate of the fuel combined with a shorter residence time. Lefebvre further showed the CO level to rise significantly below $\phi<0.6$, because of the slow rate of oxidation. Inadequate mixing of the fuel and an oxidiser can also result in an increase in CO, however, for the current premixed system, this seems unlikely.

To investigate the influence of adding N₂ and CO₂ to the flow, the CO measurements are plotted against the oxygen concentration in the oxidiser as opposed to the equivalence ratio. Noteworthy is the fact, that a measurable increase in CO is almost exclusively measured for dilution with CO₂ and not so much for dilution with N₂. For the cases of 40, 50, and 60 kW, both cases of dilution with CO₂ give the highest reading in CO. This observation might be explained by one of two different processes. Either the addition of CO₂ to the flow increases the thermal capacity and thus reduces temperatures in the flame zone resulting in local flame quenching and incomplete combustion. Or, the higher concentration of CO₂ in the mixture allows for more dissociation of CO₂ into CO and O₂ at elevated temperatures. This latter explanation seems to oppose the general trend that CO values are decreased by oxidation with O₂ into CO₂ downstream of the reaction zone. To shed some light on this matter, it is helpful to look at the CH₄ measurements for the different cases with dilution.

The elongation of the reaction zone in the downstream direction under varying equivalence ratios is in-

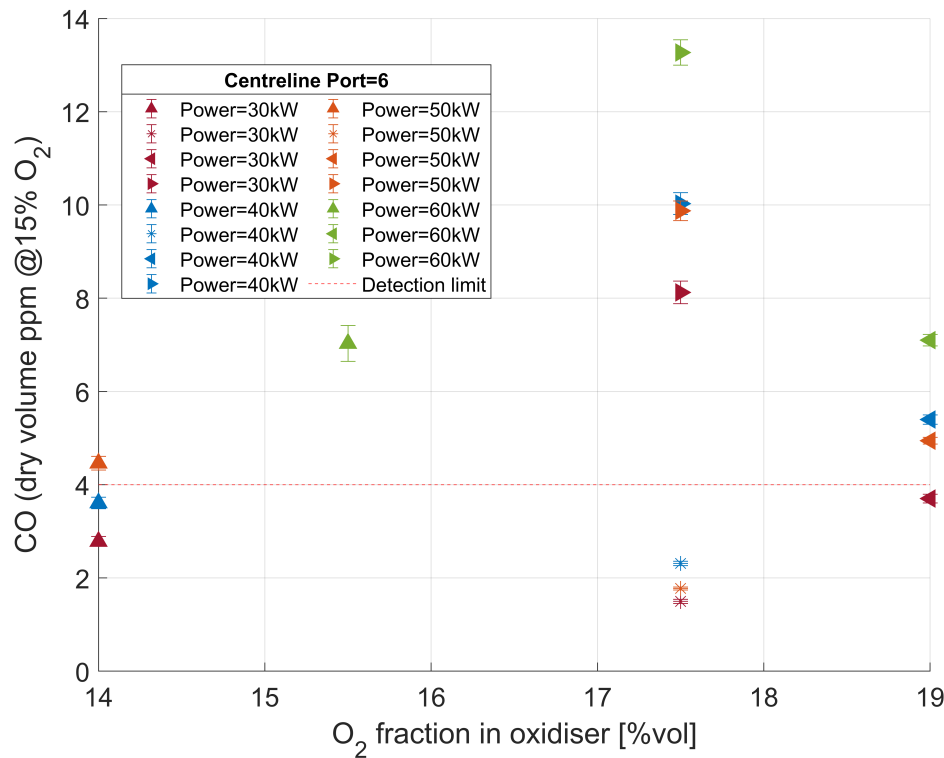


Figure 6.27: Measured CO for the cases with dilution vs the oxygen concentration in the oxidiser at port 6

vestigated by measuring the CO and CH₄ components at port 3 at different radial positions. This location is assumed to be near the reaction zone. The results for the CO component is shown in figure 6.28.

In comparison to the measured values at port 6, which are mostly below the detection limit of the analyser, the currently measured values are way higher. This indicates the presence of a reaction zone. The initial assumption of this location to be near the reaction zone is thus verified. All plotted radial profiles of CO show a clear increase at a location of 26 mm from the wall. Measurements at this location are probably nearest to the reaction zone. Mapping this location on the reacting flow field contour plot, shows it to be around the velocity half-width line of the jet, see figure 3.6. Comparing the different operating conditions (constant power and varying equivalence ratio), show an increase in CO with a decrease in equivalence ratio for all radial positions. The cases of $\phi=0.6$ and 0.7 stand out in this regard. These display significant higher values, peaking at 1400 and 1000 ppm respectively. This proves that the reaction zone is elongated in the downstream direction, by operating under leaner conditions. Additionally, the reaction zone seems to widen with a decrease in equivalence ratio, indicated by the higher values of CO over a wider range. To conclude, with a decrease in equivalence ratio, the reaction zone is shown to elongate and widen, at an axial location of 140mm from the burner head.

6.6.5. CH₄ concentration

The measurement of unburnt hydrocarbons, in this case, CH₄, reconfirms the aforementioned observation that combustion is assumed complete for all cases investigated at port 6, 290mm from the burner head. The measured values stay below 15 ppm at all times. In addition, this is far below the theoretical detection limit of the analyser, therefore, it is assumed there is no measurable unburnt fuel present in the sample gas. This confirms the achievement of complete combustion. Moreover, this observation seems to disprove the idea that the increase in CO with CO₂ dilution is due to flame cooling and incomplete combustion. Higher values for CH₄ are expected in that case. The process of dissociation of CO₂ in CO and O₂ is shown to be the major contributor to the formation of CO.

Similarly to the measurement of CO over a range of radial positions at port 3, the CH₄ values are also measured at those same locations. The results are shown in figure 6.30. The results obtained by the CH₄

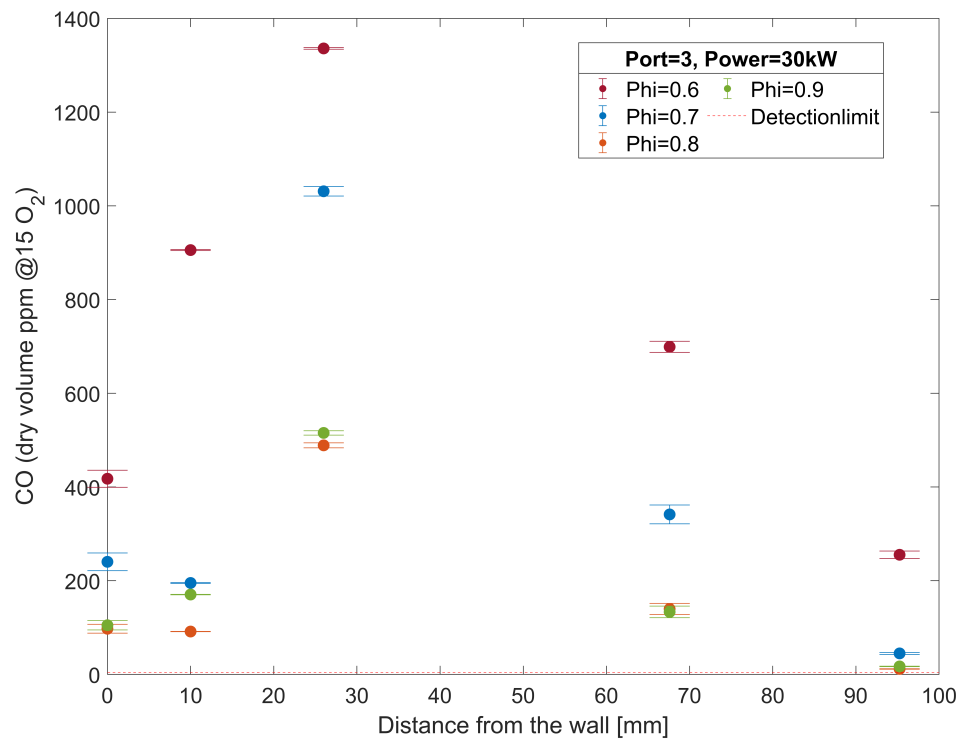
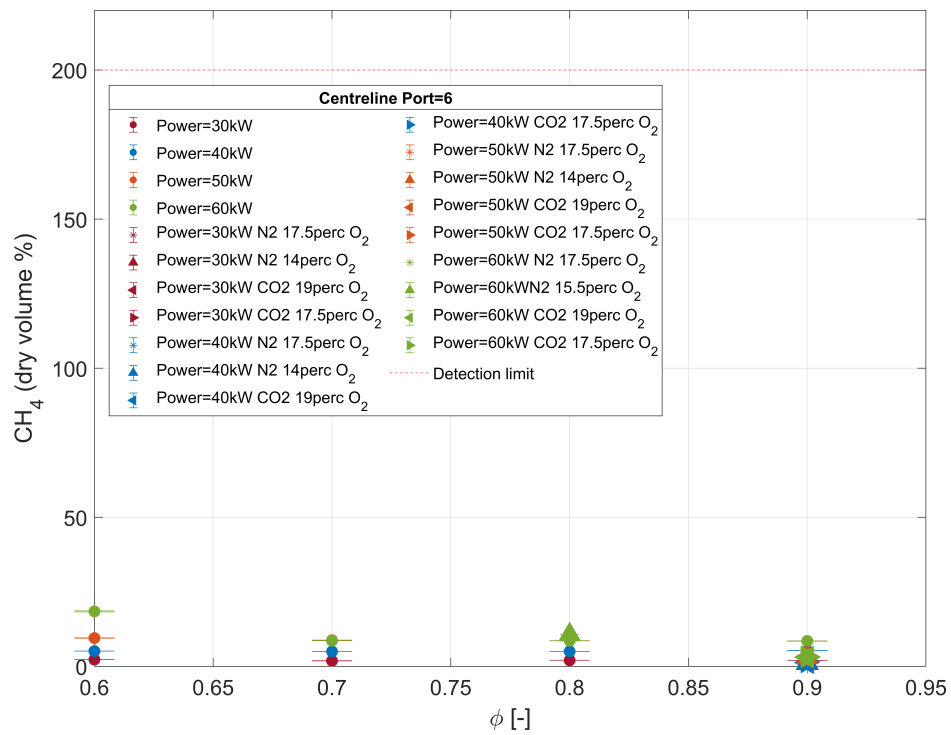


Figure 6.28: Radial profiles of CO vs equivalence ratio at port 3

Figure 6.29: CH₄ on the combustor centreline for a range of operating conditions at port 6

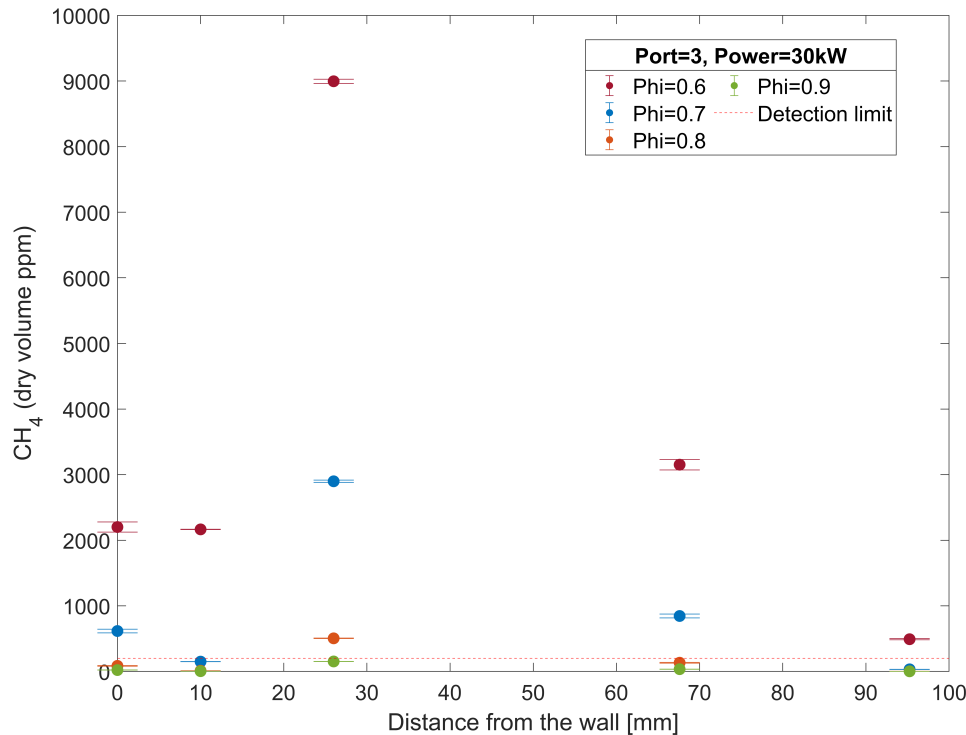


Figure 6.30: Radial profiles of CH₄ vs equivalence ratio at port 3

measurements reconfirm the aforementioned observation of elongation and widening of the reaction zone at 140mm from the burner head. High values of unburnt CH₄ are measured for the two leanest operating points. The measured values for the cases of $\phi=0.8$ and 0.9 are almost all below the detection limit and are thus invalid. This indicates completed combustion at this location for these operating conditions. Referring to the measured values of CO for the same operating conditions, these peak around +500 ppm. It seems that even though combustion has been completed previously, still significant amounts of CO can be measured. This points towards the presence of a post-flame zone, where the remaining CO is oxidised into CO₂. Again, the peak in measured CH₄ is found for an operating condition of $\phi=0.6$, with a value of 9000ppm or 0.9%vol. At $\phi=0.6$ and to a lesser extent $\phi=0.7$, combustion is clearly not complete yet and hence the reaction zone is expected to extend further than 140mm downstream of the burner head. Interesting to note is the low values of CH₄ measured near the centreline of the combustor. Except for the case of $\phi=0.6$, the measured values are close to zero, below the detection limit. This indicates fully completed combustion for all operating points. This radial location is assumed to be in the recirculation region of the combustor. The non-reacted methane at lower equivalence ratios is thus burnt further downstream before the flow is recirculated. The slightly higher value for $\phi=0.6$ might be due to some local recirculation of unburnt methane that is transported back in the direction of the burner head.

Results Analysis & Discussion

The results stemming from the different experimental techniques have been discussed separately in their respective chapters. This chapter combines the main results to find relations between observations made for the different experimental campaigns. In addition, the obtained results are compared to available literature, for example, from experimental research on comparable combustor setups.

7.1. Flow field characteristics

The main results following the PIV analysis of the flow field under reacting and non-reacting conditions are presented in this section.

First of all, it can be stated that we have successfully applied the PIV method for flameless combustion experiments. After overcoming multiple difficulties and problems with the implementation of the PIV method in a reacting environment, as was discussed in section 4.4.3, measurements were obtained with good quality and high spatial resolution under different operating conditions. It took multiple PIV campaigns before the final results were obtained, which exemplifies the extensive experience required to perform these experiments. Moreover, it highlights the value of the obtained datasets, which can be used for the future validation of numerical models for the simulation of this combustor.

The main flow structures of the recirculating flow could be identified for both the reacting and non-reacting cases. The location of both the peripheral and central recirculation zones is independent of the operating conditions. The curving of the jet flow due to the Coanda effect is observed in all cases investigated. This curvature is more gradual for the reacting flow case than the non-reacting case due to the heat release and accompanying gas expansion. The entire recirculation zone could not be visualised with the current FOV. Therefore, it is difficult to judge how far this will extend downstream and if it plays a significant role in the entrainment of cooling air injected near the exhaust duct.

Although the flow structure is similar to the reacting and non-reacting isothermal flows, significant differences are found in the flow's axial velocities and turbulent characteristics. The axial velocity increases under heat release, with a relatively higher velocity in the CRZ. This results in a larger and broader velocity gradient in the radial direction, resulting in higher levels of turbulence, distributed over a larger area, in the CRZ.

It is shown that reacting and non-reacting experiments can be interchanged to analyse the flow field structure if the focus is on identifying the location of the recirculation zones. However, when the investigation focuses on local flow characteristics such as the level of turbulence or the flow time scales. The reacting and non-reacting flow experiments are not interchangeable anymore, and PIV under reacting conditions is necessary for a fundamental characterisation of flameless combustion.

7.2. Temperature & Gas composition

7.2.1. Thermocouple measurements

The acquired ceramic shielded thermocouple did not perform very well. A significant temperature correction of around 40-60% of the measured value was calculated to be necessary to correct for radiation losses,

due to the large surface area of the thermocouple. The size of the thermocouple also had a significant influence on the flame and flow field. Therefore, another thinner platinum alloy thermocouple was acquired, which proved to be more accurate. With the same correction method applied, the maximum temperature correction is only 10% of the measured value, similar to results presented in the literature [53]. The platinum thermocouple measurements also gave more sensible results in the near-wall region. When comparing the corrected temperature readings, the ceramic thermocouple significantly overestimated the gas temperature. It is thus decided to continue the experiments with the platinum thermocouple. Additionally, the quick response time of the thinner platinum thermocouple allows for slow traverse temperature remeasurements, previously not possible with the ceramic thermocouple.

The platinum thermocouple is used for both point measurements and continuous traverse measurements near the reaction zone. The point measurements are used to validate the radial temperature profiles, which are seen to correlate well. The resulting radial temperature profiles show a significant decrease in temperature towards the wall, where the temperature drops from around 1100-1400°C at the centre to around 800°C at the wall. Peak values are found at the radial location of the nozzle, measuring up to 1500°C. The temperature profiles are seen to flatten with a decrease in equivalence ratio, indicating distributed combustion. The significant drop near the wall results from heat losses by both convection and radiation to the environment. This heat loss is increased by the external cooling air blown along the length of the combustion chamber. The maximum measured temperature at the centreline increases with an increase in equivalence ratio and thermal power input.

7.2.2. Gas composition measurements

The gas analysis system is designed, acquired and tested for the current setup. It can be concluded that it works well under the currently investigated conditions. The system can measure NO_x emissions accurately in the ultra-low (0-10 ppm) range, as requested. The drift and accuracy of the system, decoupled from the gas extraction probe, are also within reasonable limits, as shown by the 24hr drift test on the NO_2 component. The zero point test showed the NO_2 analyser to have no drift with a fluctuation of measured values within a range of ± 50 ppb. The span drift was shown to be much larger, displaying a combined low- and high-frequency fluctuation in measured values. It shows a low-frequency fluctuation of about ± 750 ppb, with a high-frequency fluctuation superimposed of about ± 75 ppb. Because this value is considerably larger than the measurement fluctuation specified in the datasheet, this fluctuation is currently being investigated by the analyser manufacturer.

For the current campaign, it is assumed this low-frequency fluctuation did not influence the measurements, as measurements are only taken for about 200 seconds, way smaller than the fluctuation period. With regular calibration of the analyser, the influence of this fluctuation is vastly reduced. The remaining issues with high-frequency fluctuations or sudden drops in the measurement remained. These are due to excessive cooling of the sampled gas flow by the convection quenched probe. The measured temperature of the sampled gas, at the probe exit, is below the dew point temperature, resulting in condensation of water vapour in the probe. The consequences of this are twofold; first, the measured NO and NO_2 values will probably be under-predicted because these components are soluble in water. Secondly, formed water droplets may travel downstream with the flow and influence the UV absorption in the analyser unit, resulting in an unrealistic drop in measured values. The latter can be solved by redesigning the cooling arrangement and insulating the external section of the probe, reducing heat loss. Nonetheless, the currently obtained measurement accuracy is still more accurate compared to the accuracy in measured NO_x obtained by Vaz [8].

The thermal model developed in MATLAB for the design of the gas sampling probe does not correlate well with experimental data. The estimated gas temperature and coolant exit temperature are greatly under-predicted. This is due to the model's limited ability to predict the probe's external cooling by both conduction and convection. This model can not be used to estimate the gas temperature at the sampling point.

From the measured values of NO_x and CO , it can be concluded that the combustor operated very well from an emission standpoint. For all cases investigated, the NO_x values remained below 7 ppm, with the lowest measured values below 1 ppm for a lean operating condition of $\phi=0.6$. This research shows that NO_x emissions can be reduced by lowering the oxygen concentration or by operating under lean conditions ($\phi<0.7$). Furthermore, reducing the equivalence ratio proved to be more effective in reducing NO_x compared to adding dilution at high equivalence ratios. The values for CO remained below the detection limit of the analyser unit (being 4ppm) for almost all operating conditions. The low values for CO and CH_4 indicate that complete

combustion is achieved at 290mm from the burner head for all operating conditions investigated. The stability of the combustor has not been investigated in-depth. However, stable combustion could be achieved as low as 30kW with an equivalence ratio of $\phi=0.6$. The only indication of the onset of incomplete combustion is observed for the case of 60kW and $\phi=0.6$. This condition is characterised by a small increase in CO levels due to a reduction in oxidation rates within the flame zone resulting in local flame extinction. The addition of CO₂ to the oxidiser also increases the CO level due to the dissociation of CO₂ into CO and O₂. Radial gas composition measurements at port 3, 140mm from the burner head, have shown the reaction zone to extend towards this location for lean operating conditions $\phi<0.7$ as indicated by a significant increase in CO and CH₄. Peak values exceeding 1000 and 4000 ppm respectively were measured, indicating incomplete combustion. Additionally, the reaction zone is seen to widen as well under those operating conditions, again observed from a significant increase in CO and CH₄ in the radial direction.

Values of O₂ measured at ports 6 and 3 are seen to be higher than expected from equilibrium calculations. This is due to the entrainment of cooling air into the combustor. Cooling air is injected radially near the exhaust to cool the exhaust duct. However, with recirculation at that location due to the contraction of the tube, the cooling air might be entrained upstream. The central recirculation flow transports the cooling air towards the burner head.

7.2.3. NO_x formation pathways

The gas temperature and NO_x emissions measured over a range of equivalence ratios are presented in figures 7.1(a-d). Every figure represents a specific power setting. The general observation is an increase in NO_x with an increase in gas temperature. NO_x emissions are seen to reduce with a decrease in equivalence ratio and an increase in thermal power input. Regardless of the operating conditions, the NO_x values are consistently low in the single-digit regime. These results indicate that ultra-low NO_x combustion is achieved for all conditions investigated. These ultra-low NO_x levels are attributed to the low maximum temperature in the combustor. As seen in figures 7.1(a-d), the temperatures at $\phi=0.9$ are in a range of 1300-1375°C, or 1573-1648K, nowhere close to reaching the thermal NO_x threshold of 1800 K. Although these temperatures are measured on the centreline and not in the reaction zone, radial temperature trends at port 3 show the temperatures to remain below the thermal NO_x threshold at the reaction zone as well. The production of NO_x is thus governed by another pathway rather than the thermal pathway. Because of the absence of nitrogen in methane, the fuel-bound NO production is also not present. Three possible mechanisms for producing NO_x remain; the NNH, N₂O, and prompt mechanisms. The latter is not deemed significant because of the lean operating conditions. This specific mechanism becomes dominant under low-temperature rich conditions. This leaves the NNH and N₂O pathways as the two most likely mechanisms for producing NO_x under the operating conditions investigated. The nitrous oxide (N₂O) pathway is the dominant mechanism at low temperatures in lean pre-mixed combustion [36]. The NNH mechanism becomes more important for fuels containing hydrogen with large carbon to hydrogen ratios [15]. Based on the currently obtained results, the relative importance of both pathways could not be determined.

7.3. How do these results relate to available literature?

The achieved ultra-low NO_x emissions are a characteristic of lean combustion with flame temperatures below 1800K. Leonard and Stegmaier found the NO_x component to be less than 2ppm for almost perfectly premixed combustion with a flame temperature below 1900K [69]. The current results are slightly higher, towards 7 ppm for $\phi=0.9$. Leonard and Stegmaier further concluded that in the case of extremely well-mixed combustion, NO_x does not increase with residence time. This observation also does not seem to agree with the currently obtained results. The higher NO_x values found for lower operating powers are most likely attributed to the longer residence time in the combustor.

Comparing these results with the results by Vaz, obtained on a comparable setup, they seem to confirm the general trend of ultra-low NO_x emissions regardless of the operating condition [8]. For a similar operating condition, the currently measured NO_x and the values obtained by Vaz are low in the single digit ppm range. It is important to note that values presented in this research are corrected to 15 vol% oxygen, whereas the values by Vaz are not corrected. Additionally, Vaz only measured the NO component, whereas in this case, both NO and NO₂ are measured. The obtained gas temperatures are also comparable for similar operating conditions, below the thermal NO_x threshold. Hence, the same conclusion is drawn on the production of NO_x, identifying the N₂O mechanism as the most likely formation mechanism. Vaz did not comment on the possibility of the formation of NO_x via the NNH mechanism. The uncorrected CO₂ values seem to be

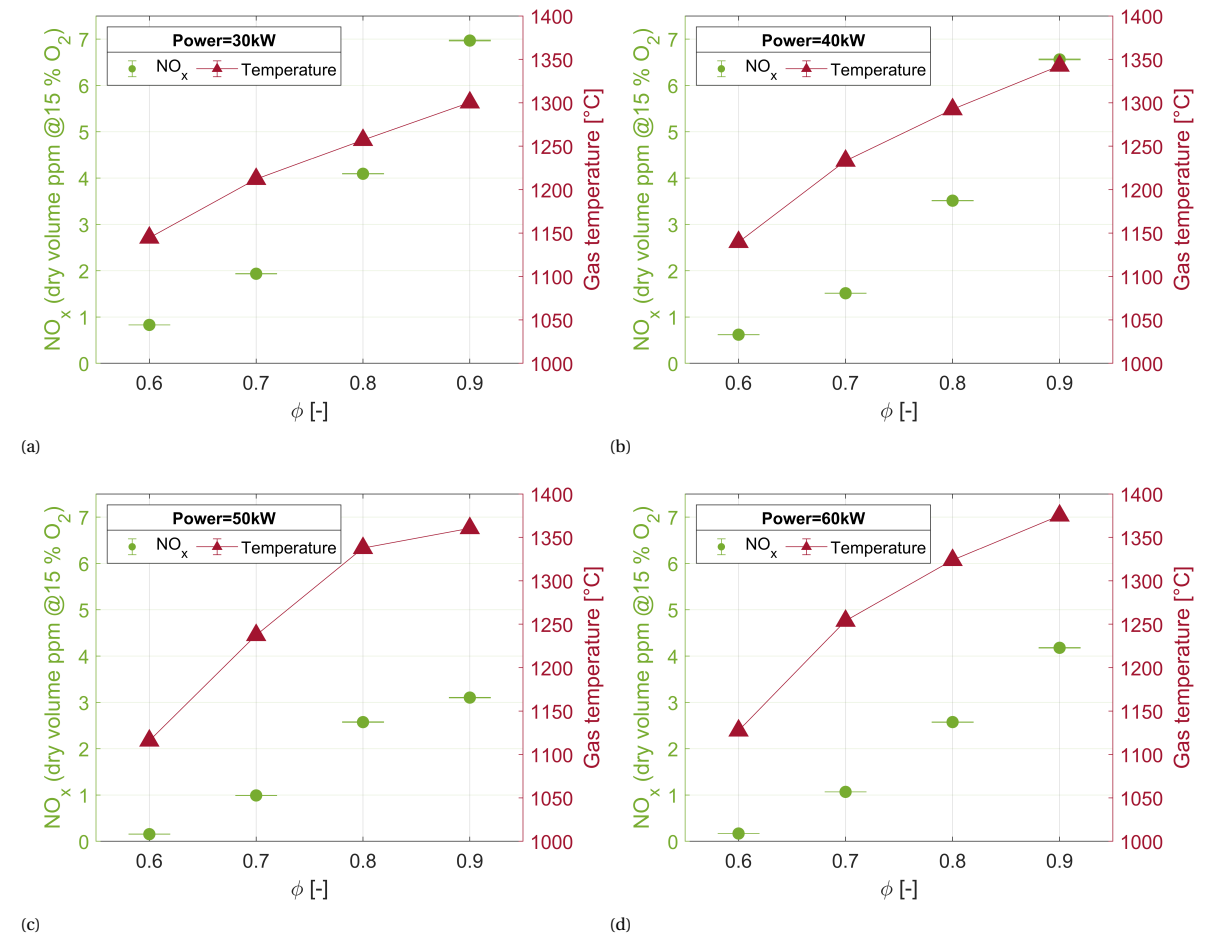


Figure 7.1: NO_x and temperature trends for a variation in ϕ at 4 different power settings

comparable to the values measured by Vaz [8]. A difference is seen in the value for O_2 , which is higher for the current research. This, again, is explained by the entrainment of cooling air into the combustion chamber.

When comparing the currently obtained results with the experimental work by Veríssimo [70], they are seen to be opposing each other. In the work of Veríssimo, flameless combustion is achieved for low excess air ratios. With an increase in excess air, comparable to a reduction in ϕ in our case, the flame moves closer to the burner head and becomes less distributed. For the current research, the opposite is observed; reducing ϕ extends and widens the reaction zone further downstream, indicated by an increase in CO and CH_4 at port 3. Veríssimo reported the measured NO_x to also decrease for a reduction in excess air. The lowest values are obtained just shy of stoichiometric conditions ($\lambda=1.1$, or $\phi=0.91$), reading $NO_x \approx 4$ ppm. Again, this is the opposite behaviour as observed in the current research, where NO_x increases with a decrease in excess air. The differences can be explained by the difference in burner head layout. For the current setup, the fuel and air are premixed before being injected into the combustion chamber. The setup by Veríssimo consists of a large central air injection nozzle with radially distributed fuel nozzles around the central air nozzle that inject the fuel straight into the recirculated flue gas before being combusted. The emission and flame zone characteristics are thus related to the central air jet momentum and degree of mixing of the reactants. These opposing trends emphasize the difficulty in deriving general trends in attaining flameless or distributed combustion, as this is strongly dependent on the burner head layout. Similarities to the current work are identified as well. Veríssimo observed very low NO_x and CO emissions for all operating points investigated as well, attributed to the suppression of the thermal mechanism.

The original definition of flameless combustion by Wüning and Wüning [18] is based on non-premixed combustion. In non-premixed combustion, fuel and oxidiser streams are separated, and chemical reactions only occur at the locations where both streams merge. This will inherently produce higher levels of NO_x emissions compared to premixed combustion. When the fuel and oxidiser streams meet, the mixture approaches stoichiometric conditions, resulting in high peak temperatures and significant NO_x production following the thermal pathway. In that case, the shift towards flameless combustion is more a shift from non-premixed to partially premixed combustion, in contrast to the current setup, which is consistently operated under lean premixed conditions. Because this shift in operating regime is not occurring, the peak temperatures and related emissions are inherently lower for all operating conditions. The significant drop in NO_x emissions as seen by Wüning and Wüning, from 160 ppm in conventional mode to 6 ppm in flameless mode, is not observed in the current case. Although a clear trend is observed in decreasing NO_x emissions by going lean or adding dilution to the flow, this will only result in a drop of a few ppm. With this, it can also be noted that the current setup is not operated in a purely conventional combustion mode during the experimental campaign. Because the combustor relies on internal recirculation to achieve stable combustion, dilution of the oxidiser stream will always occur under all operating conditions investigated. Thus, a shift from conventional to flameless mode is not achieved for the current cases.

8

Conclusions & Recommendations

This chapter is subdivided into a conclusions and recommendations section. The research questions are answered in the first, and recommendations for future research based on the observations and conclusions are discussed in the second.

8.1. Conclusions

This thesis research covers the experimental characterisation of a flameless combustion setup at the combustion lab of the faculty of aerospace engineering at TU Delft. This setup is used to investigate the possibilities of attaining flameless/distributed combustion to lower the emission of pollutant species with a special focus on reducing NO_x and CO emissions. This work focussed primarily on designing and applying existing experimental techniques in reacting and non-reacting flow environments. Throughout this work, the following techniques have been applied; Particle Image Velocimetry (PIV) for evaluating the flow field under reacting and non-reacting conditions. Thermocouple measurements inside the combustor are used to evaluate the temperature profiles. Gas composition measurements near the exhaust and for limited operating conditions near the reaction zone are used to measure the emission of pollutant species. All these measurements have been performed for a variation in operating conditions, varying the thermal power input, equivalence ratio and oxygen concentration in the oxidiser stream. The results obtained with these experimental techniques are discussed in their respective chapters. The main conclusions from this research are summarised in this chapter, first by providing answers to the separate research questions and finally by commenting on the research objective.

- *Which experimental techniques are best suited to be used on a flameless combustion setup?*

Particle image velocimetry, high-temperature platinum thermocouples, and extractive gas composition measurements are best suited to be used on the current setup.

- *Is the flameless combustion setup able to achieve ultra-low emission combustion (CO & $\text{NO}_x < 10\text{ppm}$)?*

Yes, the flameless combustion setup is able to achieve ultra-low emission combustion. Near the exhaust, the measured CO is very low, below 4ppm, while the measured NO_x remains consistently below 7 ppm.

- *Which parameters will have a positive effect on the reduction of CO and NO_x emissions?*

1. *Thermal power input*
2. *Equivalence ratio*
3. *Oxygen concentration in the oxidiser stream*

The thermal power input positively influences the reduction of NO_x and has a negligible effect on CO, which remained below the detection limit of the analyser. Decreasing the equivalence ratio ϕ positively influences the reduction of NO_x and has a negative effect on CO, where CO is seen to increase at $\phi < 0.6$

for higher thermal power inputs. Reducing the oxygen concentration positively influences NO_x and has a negative effect on CO, especially for dilution with CO_2 .

- *What are the observed differences in flow field characteristics under reacting and non-reacting conditions?*

The general flow field characteristics, such as the location of the Peripheral Recirculation Zone and Central Recirculation Zone, are largely the same. The differences are observed in the axial velocities and levels of turbulence in the Central Recirculation Zone.

The main objective of this thesis research is

The experimental characterisation of a flameless combustor under varying operating conditions.

The main objective of this thesis research is achieved through the application of various experimental techniques to characterise the flow field, local temperatures and gas composition within the combustor over a range of operating conditions. Both reacting and non-reacting conditions have been investigated to characterise the flow field. For the reacting flow conditions, temperature and gas composition measurements have also been performed at four different power settings ranging from 30 to 60kW and four equivalence ratio settings ranging from 0.6 to 0.9. Finally, dilution has been added to the oxidiser stream to simulate reduced oxygen inlet conditions. The analysis of these parameters indicated which operating parameters would positively influence the reduction in NO_x and CO, achieving ultra-low emission combustion.

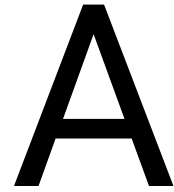
8.2. Recommendations for future research

The following recommendations for future research are made based on the results obtained by this research.

- When doing the experiments, a flame was always visible, even for lean or diluted conditions. Based on the definition of flameless combustion being purely based on the luminosity of the flame, flameless combustion is never achieved. Nonetheless, ultra-low NO_x emissions have still been achieved. Based on this result, it is proposed to rethink the definition of flameless combustion. Because the objective is to reach ultra-low NO_x combustion and not necessarily ultra-low luminosity combustion, the definition should focus more on the emissions rather than the ability to see the flame. The measured NO_x is within a range of 0.5-7 ppm, similar levels to what is often attributed to flameless combustion.
- Two possible pathways for the formation of NO_x have been proposed in this research. However, the current research could not determine the relative importance of both based on the obtained data. Therefore, it is recommended to gain more insights into the possible NO_x production pathways by looking at pre-cursing radicals and intermediate species, for example, from CRN modelling.
- For future research, it is recommended to research the combustor stability at higher power levels as well. The current study is limited to a range of operating powers of 30 to 60kW. However, to reach industrial micro-gas turbine conditions, the power density must be increased by running at higher power settings. In addition, the higher velocities in the flow field might cause stability problems when adding dilution or shifting towards leaner fuel-to-air ratios. Therefore, a lean blow-off test has to be performed under those conditions to map the stability of the combustor.
- Increase the heating capability of the oxidiser pre-heater. In the current situation, preheating is limited to 320°C. By increasing the preheating capabilities, a parametrisation can be performed based on a variation in inlet temperature. Higher reactant temperatures are thought to positively influence the attainment of flameless combustion.
- The influence of the jet momentum is not investigated separately, because it is a function of all different operating parameters studied in light of the present work. However, it is recommended to look into this parameter for similar operating conditions as explored in this work. The jet momentum can be varied using different nozzle diameters.
- For future research, it is recommended to gain insight into the flow-chemistry interaction characterised by the local Damköhler number. With the currently obtained high-resolution PIV data, information on the local flow time scale is already available. However, some effort still has to be put into retrieving local chemistry time scale information, either by simulations or experiments. This analysis could result in a more fundamental characterisation of flameless combustion.

- One of the issues with the current setup is the influence of exhaust cooling air being entrained into the combustor, as deduced from the unexpectedly high values for O_2 measured near the exit of the combustor. Varying the amount of cooling air injected could indicate the influence of air entrainment under certain operating conditions by continuously measuring the oxygen concentration at port 6. If the hypothesis is true, a decrease in cooling air will result in a reduction in O_2 levels. Therefore, it is recommended to redesign the connection between the combustor and the exhaust duct. A more gradual change in diameter near the exit, a converging duct, would largely limit the formation of recirculation zones in this region and hence limit the possibility of entraining cooling air.
- The developed gas sampling probe proved to cool the sample gas too much, as the temperature dropped below the dew point. It is thus recommended to redesign the gas sampling probe, reduce the sample gas's cooling, and keep the gas temperature at the probe exit above 60°C while simultaneously satisfying the probe outer surface cooling requirements.

It is important to note that the preceding conclusions are characteristic of this specific combustor setup under the operating conditions investigated. The derivation of general trends for the attainment of flameless or ultra-low NO_x combustion is difficult as this mainly depends on the combustor and burner head layout. Therefore, care should be taken when generalising the results and conclusions obtained from this research.



Background Oriented Schlieren

The Background Oriented Schlieren technique is based on conventional Schlieren flow imaging techniques. Large-scale flow phenomena can be visualised through optical flow distortions which are reproduced on a vector map, to visualise density gradients and temperature fields.

In the BOS setup, an image containing a random dot pattern is added in the background of the measured flow field. The camera is focussed on this image before and during the reacting flow experiment. Subsequently, the two pattern images are correlated, much the same as with PIV, to determine the 'displacement' of the dots. This is subsequently used to determine the displacement and light deflection angles in the flow with density variations. The BOS setup provides the opportunity to measure density and temperature fields. Moreover, it is a simpler method compared to laser imaging methods, without the need for the flow to be seeded. Unfortunately, this technique did not perform well on the used multi-nozzle combustor setup. Some of the results obtained by the BOS method are shown in a presentation in this appendix.

Experimental Set-up 1/2

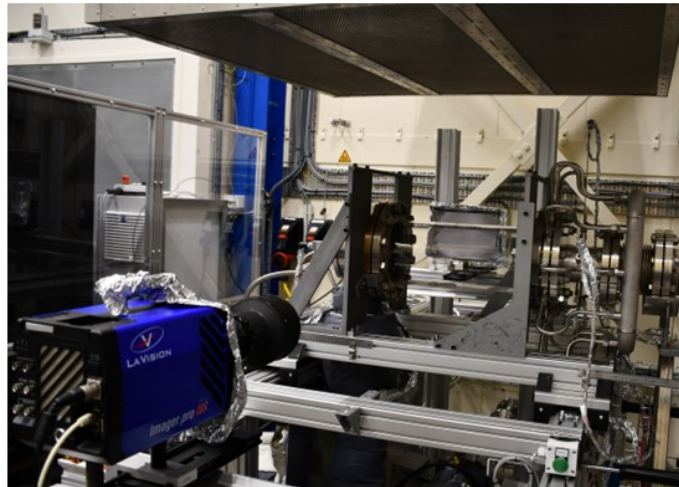
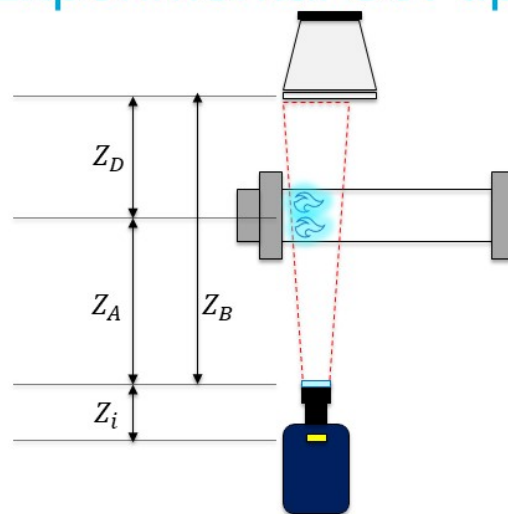


Figure A.1: Overview BOS setup 1/2

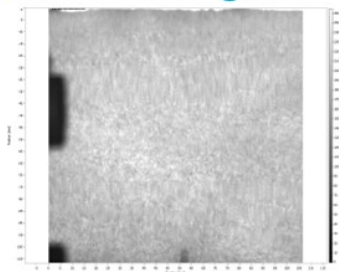
Experimental Set-up 2/2



f	200 mm
f_{stop}	11
M	0.14/0.21
$\frac{Z_A}{Z_B}$	0.68
Z_A	1097 mm
Z_B	1624 mm
Z_D	527 mm
Z_i	228 mm

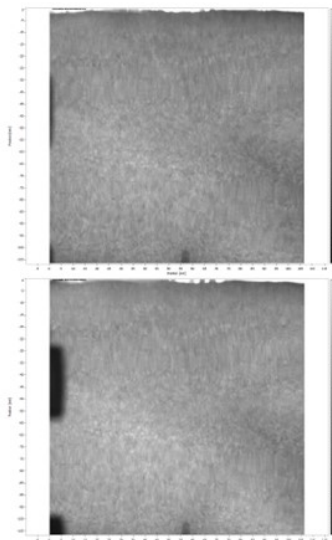
Figure A.2: Overview BOS setup 2/2

Raw Images



Reference images during experimental campaign.

Clockwise starting at the left top; Before the experiments, in-between the 1st & 2nd set of experiment, after finishing the experiments



7

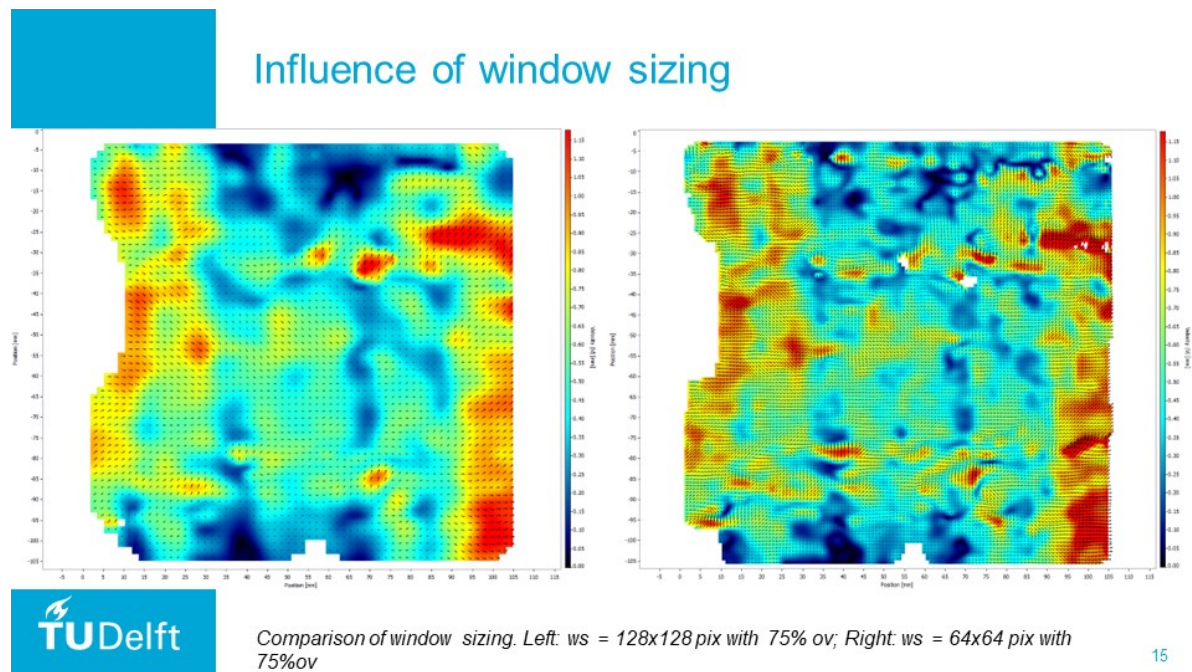
Figure A.3: Raw images of background pattern

Post-processing

- **First Image (Ref. Image)**
 - Average of ± 20 images
- **Intensity normalisation to first image**
 - Images are adapted to reach the same mean intensity as the first image
 - Account for non-uniform lighting (due to discontinuous light source)
- **Masking**
 - Geometric mask \rightarrow mask out surroundings (bolts e.g.)
- **Create multi-frame buffer from time-series**
 - Create (n-1) images
- **Cross-correlation**
 - Frame size: 2016x2016 pixels
 - 1st iteration 256x256 pixels (50% overlap)
 - 4th iteration 128x128 pixels (87.5% overlap)

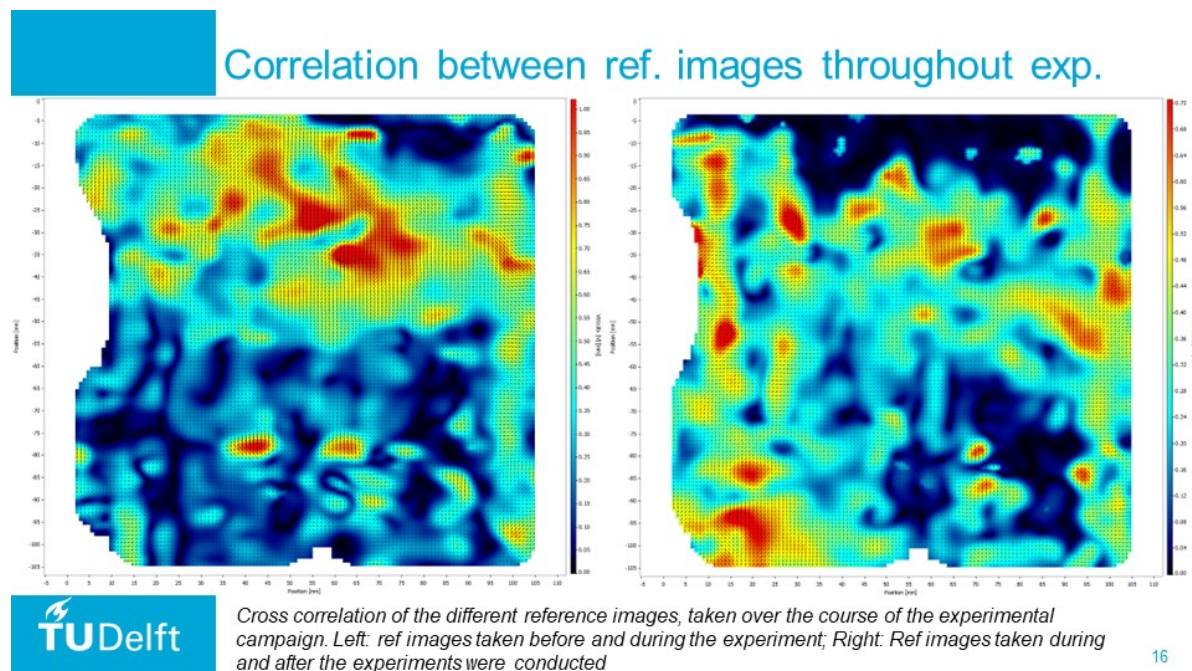
9

Figure A.4: BOS post-processing steps



15

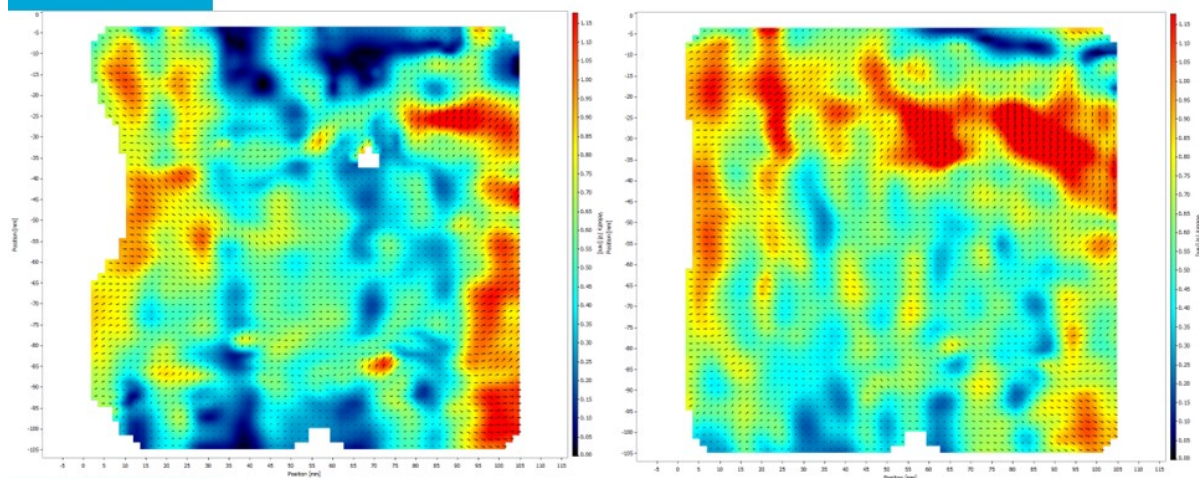
Figure A.5: Influence of window sizing on the cross correlation results



16

Figure A.6: Correlation between reference images obtained during experimental campaign

Correlation difference due to def. of ref. image

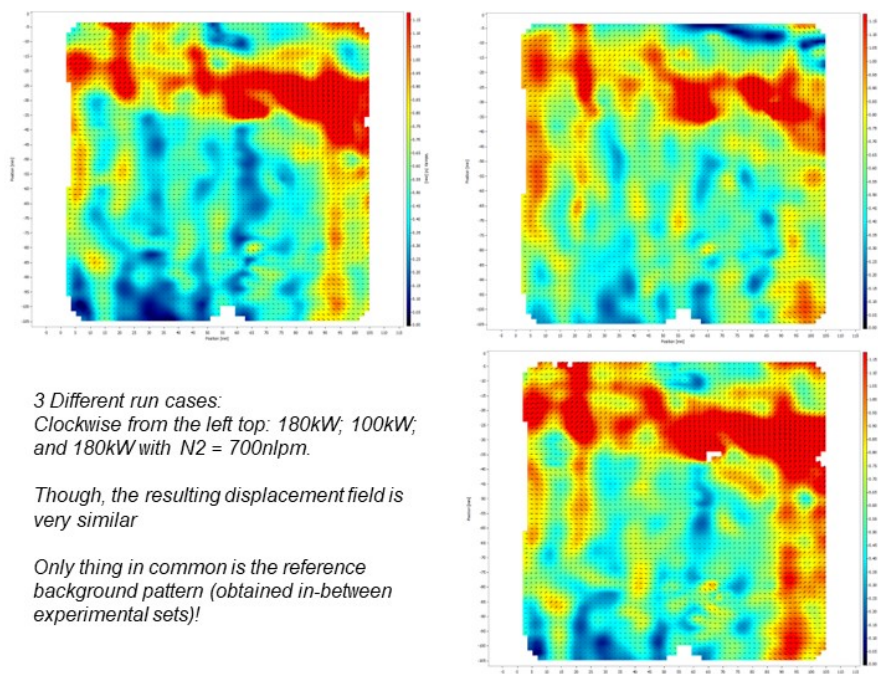


TU Delft

Difference in cross correlation due to difference in reference image for the same experimental image.
Left: cross correlation with reference image from the set obtained before starting the experiments;
Right: cross correlation with reference image from the set obtained in-between 2 sets of experiments

17

Figure A.7: Cross-correlation results due to deformation of the reference image 1/2



3 Different run cases:
Clockwise from the left top: 180kW; 100kW;
and 180kW with N2 = 700lpm.


Though, the resulting displacement field is
very similar

Only thing in common is the reference
background pattern (obtained in-between
experimental sets)!

TU Delft

18

Figure A.8: Cross-correlation results due to deformation of the reference image 2/2




Conclusions

- Main particle displacements are most likely due to deformation background pattern rather than density gradients
- The current set-up is most likely insensitive to small scale density gradients
- Nonetheless, temperature gradients are assumed to be less substantial. More uniformly distributed temperature field may be the cause?
- No other relevant conclusions can be drawn from these current results

19

Figure A.9: Conclusions BOS



Sources of uncertainty

- Deformation/burning of the background paper
- Deformation of the dots as seen by the camera due to the curvature and structure of glass tube
- (Forced) Convection around the tube, in the line of sight (camera-background), due to the airflow drawn upwards by the fume hood.
- Large particle image diameter, resulting in large window size. Information on small scale phenomena is lost.
- Projecting 3D phenomena onto a 2D plane
- Sensitivity of the set-up is too low to recognize changes in combustion regime

20

Figure A.10: Sources of uncertainty

B

Combustor system layout

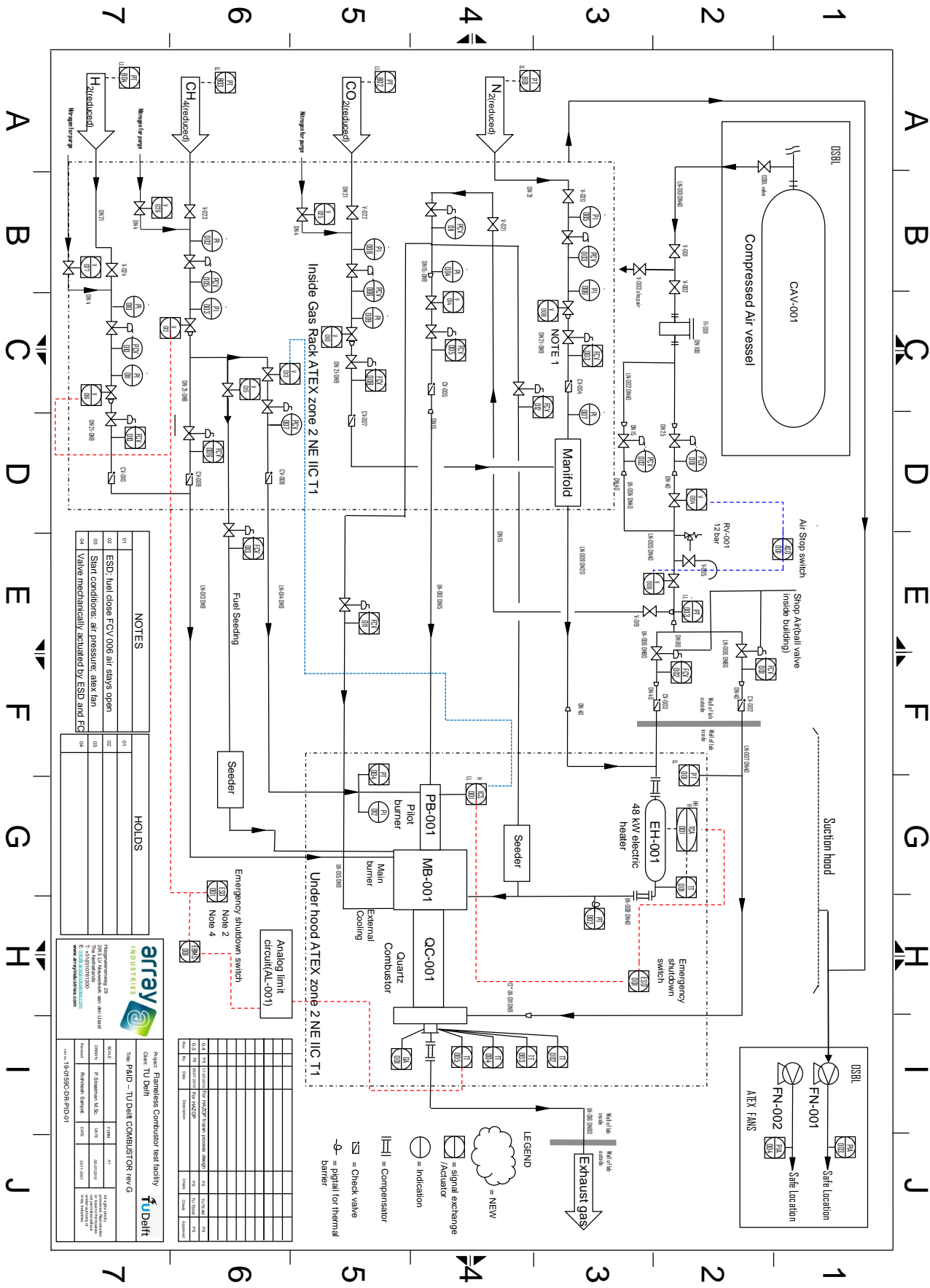


Figure B.1: Combustor system layout

C

Gas supply system layout

D

Gas probe strakes overview

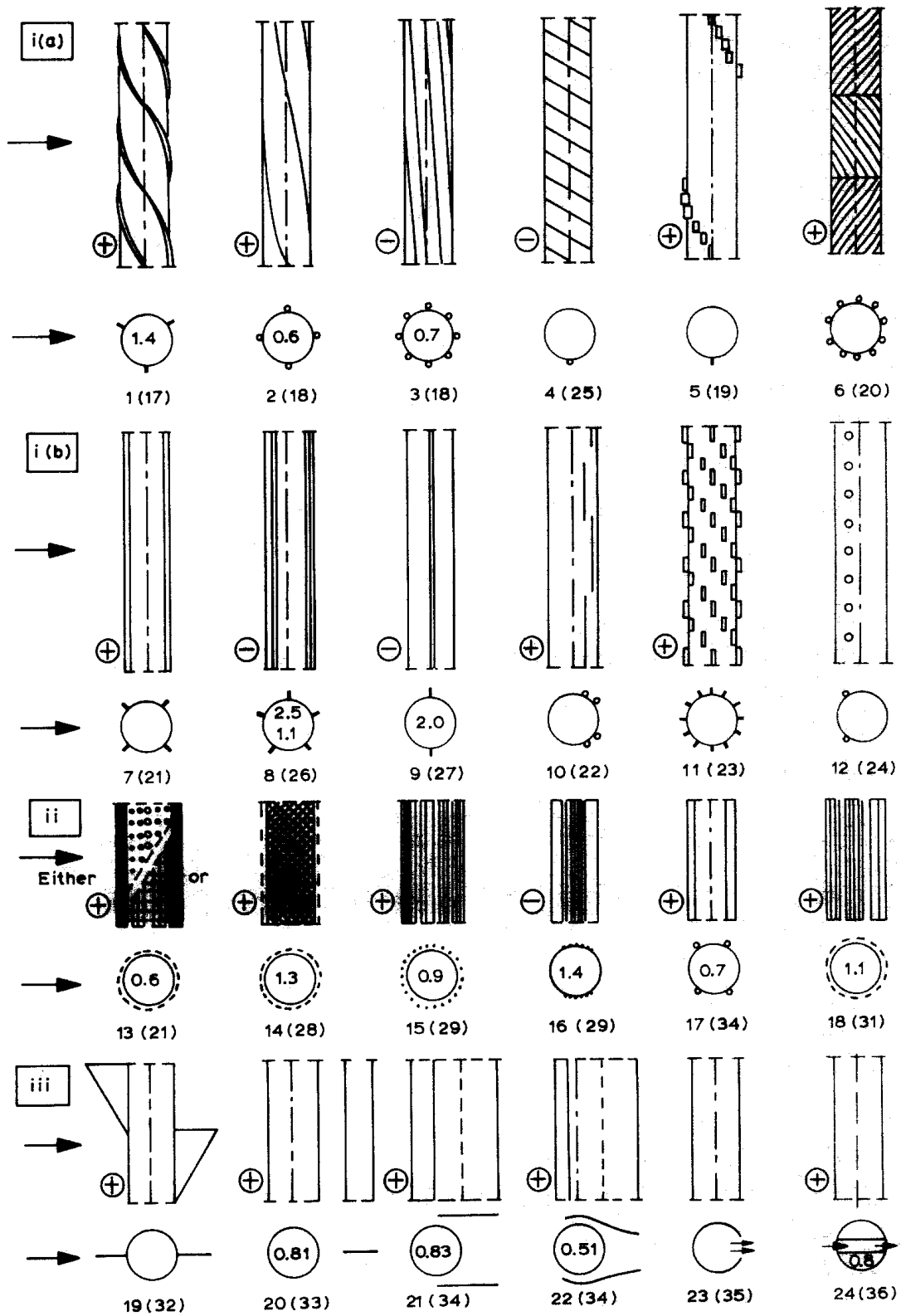


Figure D.1: Different concepts for the suppression of vortex shedding

E

Gas sampling probe layout

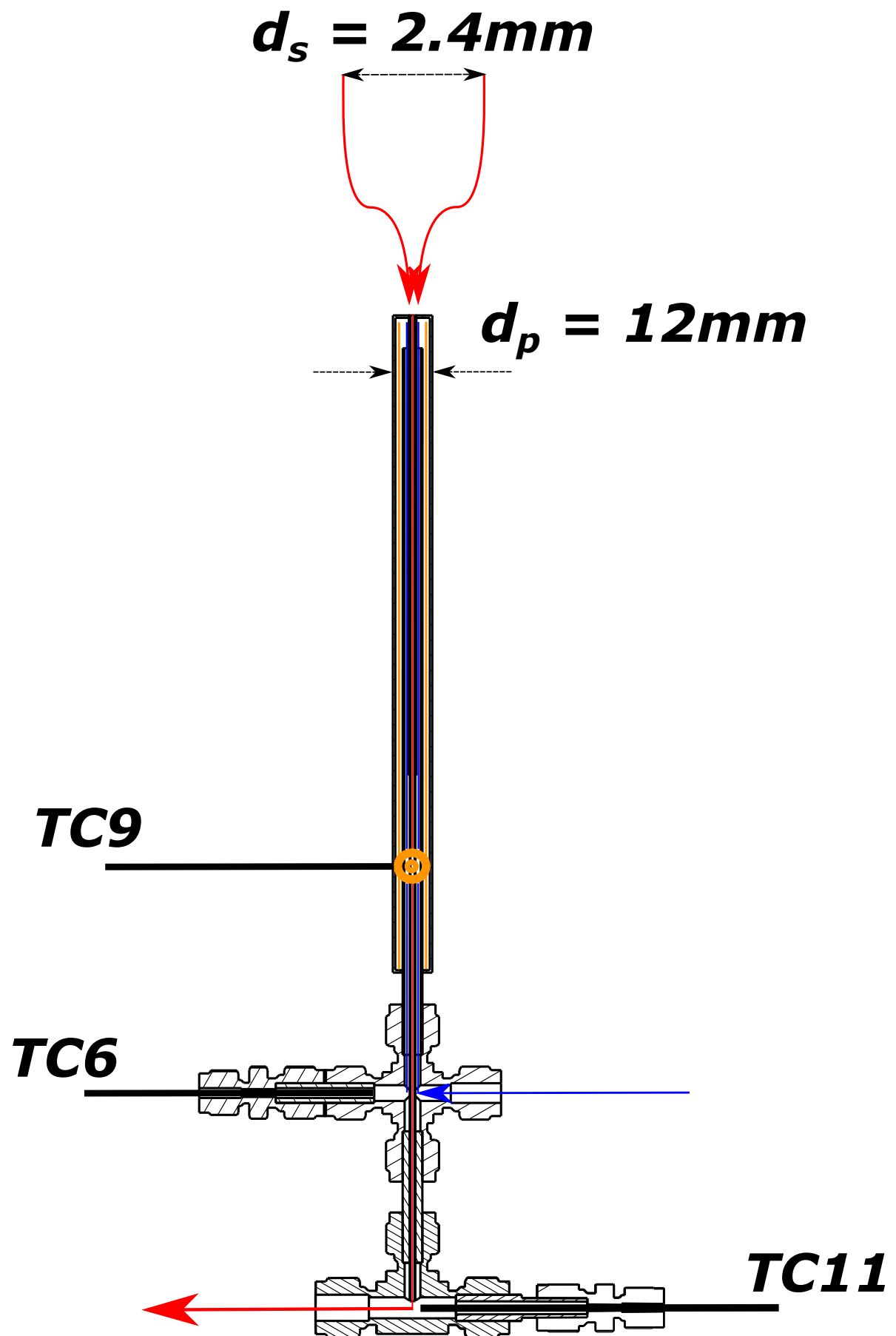


Figure E.1: Schematic of the cooled gas sampling probe

F

Uncertainty PIV plots

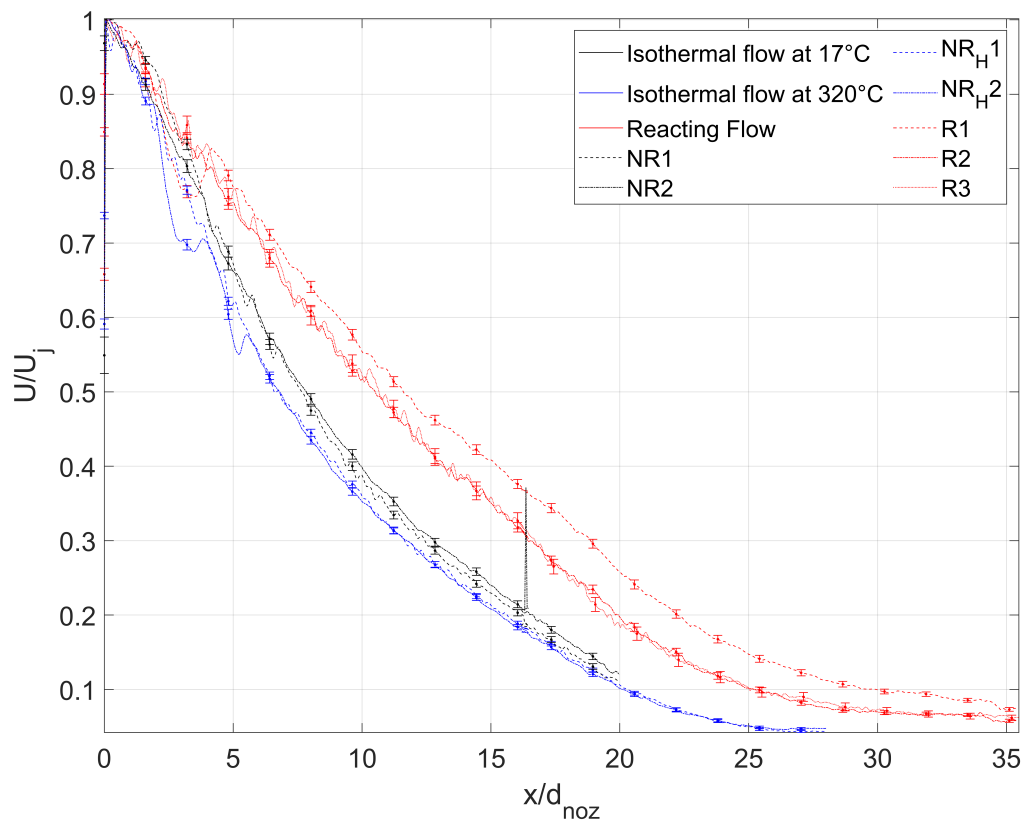


Figure F1: Axial velocity distribution along the jet centreline including error-bars representing measurement uncertainty

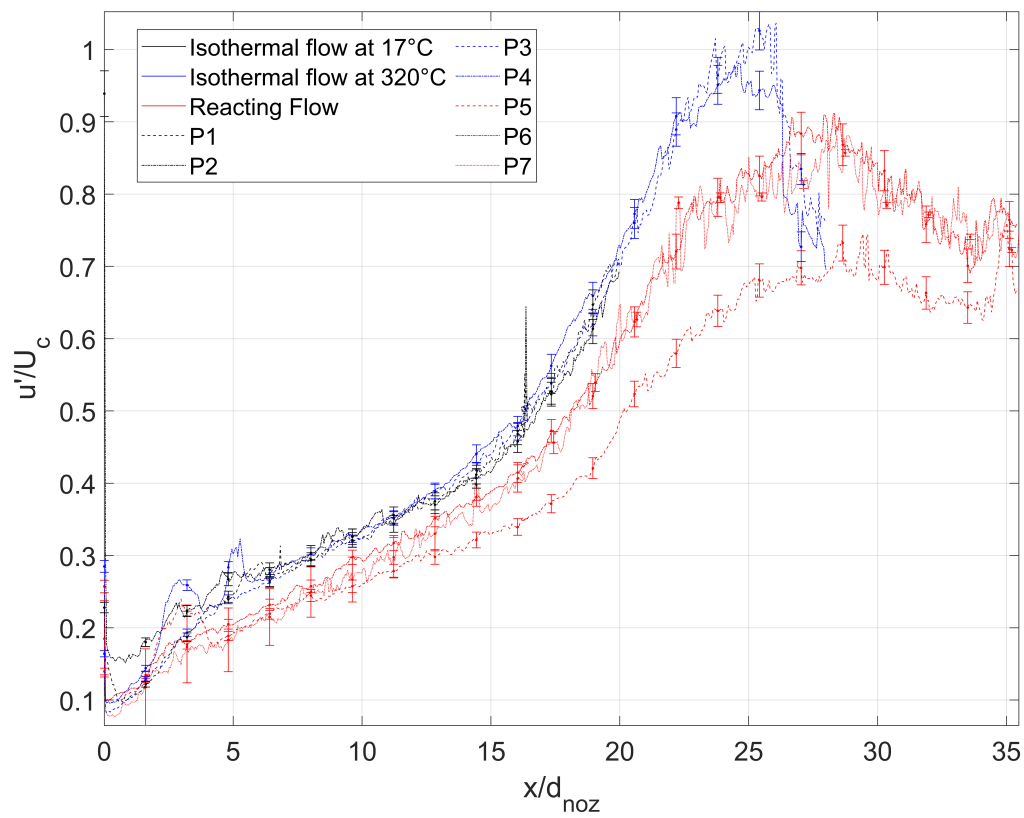


Figure E2: Turbulence intensity distribution along the jet centreline including error-bars representing measurement uncertainty

Bibliography

- [1] R. K. Pachauri and L. A. Meyer. *IPCC, 2014: Climate Change 2014: Synthesis Report. Contribution of Working Groups I, II and III to the Fifth Assessment Report of the Intergovernmental Panel on Climate Change*. Vol. 9781107025. Geneva, Switzerland, 2014, p. 151. ISBN: 9781139177245. DOI: [10 . 1017 / CB09781139177245.003](https://doi.org/10.1017/CB09781139177245.003).
- [2] Nations Unies. “Accord de Paris”. In: *21ème Conférence des Parties* (2015), pp. 1–18. URL: https://unfccc.int/sites/default/files/french_paris_agreement.pdf.
- [3] European Environment Agency. *Greenhouse gas emissions from transport in Europe*. 2017. URL: <https://www.eea.europa.eu/data-and-maps/indicators/transport-emissions-of-greenhouse-gases/transport-emissions-of-greenhouse-gases-12> (visited on 09/15/2020).
- [4] D. S. Lee et al. “Aviation and global climate change in the 21st century”. In: *Atmospheric Environment* 43.22-23 (2009), pp. 3520–3537. ISSN: 1352-2310. DOI: [10 . 1016 / j . atmosenv . 2009 . 04 . 024](https://doi.org/10.1016/j.atmosenv.2009.04.024). URL: <http://dx.doi.org/10.1016/j.atmosenv.2009.04.024>.
- [5] S. M. Correa. “A review of NO_x formation under gas-turbine combustion conditions”. In: *Combustion Science and Technology* 87.1-6 (1993), pp. 329–362. ISSN: 1563521X. DOI: [10 . 1080 / 00102209208947221](https://doi.org/10.1080/00102209208947221).
- [6] Advisory Council for Aeronautics Research in Europe. *Flightpath 2050 Europe ’ s Vision for Aviation*. Tech. rep. European Commission, 2011. DOI: [10 . 2777 / 50266](https://doi.org/10.2777/50266).
- [7] A. A. V. Perpignan. “Emission Modelling from a Multi-Fuel Dual Combustor Gas Turbine”. PhD thesis. 2020, p. 289. ISBN: 9789055841745. DOI: [10 . 4233 / uuid](https://doi.org/10.4233/uuid).
- [8] D. C. Vaz. “Towards the Application of Flameless Combustion to Micro Gas Turbines”. PhD thesis. Universidade Nova de Lisboa, 2007, p. 298.
- [9] O. Lammel et al. “FLOX® Combustion at high power density and high flame temperatures”. In: *Journal of Engineering for Gas Turbines and Power* 132.12 (2010), pp. 1–10. ISSN: 07424795. DOI: [10 . 1115 / 1 . 4001825](https://doi.org/10.1115/1.4001825).
- [10] R. Lückcrath, W. Meier, and M. Aigner. “FLOX® combustion at high pressure with different fuel compositions”. In: *Journal of Engineering for Gas Turbines and Power* 130.1 (2008), pp. 1–7. ISSN: 07424795. DOI: [10 . 1115 / 1 . 2749280](https://doi.org/10.1115/1.2749280).
- [11] R. Sadanandan et al. “Flame characteristics and emissions in flameless combustion under gas turbine relevant conditions”. In: *Journal of Propulsion and Power* 27.5 (2011), pp. 970–980. ISSN: 15333876. DOI: [10 . 2514 / 1 . 50302](https://doi.org/10.2514/1.50302).
- [12] H. Schütz et al. “Analysis of the pollutant formation in the FLOX® combustion”. In: *Journal of Engineering for Gas Turbines and Power* 130.1 (2008), pp. 1–9. ISSN: 07424795. DOI: [10 . 1115 / 1 . 2747266](https://doi.org/10.1115/1.2747266).
- [13] M. Severin et al. “Flame stabilization regimes of lean premixed confined jet flames at different reynolds numbers”. In: *53rd AIAA/SAE/ASEE Joint Propulsion Conference, 2017 July* (2017). DOI: [10 . 2514 / 6 . 2017 - 4684](https://doi.org/10.2514/6.2017-4684).
- [14] R. Sampat et al. “OPERATING CHARACTERISTICS OF A FLAMELESS COMBUSTOR OBTAINED BY EXPERIMENTS INFORMED MODELLING”. In: *Turbomachinery Technical Conference and Exposition GT2022*. 2022.
- [15] T. Á. Rutar et al. “NO_x formation pathways in lean-premixed-prevapourized combustion of fuels”. In: *221.x* (2007), pp. 387–398. DOI: [10 . 1243 / 09576509JPE288](https://doi.org/10.1243/09576509JPE288).
- [16] M. Flamme. “New combustion systems for gas turbines (NGT)”. In: *Applied Thermal Engineering* 24.11-12 (2004), pp. 1551–1559. ISSN: 13594311. DOI: [10 . 1016 / j . applthermaleng . 2003 . 10 . 024](https://doi.org/10.1016/j.applthermaleng.2003.10.024).
- [17] C. Bruno and M. Losurdo. “The Trapped Vortex Combustor: An Advanced Combustion Technology for Aerospace and Gas Turbine Applications”. In: *Advanced Combustion and Aerothermal Technologies* (2007), pp. 365–384. DOI: [10 . 1007 / 978 - 1 - 4020 - 6515 - 6 _ 28](https://doi.org/10.1007/978-1-4020-6515-6_28).

- [18] J. A. Wüning and J. G. Wüning. "Flameless oxidation to reduce thermal no-formation". In: *Progress in Energy and Combustion Science* 23.1 (1997), pp. 81–94. ISSN: 03601285. DOI: [10.1016/s0360-1285\(97\)00006-3](https://doi.org/10.1016/s0360-1285(97)00006-3).
- [19] A. Cavaliere and M. De Joannon. *Mild combustion*. Vol. 30. 4. 2004, pp. 329–366. ISBN: 3981593693. DOI: [10.1016/j.pecs.2004.02.003](https://doi.org/10.1016/j.pecs.2004.02.003).
- [20] C. K. Law. *Combustion Physics*. Cambridge University Press, 2006, p. 400. ISBN: 9780521870528. DOI: <https://doi.org/10.1017/CB09780521870528>.
- [21] M. Oberlack, R. Arlitt, and N. Peters. "2ss On stochastic Damk " ohler number variations in a". In: 4 (2000), pp. 495–509.
- [22] M. J. Evans et al. "Classification and lift-off height prediction of non-premixed MILD and autoignitive flames". In: *Proceedings of the Combustion Institute* 36.3 (2017), pp. 4297–4304. ISSN: 15407489. DOI: [10.1016/j.proci.2016.06.013](https://doi.org/10.1016/j.proci.2016.06.013).
- [23] A. A. V. Perpignan, A. Gangoli Rao, and D. J.E.M. Roekaerts. "Flameless combustion and its potential towards gas turbines". In: *Progress in Energy and Combustion Science* 69 (2018), pp. 28–62. ISSN: 03601285. DOI: [10.1016/j.pecs.2018.06.002](https://doi.org/10.1016/j.pecs.2018.06.002).
- [24] A. Gangoli Rao and Y. Levy. "A New Combustion Methodology for Low Emission Gas Turbine Engines". In: *8th International Symposium on High Temperature Air Combustion and Gasification* July (2010), pp. 177–185.
- [25] C. Galletti, A. Parente, and L. Tognotti. "Numerical and experimental investigation of a mild combustion burner". In: *Combustion and Flame* 151.4 (2007), pp. 649–664. ISSN: 00102180. DOI: [10.1016/j.combustflame.2007.07.016](https://doi.org/10.1016/j.combustflame.2007.07.016).
- [26] R. Borghi. "on the Structure and Morphology of Turbulent Premixed Flames." In: *Recent Adv in the Aerosp Sci* 230 (1985), pp. 117–138. DOI: [10.1007/978-1-4684-4298-4_7](https://doi.org/10.1007/978-1-4684-4298-4_7).
- [27] Norbert Peters. *Turbulent Combustion*. Cambridge University Press, 2004. ISBN: 978-0-89871-053-3. DOI: [10.1137/1.9781611971064.ch3](https://doi.org/10.1137/1.9781611971064.ch3).
- [28] O. Lammel et al. "FLOX® Combustion at high power density and high flame temperatures". In: *Journal of Engineering for Gas Turbines and Power* 132.12 (2010), pp. 1–10. ISSN: 07424795. DOI: [10.1115/1.4001825](https://doi.org/10.1115/1.4001825).
- [29] Y. Levy, V. Sherbaum, and P. Arfi. "Basic thermodynamics of FLOXCOM , the low-NO x gas turbines adiabatic combustor". In: 24.x (2004), pp. 1593–1605. DOI: [10.1016/j.applthermaleng.2003.11.022](https://doi.org/10.1016/j.applthermaleng.2003.11.022).
- [30] M. J. Melo, J. M. M. Sousa, and M. Costa. "Experimental Investigation of a Novel Combustor Model for Gas Turbines". In: 25.3 (2009). DOI: [10.2514/1.35173](https://doi.org/10.2514/1.35173).
- [31] M. J. Melo, J. M. M. Sousa, and M. Costa. "Flow and Combustion Characteristics of a Low-NOx Combustor Model for Gas Turbines". In: 27.6 (2011). DOI: [10.2514/1.B34033](https://doi.org/10.2514/1.B34033).
- [32] Y. Levy et al. "DESIGN AND PERFORMANCE ANALYSIS OF A GAS TURBINE FLAMELESS COMBUSTOR USING CFD SIMULATIONS". In: (2012).
- [33] A. Giese, M. Flamme, and M. Brune. "F L A M E L E S S O X I D AT I O N A N D C O N T I N U E D STAGED AIR COMBUSTION SYSTEMS FOR GAS TURBINES". In: 5 (2004), pp. 391–405.
- [34] M. Huijts. "An experimental and numerical investigation of the aerodynamic characteristics of a flameless combustor". PhD thesis. Delft University of Technology, 2018, p. 118.
- [35] *Gri-mech3.0*. URL: <http://combustion.berkeley.edu/gri-mech/overview.html> (visited on 11/03/2021).
- [36] A. H. Lefebvre and D. R. Ballal. *Gas turbine combustion*. 1983, p. 390.
- [37] C. Tropea, A. L. Yarin, and J. F. Foss. *Springer Handbook of Experimental Fluid Mechanics*. Springer-Verlag Berlin Heidelberg, 2007, p. 1557. ISBN: 9783540251415.
- [38] F. Chen and H. Liu. "Particle image velocimetry for combustion measurements : Applications and developments". In: *Chinese Journal of Aeronautics* 31.7 (2018), pp. 1407–1427. ISSN: 1000-9361. DOI: [10.1016/j.cja.2018.05.010](https://doi.org/10.1016/j.cja.2018.05.010). URL: <https://doi.org/10.1016/j.cja.2018.05.010>.

- [39] F. Scarano and B. W. Van Oudheusden. "Planar velocity measurements of a two-dimensional compressible wake". In: 34 (2003), pp. 430–441. DOI: [10.1007/s00348-002-0581-x](https://doi.org/10.1007/s00348-002-0581-x).
- [40] A. Melling. "Tracer particles and seeding for particle image velocimetry". In: *Measurement Science and Technology* 8 (1997), pp. 1406–1416.
- [41] F. Scarano. *Experimental aerodynamics*. February. 2013, pp. 1–454. ISBN: 9781498704021. DOI: [10.1201/9781315371733](https://doi.org/10.1201/9781315371733).
- [42] F. T. M. Nieuwstadt, B. J. Boersma, and J. Westerweel. *Frans T.M. Nieuwstadt Bendiks J. Boersma Jerry Westerweel*. ISBN: 9783319315973.
- [43] C. Willert and M. Jarius. "Planar flow field measurements in atmospheric and pressurized combustion chambers". In: 33 (2002), pp. 931–939. DOI: [10.1007/s00348-002-0515-7](https://doi.org/10.1007/s00348-002-0515-7).
- [44] A. Sciacchitano. "Uncertainty quantification in particle image velocimetry". In: (2019).
- [45] J. Charonko and P. Vlachos. "Estimation of uncertainty bounds for individual particle image velocimetry measurements from cross-correlation peak ratio". In: *Measurement Science and Technology* 24 (2013), p. 16. DOI: [10.1088/0957-0233/24/6/065301](https://doi.org/10.1088/0957-0233/24/6/065301).
- [46] Z. Xue, J. Charonko, and P. Vlachos. "Signal-to-noise ratio, error and uncertainty of PIV measurement". In: *PIV13; 10th International Symposium on Particle Image Velocimetry*. Delft: Delft University of Technology, 2013.
- [47] D. Ragni et al. "Particle tracer response across shocks measured by PIV". In: (2011), pp. 53–64. DOI: [10.1007/s00348-010-0892-2](https://doi.org/10.1007/s00348-010-0892-2).
- [48] Z. Sun. "Micro Ramps in Supersonic Turbulent Boundary Layers". PhD thesis. Technische Universiteit Delft, 2014, p. 182. ISBN: 9789461919243.
- [49] L. H. Benedict and R. D. Gould. "Towards better uncertainty estimates for turbulence statistics". In: 22 (1996).
- [50] M. Xu et al. "PIV measurements of turbulent jets issuing from triangular and circular orifice plates". In: 56.6 (2013), pp. 1176–1186. DOI: [10.1007/s11433-013-5099-0](https://doi.org/10.1007/s11433-013-5099-0).
- [51] C. G. Ball, H. Fellouah, and A. Pollard. "The flow field in turbulent round free jets". In: *Progress in Aerospace Sciences* 50 (2012), pp. 1–26. ISSN: 03760421. DOI: [10.1016/j.paerosci.2011.10.002](https://doi.org/10.1016/j.paerosci.2011.10.002).
- [52] P. Kalt et al. "PIV measurements of a turbulent jet issuing from round sharp-edged plate". In: (2007), pp. 625–637. DOI: [10.1007/s00348-007-0271-9](https://doi.org/10.1007/s00348-007-0271-9).
- [53] M. V. Heitor and A. L.N. Moreira. "Thermocouples and sample probes for combustion studies". In: *Progress in Energy and Combustion Science* 19.3 (1993), pp. 259–278. ISSN: 03601285. DOI: [10.1016/0360-1285\(93\)90017-9](https://doi.org/10.1016/0360-1285(93)90017-9).
- [54] S. W. Churchill and M. Bernstein. "A Correlating Equation for Forced Convection From Gases and Liquids to a Circular Cylinder in Crossflow". In: *Journal of Heat Transfer* 99 (1977), pp. 300–306. DOI: <https://doi.org/10.1115/1.3450685>.
- [55] D. Popa and F. Udrea. "Towards integrated mid-infrared gas sensors". In: *Sensors (Switzerland)* 19.9 (2019), pp. 1–15. ISSN: 14248220. DOI: [10.3390/s19092076](https://doi.org/10.3390/s19092076).
- [56] S. Gluck et al. "Evaluation of NO x Flue Gas Analyzers for Accuracy and Their Applicability for Low-Concentration Measurements Evaluation of NO x Flue Gas Analyzers for Accuracy and Their Applicability for Low-Concentration Measurements". In: 2247.x (2012). DOI: [10.1080/10473289.2003.10466208](https://doi.org/10.1080/10473289.2003.10466208).
- [57] *Paramagnetic cells*. URL: <https://industrialphysics.com/knowledgebase/paramagnetic-cells-technology-for-our-paramagnetic-o2-analyser/> (visited on 02/17/2022).
- [58] J. P. Holman. *Heat transfer: Tenth Edition*. 10th. McGraw-Hill Education, 2010, p. 758. ISBN: 978-0-07-352936-3.
- [59] V. Gnielinski. "New equations for heat and mass transfer in turbulent pipe and channel flow". In: *International Journal of Chemical Engineering* 16 (1976), pp. 359–368.
- [60] VDI-Gesellschaft Verfahrenstechnik und Chemieingenieurwesen, ed. *VDI Heat Atlas: Second Edition*. 2nd. Springer-Verlag Berlin Heidelberg, 2010. DOI: [10.1007/978-3-540-77877-6](https://doi.org/10.1007/978-3-540-77877-6).

- [61] J. H. Lienhard. *Synopsis of lift, drag, and vortex frequency data for rigid circular cylinders*. Tech. rep. Washington: Washington State University, 1966, p. 36.
- [62] W. C. Young and R. G. Budynas. *Roark 's Formulas for Stress and Strain*. 7th. McGraw-Hill, 2002, p. 854. ISBN: 007072542X.
- [63] M. M. Zdravkovich. "Review and classification of various aerodynamic and hydrodynamic means for suppressing vortex shedding". In: *JOurnal of Wind Engineering and Industrial Aerodynamics* 7 (1981), pp. 145–189.
- [64] ABB. *AO2000 Series Operator's Manual*. 2009.
- [65] Gaslab.com. *Gas sensor calibration*. URL: <https://gaslab.com/blogs/articles/gas-sensor-calibration> (visited on 04/26/2022).
- [66] C. E. Baukal and P. B. Eleazer. "Quantifying NO_x for industrial combustion processes". In: *Journal of the Air and Waste Management Association* 48.1 (1998), pp. 52–58. ISSN: 10473289. DOI: [10 . 1080 / 10473289.1998.10463664](https://doi.org/10.1080/10473289.1998.10463664).
- [67] ASME. *Part 10: Flue and Exhaust Gas Analyses*. New York: American Society of Mechanical Engineers, 1981.
- [68] C. Antoine. "Tensions des vapeurs: nouvelle relation entre les tensions et les temperatures". In: *Compt. Rend. Acad. Sci.* 107 (1888).
- [69] G. Leonard and J. Stegmaier. "Development of an aeroderivative gas turbine dry low emissions combustion system". In: *ASME 1993 International Gas Turbine and Aeroengine Congress and Exposition, GT 1993 3B*. July 1994 (1993). DOI: [10.1115/93-GT-288](https://doi.org/10.1115/93-GT-288).
- [70] A. S. Veríssimo, A. M .A. Rocha, and M. Costa. "Operational , Combustion , and Emission Characteristics of a Small-Scale Combustor". In: *Energy and Fuels* x (2011), pp. 2469–2480.